Physicochemical properties and photodynamic therapy activities of indium and zinc phthalocyanine-nanoparticle conjugates

A thesis submitted in fulfilment of the requirements for the degree of

DOCTOR OF PHILOSOPHY

Of

RHODES UNIVERSITY

By

EDITH DUBE

November 2018

Dedication

This work is dedicated to my loving husband Thabani Dube and my children Nkosana Thabani, Nkazimulo Zalobuhle and Thando Ndumiso.

Acknowledgments

I would like to express my sincere gratitude to Distinguished Professor Tebello Nyokong for offering me the opportunity to pursue my PhD degree under her wing. Her inexorable guidance, support and encouragement throughout the programme allowed me to grow as a research scientist.

Special thanks goes to Dr. David Oluwole and Njemuwa Nwaji for their amazing ideas, insights and continuous support in my research.

I would like to thank Dr John Mack, Dr Jonathan Britton, Ms Gail Cobus and Mr Francis Chindeka for their support and for making the Center for Nanotechnology Innovation a pleasurable environment to work in. I am also grateful for the support from Dr Earl Prinsloo, Shirley, Marvin and members of staff in the Chemistry Department. To the S22 family, thank you for the enjoyable moments during the three years.

A special thanks to my family and friends. Words cannot express how grateful I am to my sister Primrose, my mum and Dad, my father in law Mr T. T. Dube my siblings and friends for the sacrifices they made on my behalf. Their prayers and support sustained me thus far.

My special appreciation goes to my beloved husband Thabani for the sacrifices, support, patience and understanding throughout this period. And to my three boys for making my study period pleasurable, I thank you.

I am so grateful for the financial support from the National Research Fund (NRF).

Lastly l give praise to God who made it possible.

ABSTRACT

The syntheses and characterization of symmetric and asymmetric Pcs functionalized at the peripheral position are reported. The Pcs contain either zinc or indium as central metals and have carboxyphenoxy, phenoxy propanoic acid, benzothiazole phenoxy, thiophine ethoxy or di-*O*-isopropylidene-α-D-glucopyranose as ring substituents. The Pcs were linked to NPs via an amide bond or through self-assembly.

The photophysics and photochemistry of the Pcs were assessed when alone and with conjugates. All the studied Pcs showed good photophysicochemical behaviour with relatively high triplet and singlet oxygen quantum yields corresponding to their low fluorescence quantum yield. The Pcs with indium in their central cavity exhibited higher triplet and singlet oxygen quantum yields in comparison to their zinc counterparts due to the heavy–atom effect obtained from the former. Asymmetrical Pcs displayed higher triplet and singlet oxygen quantum yields than their symmetrical counterparts.

The triplet quantum yield, generally increased on linkage to nanoparticles (NPs) due to the heavy–atom effect of gold and silver in NPs. The conjugates to gold nanospheres yielded higher triplet and singlet quantum yields than their gold nanotriangles counterparts due to the higher loading by the former probably encouraged by their relatively small particle size.

The *in vitro* dark cytotoxicity and photodynamic therapy of selected Pc complexes and conjugates against MCF-7 cells was tested. All studied Pc complexes and conjugates showed minimum dark toxicity making them

applicable for PDT. All complexes displayed poor phototoxicity with > 50% cell viability at concentrations ≤ 160 μg/mL, however the conjugates showed < 50% cell viability at concentrations ≤ 160 μg/mL probably due to the enhanced singlet oxygen quantum yield.

The findings from this work show the importance of linking photosensitises such as phthalocyanines to metal nanoparticles for the enhancement of singlet oxygen quantum yield and ultimately the photodynamic effect.

TABLE OF CONTENTS

CONTENTS **PAGE**

LIST OF ABBREVIATIONS

^{1}H NMR	Proton nuclear magnetic resonance
ADMA	Tetrasodium α,α -(anthracene-9,10- diyl) dimethylmalonate
APTES	3–Aminopropyltriethoxysilane
AuCT	Gold chitosan
$CDCl_3$	Deuterated chloroform
CT	chitosan
CTAB	Cetyltrimethylammonium bromide
CTAC	Cetyltrimethylammonium chloride
DBU	1,8-diazabicyclo[5.4.0]undec-7-ene
DCC	Dicyclohexylcarbodiimide
DLS	Dynamic light scattering
DMAP	Dimethylaminopyridine
DMEM	Dulbecco's modified Eagle's medium
DMF	Dimethylformamide
DMSO	Dimethylsulfoxide
DMSO-d_6	Deuterated dimethylsulfoxide
DPBF	Diphenylisobenzofuran
DPBS	Dulbecco's modified phosphate buffer saline
DPE	Diphenyl ether
EPR	enhanced permeability and retention effect
FT–IR	Fourier Transform Infrared
GSH	Glutathione
GSS	Gold speckled silica nanoparticles
HAE	Heavy atom effect
HOMO	Highest occupied molecular orbital
IRF	Instrument response function
ISC	intersystem crossing
LUMO	Lowest unoccupied molecular orbital

MALDI	Matrix–Assisted Laser Desorption/Ionization
MCF 7	Michigan Cancer Foundation 7
MPc	Metallophthalocyanine
MS	Mass Spectrometer
Nd–YAG	Neodymium–doped Yttrium Aluminum Garnet
NPs	Nanoparticles
NRs	Nanorods
NSs	Nanospheres
NTs	Nanotriangles
OA	Oleic Acid
OLA	Oleylamine
PACT	Photodynamic antimicrobial chemotherapy
Pc	Phthalocyanine
PDT	Photodynamic therapy
PS	Photosensitiser
PTT	Photothermal therapy
ROS	reactive oxygen species
SEM	Scanning electron microscope
SOC	spin orbit coupling
SPR	surface plasmon resonance
Std	Standard
TCSPC	Time-correlated single photon counting
TEM	Transmission electron microscope
TEOS	Tetraethyl orthosilicate
THF	Tetrahydrofuran
UV–Vis	Ultraviolet–Visible
XPS	X–ray Photoelectron Spectroscopy
XRD	X–ray Diffractometer

LIST OF SYMBOLS

α	non-peripheral position
β	peripheral position
ε	molar extinction coefficient
λ	wavelength
τ_0	fluorescence radiative lifetime
τ_F	fluorescence lifetime
τ_T	triplet state lifetime
Φ_F	fluorescence quantum yield
Φ_T	triplet state quantum yield
Φ_Δ	singlet oxygen quantum yield
A/abs	absorbance/absorption
S_0	singlet ground state
S_1	singlet excited state
t	time
T_1	triplet excited state
$h\upsilon$	light (h =Planck's constant; υ = frequency of a photon of light)

CHAPTER 1

1. Introduction

Preamble

The thesis describes the synthesis of symmetrical and asymmetrical phthalocyanines (Pcs) containing zinc and indium as central metals. The Pcs are linked to Au containing nanoparticles via an amide or Au-S or Au-N bonds. The photophysical and photochemical properties of the Pcs and their conjugates are studied together with the photodynamic therapy behaviour against epithelial breast cancer cell lines (MCF 7).

1.1. Phthalocyanines

Phthalocyanines (Pcs) are planar aromatic macrocycles consisting of an 18 π–electron conjugated ring with four isoindole units connected via nitrogen atoms [1,2]. The Pc macrocycle can be substituted with different functional groups on the non–peripheral (α) and peripheral (β) positions (indicated in **Scheme 1.1,** to be discussed later) to influence their physicochemical properties which are crucial for their applications. At the same time the central cavity of Pcs can coordinate different metals to form metallophthalocyanines (MPcs) and these metals are known to influence their photophysical behaviour.

Pc derivatives have attracted attention as second generation photosensitisers (PS) for diverse applications such photodynamic therapy (PDT) [3–5], photodynamic antimicrobial chemotherapy (PACT) [6–8], photodegradation of pollutants [9] and nonlinear optics [10] to mention but a few. Their applicability could be attributed to their ease of structural modification, absorption in the near infra–red region, and good optical, chemical and thermal properties [11–15].

1.1.1. Electronic absorption Spectra

The ground state electronic absorption spectra of MPcs are often influenced by factors such as nature of the central metal, ring substituents, the solvent used, point of substitution and ring expansion [16–19]. MPcs are characterised by two distinct absorption bands as shown in **Figure 1.1.**

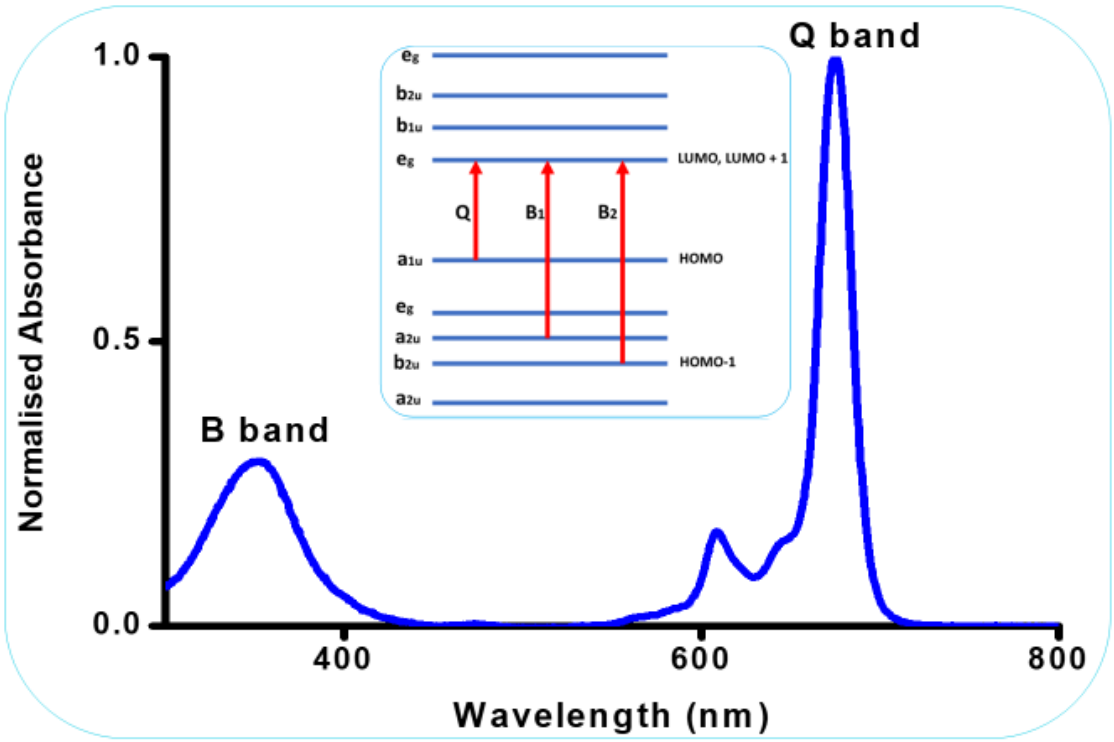

Figure 1.1: Ground state electronic absorption spectrum (insert: molecular orbital representation of electronic transition) for MPcs.

The Q-band is the most intense peak found in the visible and near infra-red region depending on the structural properties of the MPcs, while the B-band, found between 300–400 nm consist of two less intense, overlapping peaks due to B_1 and B_2 hence it is broad [20].

Using Gouterman's four orbital model [21], the Q-band is assigned to the doubly degenerate π-π* transition between the ground state a_{1u} of the highest occupied molecular orbital (HOMO) to the degenerate e_g of the lowest unoccupied molecular orbital (LUMO), while the B-bands (B_1 and B_2) correspond to the π-π* transitions from a_{2u} and b_{2u} of the HOMO to the e_g of the LUMO, **Figure 1.1** (insert) [20–23].

1.1.2. Synthesis of symmetrical and asymmetrical Pcs.

The synthesis of phthalocyanines can be achieved using different precursors such as: phthalamide, phthalic acid, phthalic anhydride, *o*-cyanobenzamide, *o*-dibromobenzene, diiminosoindoile and phthalonitrile. However, the method employing phthalonitrile precursors is much more popular due to ease of purification and high yields of Pcs [24].

For the synthesis of α and β-substituted Pcs, 3-nitrophthalonitrile and 4-nitrophthalonitrile, respectively, are used as precursors. The nitro groups of these phthalonitriles are modified to afford the desired substituted phthalonitriles for the synthesis of Pcs. Symmetrically tetra–substituted Pcs are synthesized by cyclo–condensation of mono–substituted phthalonitriles as precursors [25–27], **Scheme 1.1**.

Mono–substituted phthalonitriles always result in a mixture of four possible isomers of tetrasubstituted phthalocyanines with D_{2h}, C_{4h}, C_{2V}, and C_s symmetry as shown in **Figure 1.2** (using β substituted Pcs as examples). Similar isomers are obtained for the α substituted Pcs. Attempts have been made to isolate these isomers and a few have been isolated using column chromatography [28,29], however in most cases specially designed high-performance liquid chromatography (HPLC) columns are required and the yield is low. Isometric mixtures have been shown to be suitable for many applications including PDT [30].

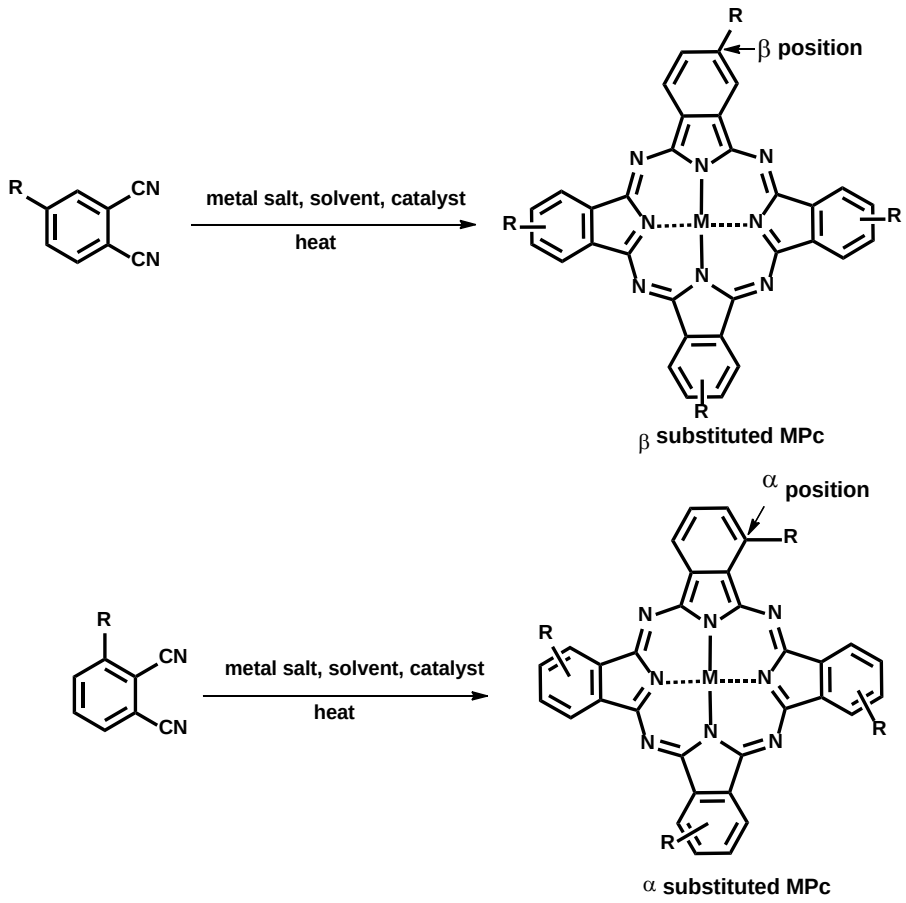

Scheme 1.1: Synthetic route for tetra-substituted MPcs (R represents the substituent)

The uniformity of substituents in symmetrical Pcs sometimes limits their application where specific binding with other ligands is desired. Hence efforts are made towards the design and synthesis of asymmetric Pcs with a unique substituent located at a specific position [31]. Asymmetry has been shown to be advantageous since it introduces distortions on the phthalocyanine macrocyle which affects the electronic states of the conjugated macrocycle [30]. This results in improved photophysical properties of the Pcs [32,33] which consequently is good for different applications including photodynamic therapy. Hence asymmetrical Pcs are employed in this work together with symmetrical ones.

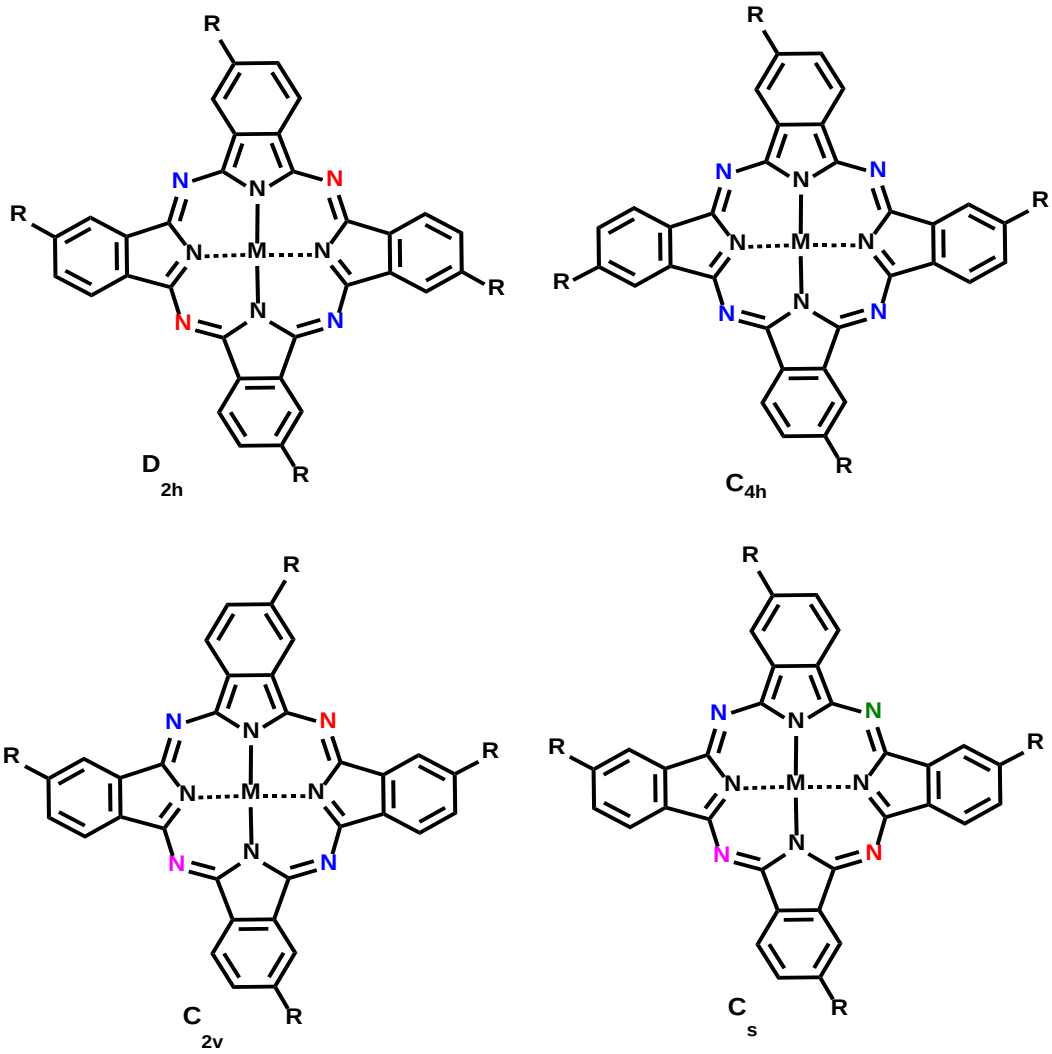

Figure 1.2: Constitutional isomers of tetrasubstituted phthalocyanines. (For each isomer symmetrically nonequivalent nitrogen atoms are shown in different colors and R represents the substituent).

Statistical condensation of two differently substituted phthalonitriles is generally utilised for the synthesis of A_3B-type asymmetrical Pcs, which are characterised by three identical (A) isoindole subunits and one different (B) subunit, **Scheme 1.2**. The phthalonitrile precursors are combined in mole ratios of 3:1 up to 9:1 (A:B) depending on the reactivity of the substituents [31,34–36].

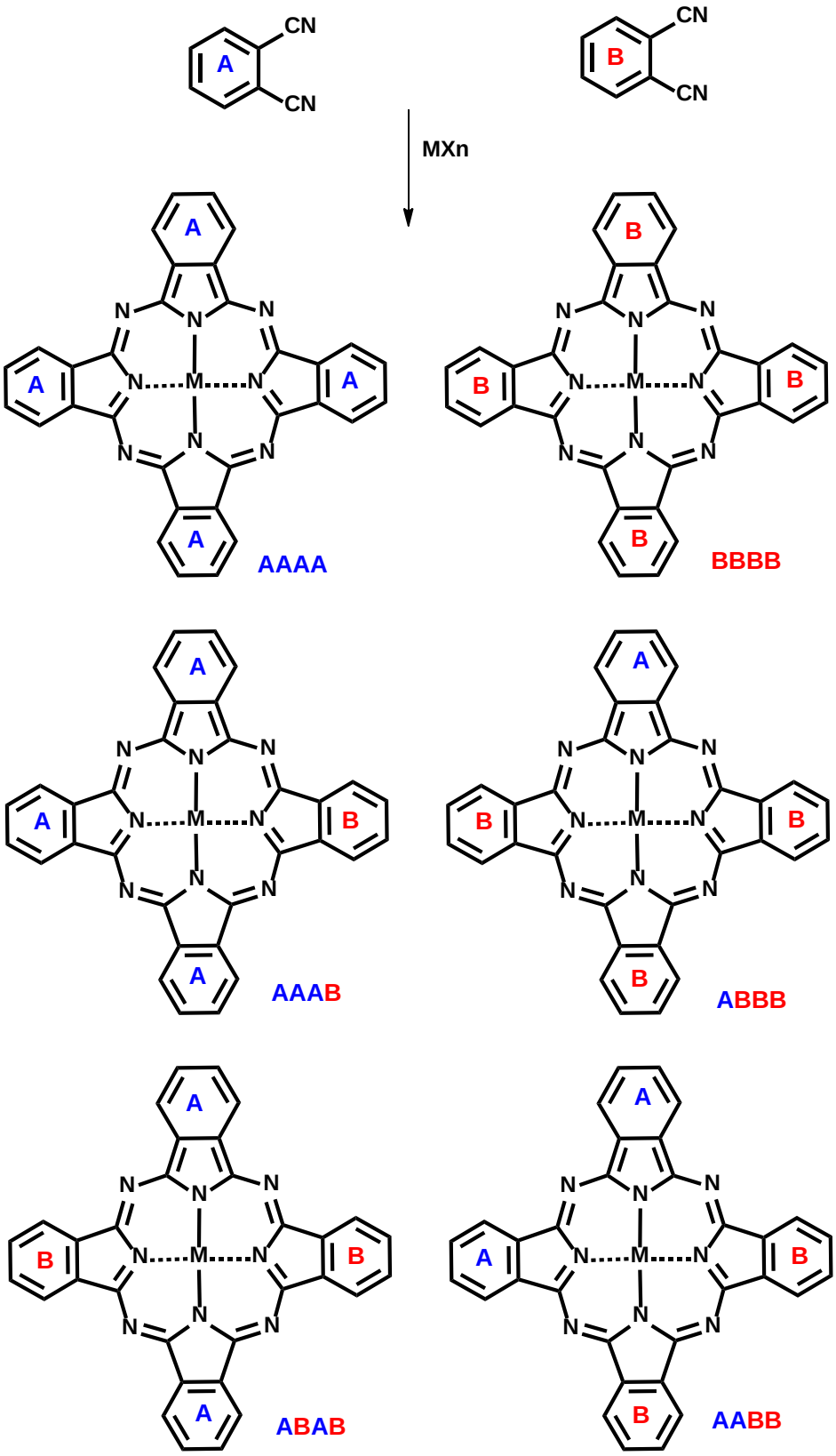

Scheme 1.2: Statistical mixed condensation products of phthalonitriles **A** and **B**.

A mixture of six products could be obtained as shown in **Scheme 1.2** and these are separated chromatographically to isolate the desired Pc (A_3B or AB_3).

1.1.3. MPcs synthesised and studied in this work

In this work both symmetrical and asymmetrical peripherally substituted MPcs are synthesised containing either zinc or indium as central metals and with carboxyphenoxy, phenoxy propanoic acid, benzothiazole phenoxy, thiophine ethoxy and di-*O*-isopropylidene-α-D-glucopyranose as ring substituents, **Table 1.1**. Complexes **1**, **3a**, **3b** and **4a** have been reported before [37–40]. However, their photophysical and photochemical behaviour in the presence of gold or gold silver alloy or gold speckled silica nanoparticles are explored for the first time. Complexes **2**, **4b**, **5**, **6**, **7** and **8** are reported here for the first time.

1.1.3.1. Choice of central metal.

Metal centres influence photophysical and photochemical properties of Pcs. In and Zn were chosen because they are diamagnetic hence they have a closed shell structure which results in enhanced photophysical properties. Additionally, as heavy atoms; they promote intersystem crossing to populate the triplet state through the spin orbit coupling (SOC). SOC (also termed heavy atom effect, HAE) is most prevalent in atoms whose nuclei are large and enhances the kinetics of both radiative and non-radiative transitions between states with different spin [41,42].

Table 1.1: MPcs and conjugates synthesised in this work

MPc	**Conjugate (bond formed)**
Symmetric MPcs	
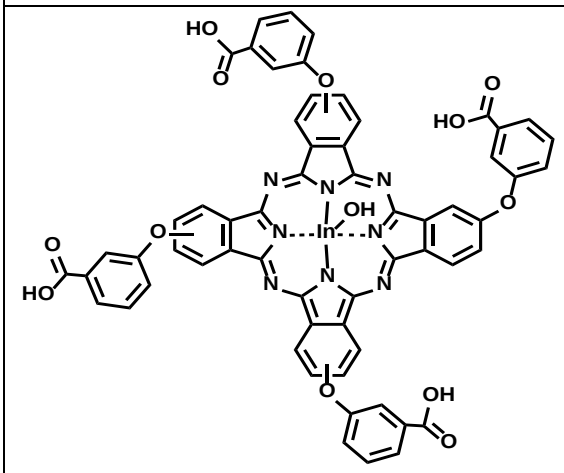 Indium(III) tetra–(3–carboxyphenoxy) phthalocyanine (**1**). [37]	**1**-Ag_1Au_3NSs-GSH **1**-Ag_3Au_1NSs-GSH **1**-Ag_3Au_1SiNSs- APTES (amide bond)
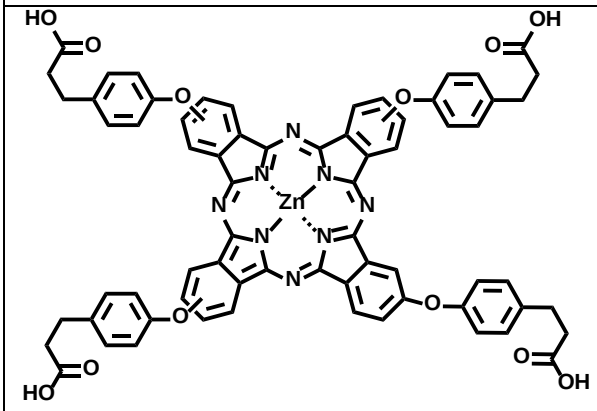 Zinc(II) tetra–[3-(4-phenoxy)propanoic acid] phthalocyanine (**2**). [New]	**2**-AuNTs-GSH **2**-AuNSs-GSH **2**-AgNSs -GSH **2**-Ag_3Au_1NSs-GSH (amide bond)

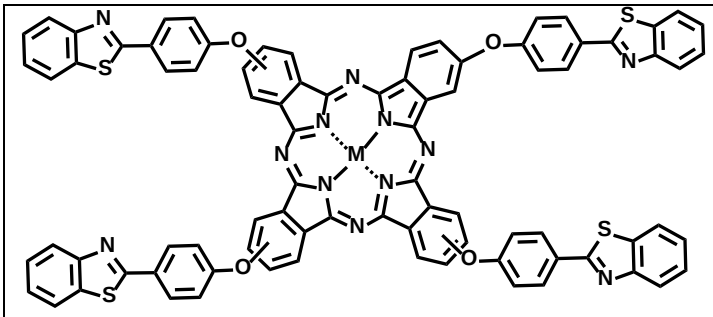 Zinc(II) [tetra-(benzothiazol-2-yl)phenoxy] phthalocyanine (**3a**). M= Zn [38] Indium(III) chloride [tetra-(benzothiazol-2-yl)phenoxy] phthalocyanine (**3b**). M= In(Cl) [39]	**3a**-AuNTs-CTAC **3a**-AuNSs-CTAB **3a**-GSS **3b**-AuNTs-CTAC **3b**-AuNSs-CTAB **3b**-GSS (PDT studies) (Au-S/Au-N bond)
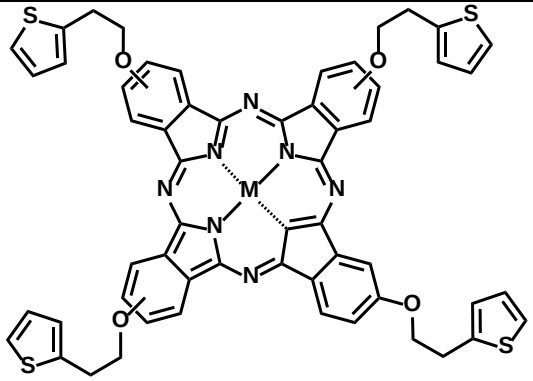 Zinc(II) tetra-(thiophine ethoxy) phthalocyanine (**4a**). M= Zn [40] Indium(III) chloride tetra–(thiophine ethoxy) phthalocyanine (**4b**). M= In(Cl) [New]	**4a**-AuNTs-CTAC **4a**-AuNSs-CTAB **4a**-GSS **4b**-AuNTs-CTAC **4b**-AuNSs-CTAB **4b**-GSS (Au-S bond)
Asymmetric MPcs	
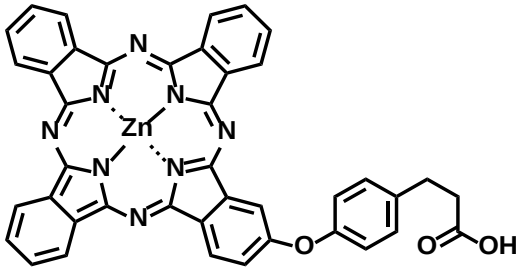 Zinc(II) mono–[3-(4-phenoxy)propanoic acid] phthalocyanine (**5**). [New]	**5**-AuNTs-GSH **5**-AuNSs-GSH **5**-AgNSs -GSH **5**-Ag_3Au_1NSs-GSH (amide bond)

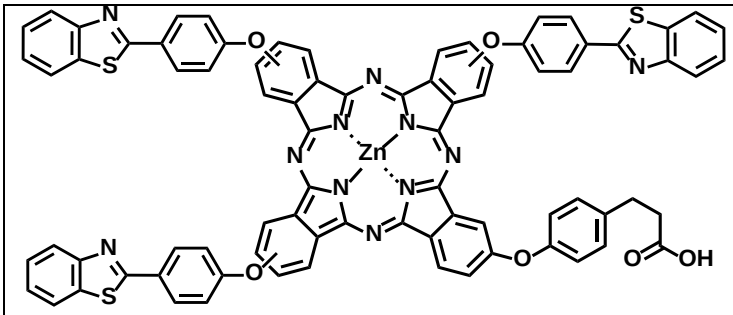 Zinc(II) [tris-(4-(benzothiazol-2-yl)phenoxy)- 3-(4-phenoxy)propanoic acid] phthalocyanine (**6**). [New]	**6**-AuNTs-CTAC **6**-AuNSs-CTAB **6**-AuCT (PDT studies) (Au-S/Au-N bond) **6**-CT (S-N bond) **6**-AuNTs-GSH **6**-AuNSs-GSH (amide bond)
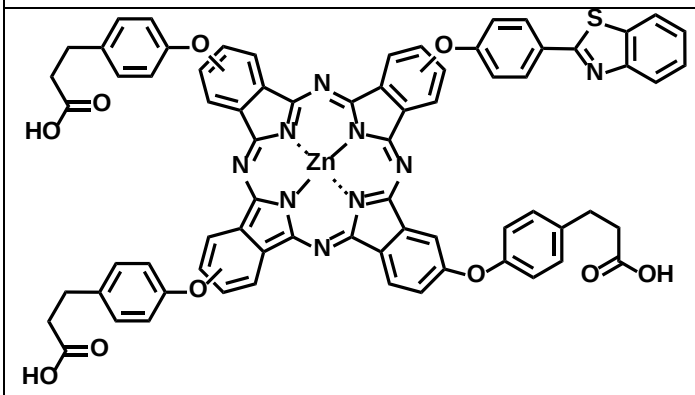 Zinc(II) [tris-(3-(4-phenoxy)propanoic acid)-4-(bezothiazol-2-yl) phenoxy] phthalocyanine (**7**). [New]	**7**-AuNTs-GSH **7**-AuNSs-GSH (amide bond: un published work) **7**-AuNTs-CTAC (Au-S/Au-N bond)
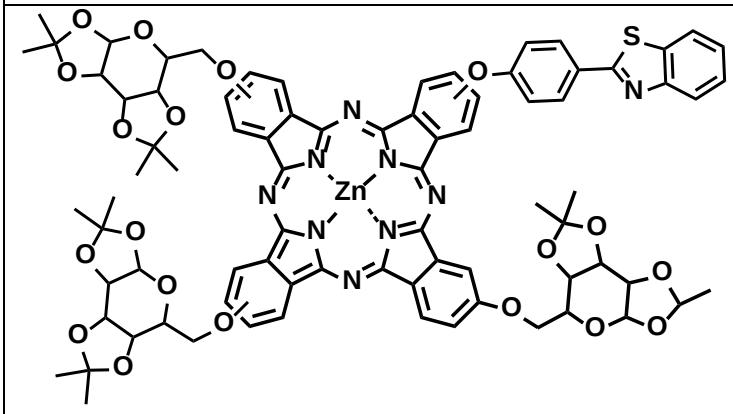 Zinc(II) [(tris- (2,2,7,7-tetramethyltetrahydro-3aH-bis([1,3] dioxolo)[4,5-b:4',5'-d]pyran-5-yl)methoxy)-2-(4-benzothiazol-2-yl)phenoxy] phthalocyanine (**8**). [New]	**8**-AuNRs-CTAB **8**-AuNSs-CTAB (Au-S/Au-N bond) (PDT studies)

The probability of intersystem crossing to triplet state thus increases with an increase in the atomic number of elements and this reduces fluorescence [43,44]. This makes heavy metals such as In and Zn a good choice as central metals in MPcs for PDT.

1.1.3.2. Choice of substituent.

Substituents greatly influence the behaviour of Pcs especially the photophysical and photochemical properties together with their applications [45,46].

i) The carboxyphenoxy (in complex **1**) was chosen as a ring substituent due to the promising PDT activity displayed by zinc tetra phthalocyanine with carboxyphenoxy groups [47].

ii) The phenoxy propanoic acid substituent (in complexes **2**, **5**, **6** and **7**) was chosen based on the fact that porphyrins containing propanoic acid (such as the Uroporphyrins) have been successfully employed for PDT [4] and in addition, phenyl rings are reported to contribute to effective population of the triplet state [48]. MPcs with a phenoxy propanoic acid substituent (both symmetric and asymmetric) are synthesised here for the first time.

iii) The benzothiazole phenoxy substituent (in complexes **3a**, **3b**, **6**, **7** and **8**) was chosen since benzothiazole derivatives have been found to have antitumor activities [49–51] which could be advantageous for PDT applications. Additional phenyl rings could also be an advantage as explained before.

iv) The thiophine ethoxy substituent (in complexes **4a** and **4b**) was used because of the reported anticancer potential of thiophene derivatives [52,53].

v) A saccharide (1,2:3,4-di-*O*-isopropylidene-α-D-glucopyranose) as a substituent (in complex **8**) was chosen for improved cell-uptake since cancer cells are known for increased glucose uptake and glycolysis to provide sufficient metabolic energy to sustain their proliferation. The glucose transporter proteins are over-expressed in a variety of human carcinomas [54] and glycoconjugation of MPc could enhance their cellular uptake and eventually the PDT efficacy.

1.1.3.3. Choice of the nanoparticle capping agent

In this work, glutathione (GSH) functionalised or cetyltrimethylammonium bromide/chloride (CTAB/CTAC) stabilised gold nanoparticles (spheres, AuNSs-GSH/AuNSs-CTAB; rods, AuNRs-CTAB and triangles, AuNTs-GSH/AuNTs-CTAC), silver nanospheres (AgNSs-GSH), gold-silver alloy nanospheres (Ag_3Au_1NSs-GSH and Ag_1Au_3NSs-GSH, numbers are mole ratios of Ag : Au in the alloy), gold-silver alloy coated with silica nanospheres and functionalised with aminopropyl triethoxylsilane (Ag_3Au1SiNSs–APTES), gold speckled silica nanoparticles (GSS), chitosan (CT) and a gold chitosan (AuCT), composite, **Figure 1.3**, were synthesised and attached to MPcs for possible application in PDT. **Table 1.1** shows the synthesised MPcs and their conjugates with nanoparticles.

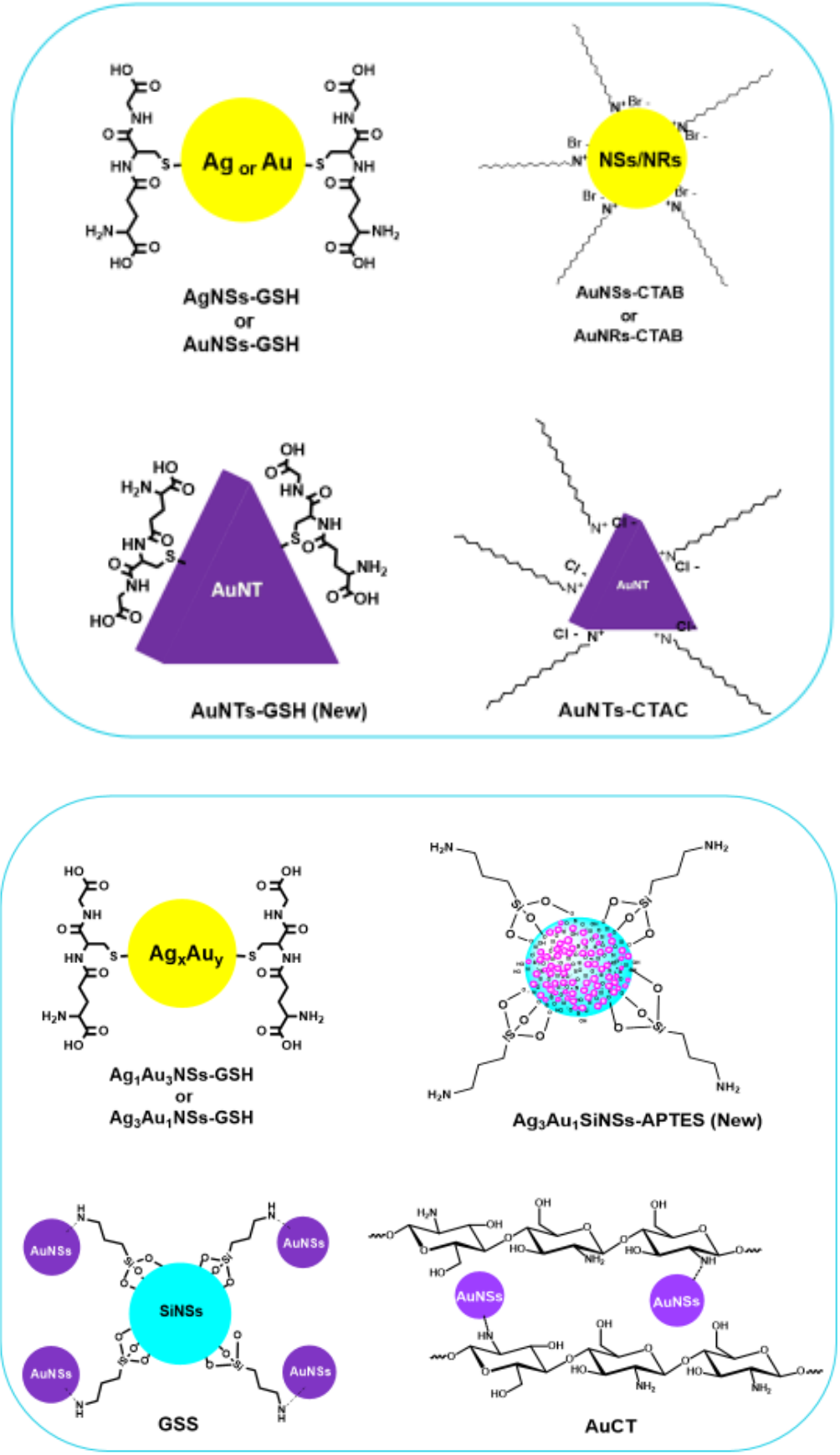

Figure 1.3: An illustration of nanoparticles used in this work.

The MPcs were linked to these NPs taking advantage of:

i) the high affinity of gold in the NPs for sulphur or nitrogen in the complexes. The complexes with thiophine (complexes **4a** and **4b**) or benzothiazole (complexes **3a**, **3b**, **6**, **7** and **8**) groups, were linked to AuNPs (either AuNSs-CTAB, AuNRs-CTAB or AuNTs-CTAC), GSS and AuCT, via a Au-S/Au-N bond.

ii) Complexes with carboxylic acid groups, were covalently linked to either glutathione functionalized NPs or aminopropyl triethoxylsilane functionalized NPs (Ag_3Au_1SiNSs–APTES; for complex **1**). GSH and APTES were used as capping bifunctional ligands for the NPs due to the availability of an amine moiety in their molecular structure which can foster amide bond formation with a –COOH containing phthalocyanine.

1.1.3.4. *Comparative Studies.*

The complexes alone and at times with NPs will be compared to study the effect of substituents, central metal and symmetry on the photophysical and photochemical properties. For asymmetric MPcs the effect of the number of substituents will also be compared.

i) Symmetrically substituted complexes **2**, **3a** and **4a** (with Zn as the central metal), will be compared for the effect of ring substituents on the photophysical and photochemical properties. The same applies for complexes **1**, **3b** and **4b** (with In as the central metal).

ii) Complexes **3a** and **3b**, **4a** and **4b** will be compared for the effect of the central metal on the photophysical and photochemical properties in the absence and in the presence of NPs. The same complexes will be compared for the effect of NPs shape and size. Complex **3b** and its conjugate with GSS will be used as an example for *in vitro* dark cytotoxicity and PDT activity against MCF-7 breast cancer cells.

iii) The effect of the number of propanoic acid groups on the photophysical and photochemical properties will be studied by comparing complexes **2** (with four phenoxy propanoic acid groups) and **5** (with one phenoxy propanoic acid group) when alone and with NPs.

iv) The effect of the number of benzothiazole phenoxy groups will also be compared using complexes **3a** (with four benzothiazole phenoxy groups), **6** (with three benzothiazole phenoxy groups and one phenoxy propanoic acid group) and **7** (with one benzothiazole phenoxy group and three phenoxy propanoic acid groups), with and without NPs. Complex **6** and its conjugate with AuCT (**6**-AuCT) will be used as an example for *in vitro* dark cytotoxicity and PDT activity.

v) Complexes **7** and **8**, with one common substituent (benzothiazole phenoxy group) will be compared for the effect of phenoxy propanoic acid versus di-*O*-isopropylidene-α-D-glucopyranose groups on the photophysical and photochemical properties. Complex **8** and its conjugates with AuNPs (AuNRs-CTAB, AuNSs-CTAB) will be used as an example for *in vitro* dark cytotoxicity and PDT activity against MCF-7 breast cancer cells.

vi) Complex **1**, with a carboxyphenoxy group, will be used to compare the effect of alloy nanoparticles on the photophysical and photochemical properties. This also applies for complexes **2** and complex **5.**

1.2. Photodynamic Therapy (PDT)

PDT is a clinically approved, minimally invasive cancer treatment which requires a photosensitizer (PS) and light of appropriate wavelength in the presence of ground state molecular oxygen to elicit selective destruction of the tumor cells [4]. The three components (a PS, visible light and molecular oxygen) are nontoxic when separate, however when the PS is activated by visible light, the excited PS reacts with molecular oxygen leading to the production of reactive oxygen species (ROS), capable of inducing stress on tumorigenic cells [4,55–57].

PDT is particularly useful for the treatment of early and localised tumours, due to the selective delivery of the PS to cancerous tissue [5,58]. However, complete cure of metastatic tumours is more challenging since irradiation of the whole body is not possible [5,59].

MPcs have proven to be an efficacious PS for PDT of cancer and some of them have been approved in countries such as Russia, United States of America and United Kingdom, for the treatment of cancer. **Figure 1.4** shows the phthalocyanines that are in clinical trials [60,61].

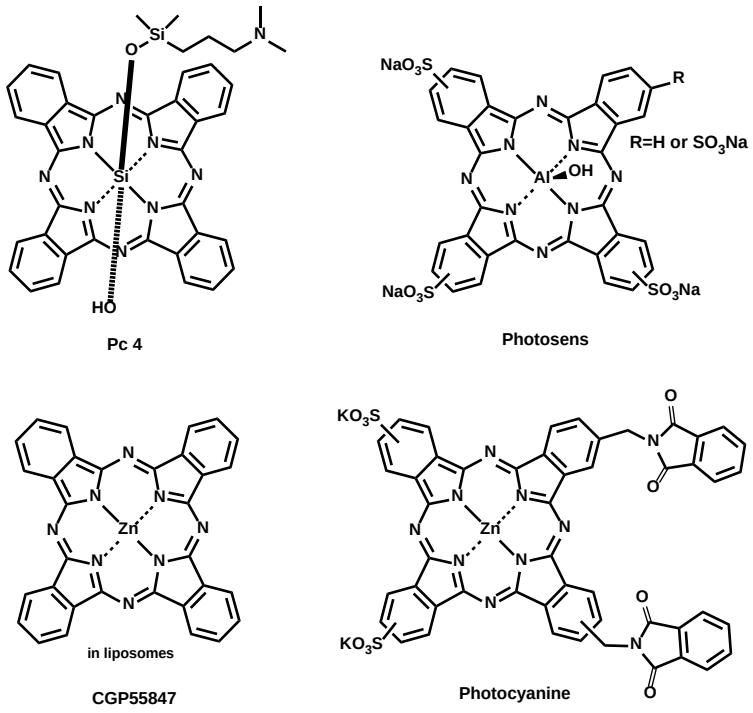

Figure 1.4: Some MPcs in clinical trials as PS for PDT.

1.2.1. PDT mechanisms when using MPcs as PS.

During photosensitisation as shown in **Scheme 1.3**, the MPc (as a PS) is irradiated with light of a specific wavelength, usually between 400-800 nm [57]. The MPc in the ground state (S_0) absorbs light, which provides energy for the MPc to reach an electronically excited singlet state (S_1). The S_1 state has an unstable and short half-life (10^{-9} s) [62], leading to fast deactivation through either radiative (such as fluorescence) or non-radiative processes, like intersystem crossing (ISC). Ideal MPcs undergo deactivation through ISC to a triplet excited state (T_1). The longer half-life (10^{-3} s) of the T_1 state [62] compared to S_1, allows for sufficient time for photosensitisation by the excited MPc.

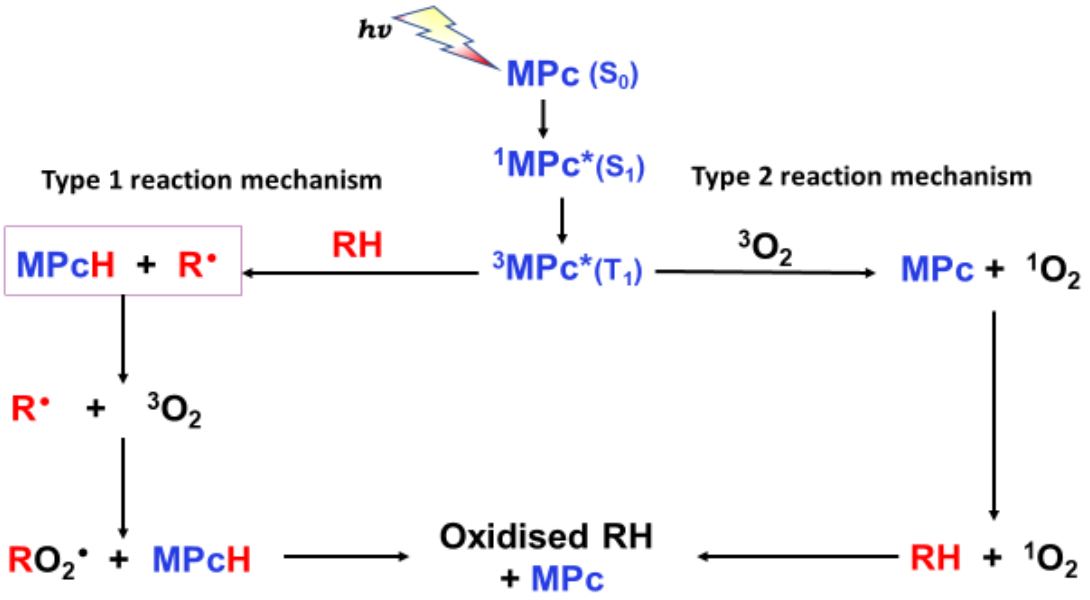

Scheme 1.3: Schematic representation of Type 1 and Type II photochemical reaction mechanisms.

Photosensitisation occurs in three ways, which are either Type I, Type II or Type III. Type I involves the interaction of the MPc in the T_1 state and a substrate (RH), resulting in electron or hydrogen transfer to form free radicals which react with molecular oxygen ($^3O_2$), to form an oxidised substrate.

Type II mechanism involves the transfer of energy from the MPc in the T_1 state to molecular oxygen, producing a highly reactive oxygen species, singlet oxygen ($^1O_2$) which induces oxidative stress in the cells [57,58,62,63]. Type II is the most common mechanism followed in PDT due to the high oxygen concentration in most tumors.

Type III reaction mechanism (Figure not shown), involves an electron transfer that occurs between the MPc in the T_1 state (^{3}MPc*) and the substrate resulting in an anionic MPc and a cationic substrate. Another electron transfer then occurs where the anionic MPc transfers an electron

to $^3O_2$ forming the superoxide anion, O_2^-. This transfer returns the MPc to its ground state. The superoxide anion and cationic substrate then interact to form the oxygenated product.

After photosensitisation, malignant cell death can be from direct photodamage, vascular shutdown and the activation of an immune response [58,59,64,65] if not all of them at once.

1.2.2. Nanoparticles in PDT.

In spite of the many successes recorded for the PDT activity of MPcs, there remain some limitations associated PS in general, and these include lack of selectivity and specificity towards cancer cells in comparison to healthy ones [62,66]. To address these limitations, various approaches have been explored. These include encapsulation of the PS in colloidal carriers (such as liposomes [67,68], polymeric micelles [69,70]) and conjugation of the PS to either antibodies [71], synthetic peptides [72], nanoparticles [73,74] or carbohydrates [75–80]. This work focusses on the linkage of MPcs to nanoparticles (NPs) for drug delivery, hence only nanoparticles will be discussed.

Nanoparticles are defined as materials with size ranging from 1 nm to 100 nm. They have been shown to effectively enhance the selectivity and specificity of PS for tumour cells, through enhanced permeability and retention (EPR) effects. EPR effect is a phenomenon by which molecules of certain sizes tend to selectively accumulate in solid tumor tissues but not in normal tissue (pore

size less than 10 nm) because of the abnormal leaky, disorganised and loosely-connected blood vessels (with pore sizes of 100-600 nm) in tumor tissues [81–84]. Additionally, the poor lymphatic drainage in tumours allows nanoparticles to be retained after internalisation due to the inability of tumours to renew and clean the interstitial fluid.

Nanoparticles as a result are ideal carriers of PS for PDT due to their tunable size that can be made to be between 10 nm-100 nm, allowing easy permeability through the pores of the leaky vasculature (and not normal tissue). These particles have additional advantages due to their unique size and shape dependent photophysical and photochemical properties as well as the extensive possibilities for size and shape control [81,85–87]. Their large surface area to volume ratio combined with ease of surface modifications allows for attachment to other molecules, hence they are utilised for various biomedical applications. Additionally, a high number of PS molecules can be accommodated, which increases the amount of PS loaded and delivered to the cancer cells, and results in enhanced production of $^1O_2$ and other ROS [85,87].

Additionally, metal nanoparticles can convert certain wavelengths of light into heat, since they contain electrons that are free to move throughout the metal. Depending on the size and shape of the nanoparticles, these free electrons absorb light energy, making the cloud of free electrons on the surface of the metal nanoparticles to resonate hence generating heat. As a result, metal

nanoparticles are utilised for photothermal therapy (PTT) of cancer. PTT can be combined with PDT [82,87] for synergistic destruction of tumorigenic cells.

1.2.3. Nanoparticles linked to Pcs

The nanoparticles: AuNSs, AuNRs, AuNTs, AgNSs, gold-silver alloy, GSS, CT and a AuCT composite have been used before [88–109] for various applications including photothermal therapy (PTT), as shown in **Table 1.2**.

Table 1.2: Nanoparticles synthesised in this research work and their applications

Nanoparticle	Application of NPs
AuNPs:	
Spheres, Rods	Bioimaging, Biosensing, photothermal therapy, Catalysis, drug delivery, PDT, PACT [88,89,100,103].
Triangles	Vapour sensing catalysis, photothermal therapy [104,105].
AgNPs	Wound dressing, water purification, catalysis [106–108].
Gold- silver alloys (Ag_xAu_y)	Catalysis, bioanalysis, nonlinear optics, antitumor activity [90–92,109].
Ag_3Au_1SiNSs–APTES	New
Gold speckled silica NPs (GSS)	Photothermal therapy, bioimaging [93,94].
Chitosan (CT)	Antitumour activity, drug delivery [95–97].
Gold Chitosan (AuCT)	Catalysis, Sensing, PTT [98,99,101,102].

Table 1.3 shows the reported Pcs which have been linked to NPs employed in this work, together with their applications [72, 108-129].

Table 1.3: Examples of various Pcs and their conjugates to the nanoparticles for different applications

Pcs	**NPs (bond formed)**	**Application**	**Ref**
MPc-AuNPS			
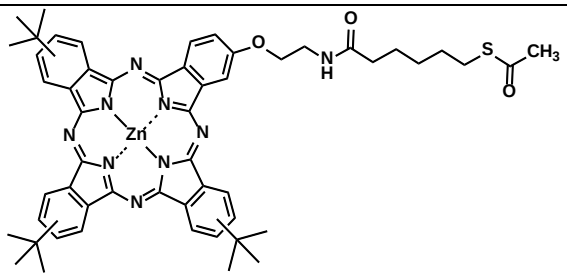 **9**	Spheres (Au-S)	Dye-sensitized solar cells (DSSCs)	[110]
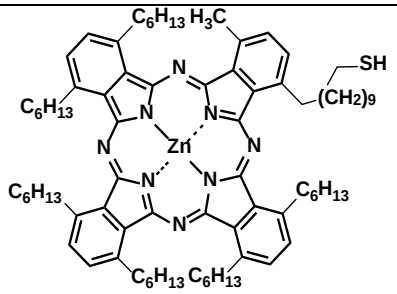 **10**	Spheres (Au-S)	Photochemistry PDT	[72, 109]
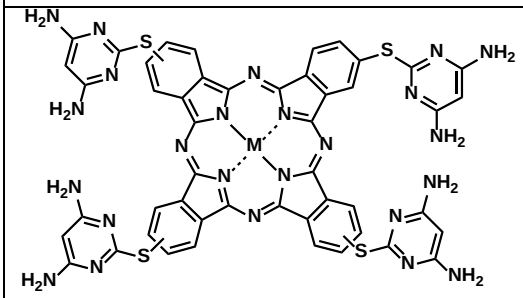 **11a. M= Zn** **11b. M= In**	Spheres (Au-N)	Photophysics Photochemistry	[112]
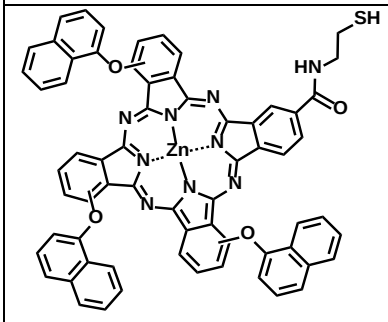 **12**	Spheres (Au-S)	Photophysics Photochemistry	[113]

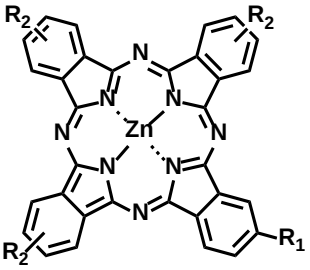 13. 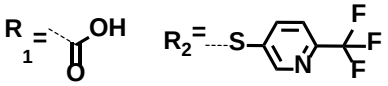 14. 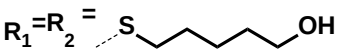	Spheres (Au-S/Au-N)	Photophysics Photochemistry	[113]
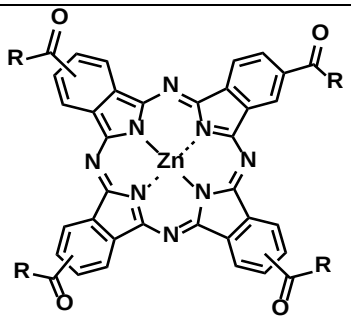 15. R = O^- 16. R = $CH_2(CHOH)_4CH_2N^-CH_3$	Positively charged CTAB coated rods (mixture: electrostatic interactions)	PDT	[114]
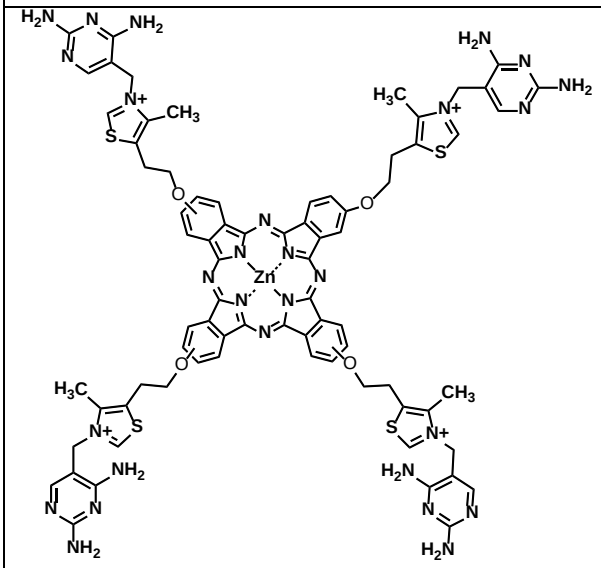 17	rods (Au-S/Au-N)	Photophysics	[115]

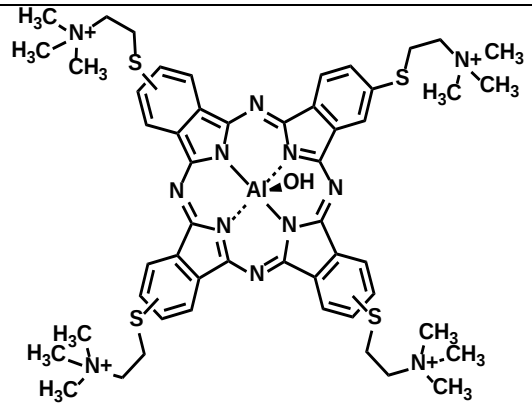 **18**	rods bipyramids (Au-S)	PACT	[116]
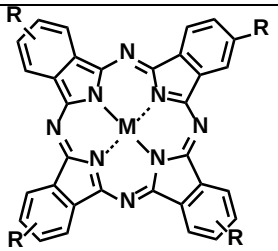 **19a. M= Al(Cl); R= SO_3^-** **19b. M= Al(OH); R= SO_3Na** **19c. M= Zn; R= SO_3Na** **20. M= Zn; R= SCH_2CH_2COOH** **21. M= Zn; R= SCH_2COOH**	stars spheres rods (mixture: electrostatic interactions)	Photophysics, PDT and PTT	[117, 118]
MPc-AgNPS			
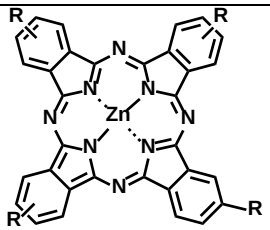 **22. R =** 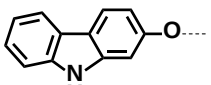 **23. R = NH_2**	Spherical AgNPs (Ag-N)	photocatalysts for degrading organic pollutants.	[119, 120]
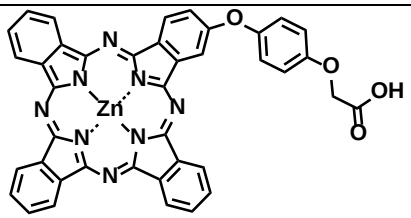 **24**	Spherical AgNPs cysteamine capped (amide)	PDT	[121]

MPc-gold- silver alloys			
11a	Spherical Ag_3Au_1 and Ag_1Au_3NPs (Au-S/Au-N)	Non linear optics	[122]
19b	Spherical AuAg-NPs (mixture: electrostatic interactions)	PACT	[123]
24	Spherical AgAu NPs cysteamine capped (amide)	PDT	[121]
MPc-CT and MPc-AuCT composite			
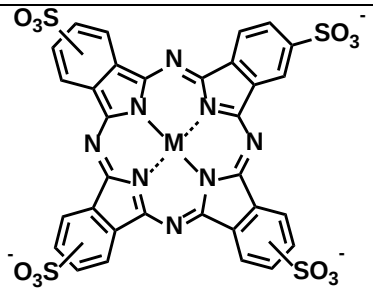 **25. M= Ni** **26. M= Cu** **27. M= Fe** **28. M= Co**	Spherical CT (for **25**-**28**) (mixture)	sensing, catalysis, photocatalysis (degradation of pollutants).	[124 – 126]
	AuCT (for CoPc (**28**) only) (mixture: electrostatic interactions)	catalysis	[127]

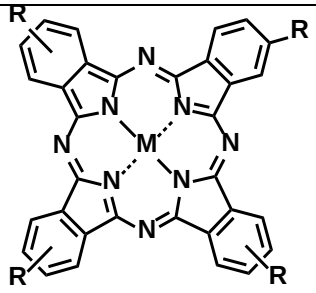 **29. M= H_2, R=H** **30. M= Zn, R= NH_2** **31. M= Zn, R= H** **32. M= Zn, R= O(C_6H_4)CHO**	CT-TiO_2 (for H_2Pc (**29**) only)	catalysis	[128]
	CT (for **30**-**32**) (mixture)	cell cytoxicity, antibacterial, catalysis,	[120, 129, 130]
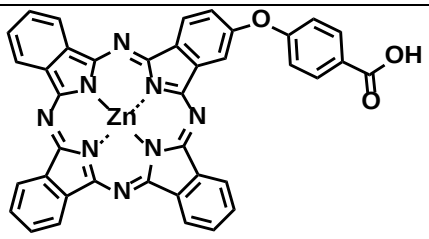 **33**	CT (mixture)	PDT	[131]

As shown in **Table 1.3**, AuNTs and GSS nanoparticles have never been linked to Pcs and their linkage to Pcs is reported in this work for the first time. AuNTs are good for PDT since they have shown better cellular uptake compared to other anisotropic nanoparticles (order of cellular uptake efficiency: triangles > rods> stars) [132]. GSS nanoparticles have shown some photothermal therapy (PTT) effect [93] which might bring a synergistic effect of PDT and PTT when they are linked to MPcs for cancer treatment.

On the other hand, very few asymmetric Pcs have been linked to NPs (especially gold containing NPs) and tested for *in vitro* dark cytotoxicity and PDT activity. In this work the linkage of novel asymmetric MPcs to NPs containing gold, together with *in vitro* dark cytotoxicity and PDT activity is reported.

Also shown in **Table 1.3**, is that very few gold silver alloy nanoparticles have been linked to Pcs. Alloying reduces the toxicity of silver in biomedical applications and encapsulating the alloy with non-toxic amorphous silica is expected to effectively eliminate the toxic effects of silver. In this work the silver rich alloy (Ag_3Au_1) nanospheres were coated with aminopropyl triethoxylsilane (APTES) functionalised silica nanospheres for the first time. The NPs (Ag_3Au_1SiNSs–APTES) were further linked to an MPc (complex **1**) via an amide bond.

Mixtures of AuCT with MPcs have been used before (**Table 1.3**), however the linkage of an asymmetric Pc to AuCT via a Au-S interaction is reported in this work for the first time.

1.3. Choice of nanoparticles used in this work

The size and shape of NPs can influence the physichochemical properties of a material, leading to different applications [133], hence different shapes are employed in this work.

1.3.1. Gold Nanoparticles

Gold nanoparticles (AuNPs) exhibit unique optical, chemical, and biological properties hence they are of clinical interest in several applications including drug delivery. The attractive features of gold nanoparticles are their surface plasmon resonance, the controlled manner in which they interact with thiol and nitrogen groups, biocompatibility and the tunability of properties by changing the particle size, shape and surface chemistry [134–136]. These attributes are exploited to provide an effective multifunctional platform for imaging and diagnosis of diseases and to selectively deliver therapeutic agents [88,137,138] as indicated in **Table 1.2**. The use of gold nanoparticles can also increase the stability of the drugs.

Despite the extensive reports on the advantages of anisotropic particles over nanospheres, there is still limited research on the linkage of drugs like phthalocyanines to anisotropic gold nanoparticles. As stated above and as shown in **Table 1.3**, Pcs have been linked to gold nanospheres and a few to nanorods. There are no reports on linkage to nanotriangles. Hence in this work, the conjugates of MPcs to gold nanorods and triangles are compared to their nanosphere counterparts.

The shape of nanoparticles has been reported to influence the delivery system of drugs. Non-spherical (anisotropic) particles exhibit significant advantages over their spherical counterparts. Anisotropic particles exhibit desirable properties such as enhanced circulation time and efficient tumor penetration. The anisotropic nanoparticles stick to the surface of a tumor longer than a spherical shaped nanoparticles, providing more efficient transfer of therapeutic drugs to the tumor [139,140].

In this work gold nanotriangles (AuNTs-CTAC and AuNTs-GSH represented in **Figure 1.3**) are linked to MPcs (complexes **3a**, **3b**, **4a**, **4b**, **6** and **7** for AuNTs-CTAC; complexes **2**, **5**, **6** and **7** for AuNTs-GSH) for the first time.

1.3.2. Silver (AgNSs) and silver-gold alloy nanospheres (Ag_3Au_1NSs and Ag_1Au_3NSs)

Silver nanoparticles (AgNPs) just as AuNPs exhibit unique optical, chemical, and biological properties making them attractive for biomedical applications. However, the silver surface easily oxidizes under ambient conditions reducing its plasmonic performance and also making it toxic due to the rapid dissolution of the surface oxide layer releasing Ag^+ ions [141,142]. This prohibits the use of nanosilver in biomedical applications where inert materials are sought.

To minimize the toxicity of silver nanoparticles and reduce the use of expensive gold, alloy (bimetallic) nanoparticles have been used alternatively

in biomedical applications [143]. These bimetallic nanoparticles exhibit unique catalytic, electronic and optical properties distinct from those of the corresponding metallic particles. Alloyed silver–gold nanoparticles, resist surface oxidation making them applicable for drug delivery. The toxicity of silver can also be reduced by encapsulating it with non-toxic amorphous silica to reduce Ag+ ion release and direct nanosilver contact with biological systems [144,145]. It is for this reason that the Ag_3Au_1NSs were encapsulated with silica nanospheres (SiNSs). Hence, in this work the effects of AgNSs-GSH, AuNSs-GSH, Ag_3Au_1NSs-GSH, Ag_1Au_3NSs-GSH and Ag_3Au_1SiNSs–APTES, represented in **Figure 1.3**, on the photophysicochemical behaviour of MPcs are evaluated. The synthesis of Ag_3Au_1SiNSs–APTES (the subscripts are the mole ratios) and their linkage to an MPc (complex **1**) is reported for the first time.

1.3.3. Gold speckled silica nanoparticles

As stated above, gold and silica nanoparticles have attracted attention in biomedical applications, due to their excellent biocompatibility, and ease of surface modification [146–150]. A hybrid of gold and silica nanoparticles, represented in **Figure 1.3**, termed gold speckled silica (GSS) nanoparticles consist of a silica core with discontinuous, irregular specks of nanogold on the surface and within the pores of the silica matrix.

The dielectric–metal interfaces enables the GSS nanoparticles to absorb a broad spectrum of light from the visible to near infra-red regions—facilitating their use as photothermal therapy agents. These nanoparticles have demonstrated high thermal stability and good PTT *in vitro* using the lung A549 cancer cell lines [93]. The localized rise in the temperature of GSS particles leads to the rapid injury and death of the cancer cells [151]. Gold nanoparticles on their own are photothermally unstable, gradually losing their photothermal converting capacity upon repetitive near infrared irradiation [152,153] making the use of GSS advantageous. Since both silica and gold are generally regarded as safe biomaterials, with gold–silica nanoshells currently undergoing early phase clinical trials [93], the combination of silica and gold in GSS nanoprticles hold potential for use in both photothermal therapy and drug delivery for photodynamic therapy. Hence in this work GSS nanoparticles are linked to MPcs (complexes **3a**, **3b**, **4a** and **4b**) for the first time to assess their singlet oxygen generation capacity and the PDT activity.

1.3.4. Gold chitosan composite.

Chitosan (CT), a polysaccharide composed of glucosamine and *N*-acetylglucosamine, is biocompatible, biodegradable, bioactive, mucoadhesive and has several functional groups making it an excellent candidate for diverse biomedical and pharmaceutical applications including drug delivery [154–156], **Table 1.2**. The amino groups in chitosan easily interact with metal nanoparticles. Due to the affinity of gold for nitrogen, gold nanoparticles can be easily supported on chitosan using Au-N interactions, **Figure 1.3**. The CT

amine group is protonated and positively charged in slightly acidic solution, making it to easily form complexes with oppositely charged materials and it solubilises in aqueous environments.

Chitosan has demonstrated antitumor activity suggested to be due to its ability to induce cytokines production through increased T-cell proliferation and strong pro-apoptotic effects against tumor cells. In drug delivery chitosan and its derivatives improve drug absorption, stabilize drug constituents for drug targeting in addition to drug release enhancement [157]. As shown in **Table 1.3**, chitosan and the gold chitosan composite have been mixed with Pcs before [120,124–131], however this work reports their linkage to an asymmetric MPc (complex **6**) via Au-S/Au-N self-assembly for PDT. The *in vitro* dark cytotoxicity and PDT studies of the MPc (complex **6**) alone and when linked to AuCT are reported here for the first time.

1.4. Photophysicochemical Parameters

The photophysical properties of phthalocyanines determine their applicability as photosensitizers in different areas including PDT. These properties are measured by the changes in the electronic states when light is absorbed. The Jablonski diagram (**Figure 1.5**), illustrates the processes that occur on absorption of light by a photosensitizer. Briefly, the photosensitiser molecule,

in this case the phthalocyanine, in its singlet ground state (S_0) absorbs light energy and get excited to the singlet excited state (S_1).

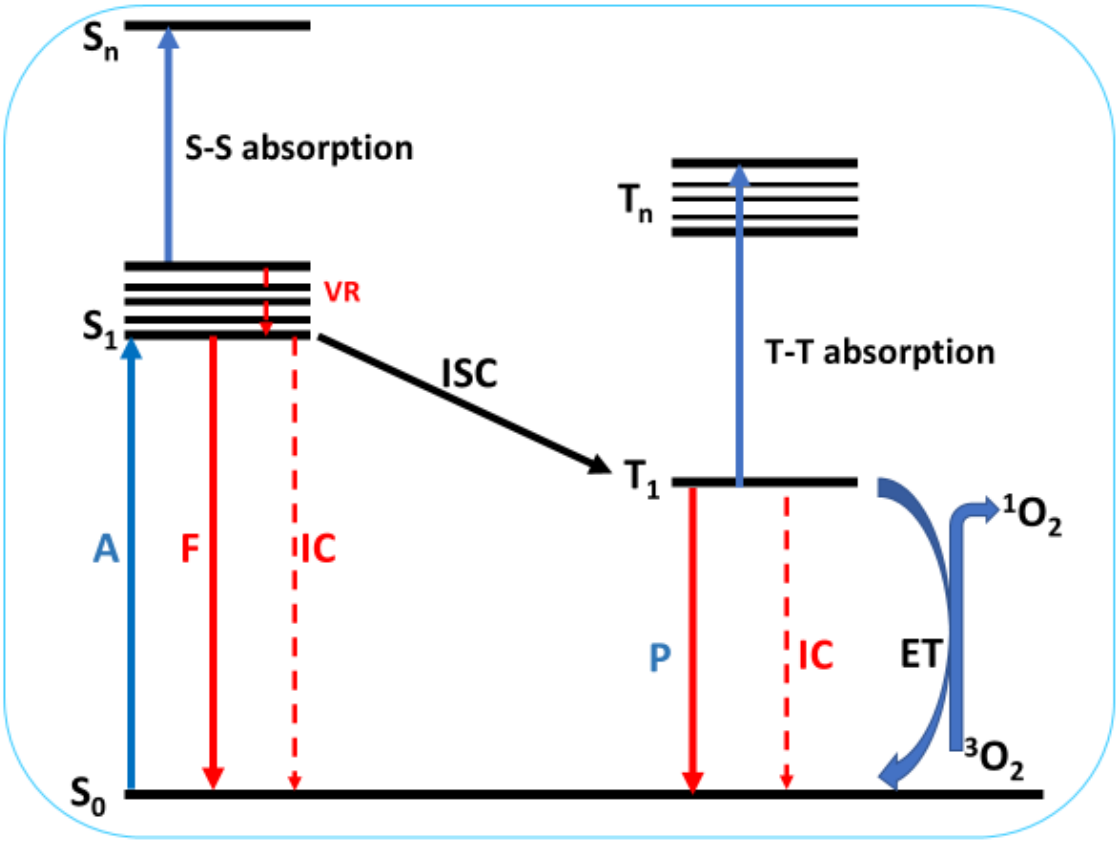

Figure 1.5: A modified Jablonski diagram showing the transitions between ground state (S_0) and electronic excited states (S_1 and T_1). S_1= singlet excited state, T_1= first triplet state, A= absorption, F= fluorescence, IC = internal conversion, VR= vibrational relaxation, ISC= intersystem crossing, P= phosphorescence, ET = energy transfer, S-S absorption=excited state singlet to singlet absorption and T-T absorption= excited state triplet to triplet absorption.

In the S_1 excited state it can either revert to the singlet ground state by releasing a photon of light via vibrational relaxation resulting in fluorescence (F), or it can undergo intersystem crossing (ISC) to the triplet state, T_1 [158–

160]. The photosensitiser transfers energy from the excited triplet (T_1) to ground state molecular oxygen ($^3O_2$) generating a reactive singlet oxygen ($^1O_2$) species that destroys cancers cells [4].

The photophysicochemical parameters of phthalocyanines are fluorescence quantum yield (Φ_F) and lifetime (τ_F), triplet quantum yield (Φ_T) and lifetime (τ_T) and the singlet oxygen quantum yield (Φ_Δ). These are important in the determination of the suitability of the molecules as photosensitisers [161,162].

1.4.1. Fluorescence quantum yields (Φ_F)

The fluorescence quantum yield (Φ_F) is defined by the ratio of the number of photons emitted to the number of photons absorbed. The fluorescence quantum yield values are determined using a comparative method [163,164] where the emission spectrum of a sample is compared with that of a standard on excitation at the same wavelength. The Φ_F are calculated according to Equation 1.1.

$$\Phi_F = \Phi_{F(Std)} \frac{F.A_{Std.}n^2}{F_{Std.}A.n_{Std^2}} \qquad (1.1)$$

where F and F_{Std} are the areas under the fluorescence curves of the sample and the standard, respectively. A and A_{Std} are the absorbances of the sample and standard at the excitation wavelength, and n and n_{Std} are the refractive indices of the solvents used for the sample and standard, respectively. Φ_{Fstd}

is the fluorescence quantum yield of the standard and unsubstitued zinc phthalocyanine (ZnPc) in DMSO (Φ_F = 0.2 [46]) was used as a standard. Factors such as the nature of solvent used, pH, aggregation, temperature, nature of central metal, concentration, nature of substituents and point of substitution have been reported to influence the Φ_F of MPcs.

The fluorescence life-time (τ_F),) is the average time a molecule spends in its excited singlet state before reverting to the ground state through fluorescence. The time-correlated single-photon counting (TCSPC) technique [165,166] was used to determine the τ_F values of all the MPcs and their conjugates studied in this work.

1.4.2. Triplet quantum yields

The triplet quantum yield (Φ_T) measures the fraction of absorbing MPcs that undergo rapid intersystem crossing (ISC) from the lowest excited singlet state to populate the lowest excited triplet state (T_1). The triplet lifetime is the amount of time it takes the triplet state to be completely depopulated and is indicative of the available time for the triplet state MPcs to transfer energy to ground state molecular oxygen or other substrates.

A comparative method [167,168] using a standard was used for triplet quantum yields determination based on triplet decay, using equation 1.2.

$$\Phi_T = \Phi_T^{Std} \frac{\Delta A_T \varepsilon_T^{Std}}{\Delta A_T^{Std} \varepsilon_T} \qquad (1.2)$$

where, Φ_T^{Std} is the triplet state quantum yield for the standard and unsubstituted ZnPc was used as a standard in DMSO (Φ_T^{Std} = 0.65) [167]. ΔA_T and ΔA_T^{Std} are the changes in the triplet state absorbance of the sample and the standard, respectively. ε_T and ε_T^{Std} are the triplet state molar extinction coefficients for the sample and standard, respectively.

To determine ε_T and ε_T^{Std}, the molar extinction coefficients of the ground singlet state of samples (ε_S), standard ($\varepsilon_S{}^{std}$) and the respective changes in triplet state absorbances of samples (ΔA_T) and standard ΔA_T^{Std} are used according to equation 1.3 and 1.4.

$$\varepsilon_T = \varepsilon_s . \frac{\Delta A_T}{\Delta A_s} \qquad (1.3.)$$

$$\varepsilon_T^{std} = \varepsilon_S^{std} . \frac{\Delta A_T^{std}}{\Delta A_S^{std}} \qquad (1.4)$$

The triplet lifetimes are obtained from the triplet decay curve by fitting using Origin Pro 8 software.

1.4.3. Singlet oxygen quantum yield (Φ_Δ)

Singlet oxygen ($^1O_2$) is a highly reactive oxygen species that is the primary cytotoxic agent in PDT [169]. It is formed through an energy transfer process between an excited triplet state of the MPc and ground state molecular oxygen ($^3O_2$), **Figure 1.5**.

The singlet oxygen generation may be experimentally determined by a chemical method that utilises singlet oxygen quenchers [170]. The singlet oxygen quenchers react with singlet oxygen (**Scheme 1.4**) as soon as it is produced in an oxygenated MPc solution. The depletion of the singlet oxygen quencher is spectroscopically monitored over predetermined time intervals to assess the singlet oxygen produced by the PS. Singlet oxygen quenchers such as 1,3 diphenylisobenzofuran (DPBF) or anthracene-9,10-bismethylmalonate (ADMA) (**Scheme 1.4**) can be used to quantify singlet oxygen production in organic solvents and aqueous solutions, respectively [171,172]

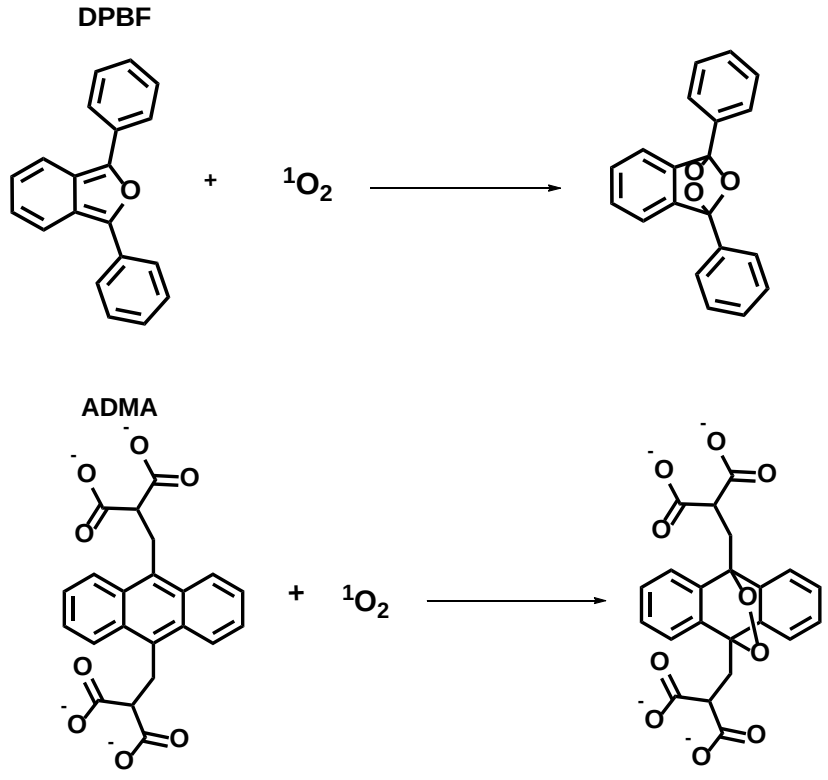

Scheme 1.4: Reaction of singlet oxygen with DPBF and ADMA.

The relative method is used for singlet oxygen quantum yield calculations, using equation 1.5.

$$\Phi_{\Delta} = \Phi_{\Delta}^{Std} \frac{R\, I_{abs}^{Std}}{R^{Std}\, I_{abs}} \qquad (1.5)$$

where Φ_{Δ}^{Std} is the singlet oxygen quantum yield for the standard (ZnPc, Φ_{Δ}^{Std} = 0.67 in DMSO [172] or aluminium sulfonated phthalocyanine (AlPcSmix; mixture of sulfonated phthalocyanine derivatives), Φ_{Δ}^{Std} = 0.42 in aqueous solutions) [173].

R and R^{Std} are the DPBF/ADMA photobleaching rates in the presence of the sample under investigation and the standard respectively. I_{abs} and I_{abs}^{Std} are the rates of light absorption by the sample and the standard, respectively and are determined by equations 1.6 and 1.7 [174].

$$I_{abs} = \frac{\alpha.\mathrm{A}.I}{N_A} \qquad (1.6)$$

$$I_{abs}^{std} = \frac{\alpha.\mathrm{A}.I}{N_A} \qquad (1.7)$$

where $\alpha = 1\text{-}10^{-A(\lambda)}$, $A(\lambda)$ is the absorbance of the sensitizer at the illumination wavelength, A is the illuminated cell area (expressed in cm^2), I is the intensity of light (expressed in photons $cm^{-2}s^{-1}$) and N_A is the Avogadro's constant [173–175]

1.5. Summary of aims

The aims of this thesis include:

- Synthesis and characterization of symmetrical and asymmetrical, metallophthalocyanines with carboxyphenoxy, phenoxy propanoic acid, benzothiazole phenoxy, di-*O*-isopropylidene-α-D-glucopyranose and thiophine ethoxy as substituents.
- Synthesis of nanoparticles (Ag_1Au_3NSs-GSH, Ag_3Au_1NSs-GSH, Ag_3Au_1SiNSs-APTES, AuNTs-GSH, AuNSs-GSH, AuNTs-CTAC, AuNSs-CTAB, AuNRs-CTAB, AgNSs-GSH and GSS) and a AuCT composite.
- Conjugation of metallophthalocyanines to nanoparticles, CT and a AuCT composite.
- Study the spectroscopic (ground state electronic absorption, excitation and emission) properties of the synthesised MPcs when alone and when linked to NPs or CT or AuCT.
- Study the photophysical (fluorescence quantum yield and lifetime, triplet quantum yield and lifetime) and photochemical (singlet oxygen quantum yield) properties of the synthesised MPcs when alone and when linked to NPs or CT or AuCT.
- *In vitro* dark cytotoxicity and photodynamic therapy activities of selected MPcs and conjugates against MCF-7 breast cancer cells.

CHAPTER TWO

2. Experimental Section

This chapter gives details of the materials, instrumentation and experimental procedures used for the synthesis and characterisation of the complexes, nanoparticles, and their conjugates studied, together with *in vitro* dark cytotoxicity and PDT studies.

2.1 Materials

2.1.1 Solvents

Dimethyl sulfoxide (DMSO, spectroscopy grade), 1–pentanol, 1-choloro naphthalene, deuterated (DMSO-d_6, chloroform-d), 1–hexanol and 25% ammonium hydroxide were obtained from Sigma Aldrich®. Absolute ethanol (EtOH), methanol (MeOH), dimethylformamide (DMF), cyclohexane, tetrahydrofuran (THF), nitric acid (55%), acetonitrile, acetone and toluene were obtained from SAARCHEM®. Ultra–pure water was obtained from a Milli–Q Water System (Millipore Corp, Bedford, MA, USA).

2.1.2 Reagents

Reagents for phthalonitrile precursors, phthalocyanines, nanoparticle syntheses and conjugation to NPs, chitosan and gold chitosan.

3-(4-Hydroxyphenyl)-propionic acid, potassium carbonate, zinc(II) acetate dihydrate, indium(III) chloride, 1,8-diazobicylo[5.4.0]undec-7-ene (DBU), unsubstituted zinc phthalocyanine (ZnPc), 1,2–dicyanobenzene, N,N'-dicyclohexylcarbodiimide (DCC), 4-(dimethylamino)pyridine (DMAP), 1,3-diphenylisobenzofuran (DPBF), chitosan (CT), silica gel, anthracene-9,10-bis-methylmalonate (ADMA), glutathione (GSH), Triton X 100, tetraethyl orthosilicate (TEOS), gold(III) chloride trihydrate, silver acetate, (3–aminopropyl)–triethoxysilane (APTES), diphenyl ether (DPE), potassium hydroxide pellets, oleylamine (OLA) and oleic acid (OA) were purchased from Sigma–Aldrich. The syntheses of 4-nitrophthalonitrile [176], 4-glycosylated phthalonitrile [80], 4-[4-(benzothiazol-2-yl)phenoxy] phthalonitrile [39], 4-(2-(2-thienyl)ethoxy)phthalonitrile [40] and aluminium sulfonated

phthalocyanine (AlPcSmix- mixture of sulfonated phthalocyanine derivatives) [177] have been reported in the literature .

Reagents for *in vitro* dark Cytotoxicity and PDT activity

Cultures of epithelial breast cancer cells (MCF-7 cells) were obtained from Cellonex. Trypsin ethylenediaminetetraacetic acid (EDTA), trypan blue, Dulbecco's phosphate-buffered saline (DPBS) and Dulbecco's modified Eagle's medium (DMEM) were obtained from Sigma Aldrich, heat-inactivated fetal calf serum (FCS), neutral red cell proliferation reagent (WST-1), and 100 µg/mL-penicillin-100 unit/mL-streptomycin-amphotericin B mixture were obtained from Lonza (Biowest).

2.2. Equipment

i) Proton-nuclear magnetic resonance (^{1}H NMR) spectra were recorded on a Bruker AVANCE II 600 MHz NMR spectrometer using tetramethylsilane (TMS) as an internal reference.

ii) Elemental analyses of MPcs were carried out using a Vario-Elementar Microcube ELIII CHNS instrument analyzer.

iii) Mass spectra data were acquired on a Bruker AutoFLEX III Smart-beam TOF/TOF mass spectrometer using α-cyano-4-hydrocinnamic acid as the matrix.

iv) Infrared spectra were acquired on a Bruker ALPHA FT–IR

spectrometer with universal attenuated total reflectance (ATR) sampling accessory.

v) Ground state electronic absorption was measured using a Shimadzu UV-2550 spectrophotometer.

vi) Fluorescence excitation and emission spectra were measured on a Varian Eclipse spectrofluorimeter using a 360–1100 nm filter. Excitation spectra were recorded at the wavelength of the emission maxima.

vii) Fluorescence lifetimes were measured using a time correlated single photon counting setup (TCSPC) (FluoTime 300, Picoquant GmbH) with a diode laser (LDH-P-670, Picoquant GmbH, 20 MHz repetition rate, 44 ps pulse width). Fluorescence was detected under the magic angle with a peltier cooled photomultiplier tube (PMT) (PMA-C 192-N-M, Picoquant GmbH) and integrated electronics (PicoHarp 300E, Picoquant GmbH). A monochromator with a spectral width of about 4 nm was used to select the required emission wavelength. The response function of the system, which was measured with a scattering Ludox solution (DuPont), had a full width at half-maximum (FWHM) of about 300 ps. The ratio of stop to start pulses was kept low (~0.05) to ensure good statistics. All fluorescence decay curves were measured at the wavelength of emission maxima. The data were analysed with the FluoFit software (Picoquant®). The support plane approach was used to estimate the errors of the decay times [178]. The layout of the TCSPC is shown in Figure 2.1.

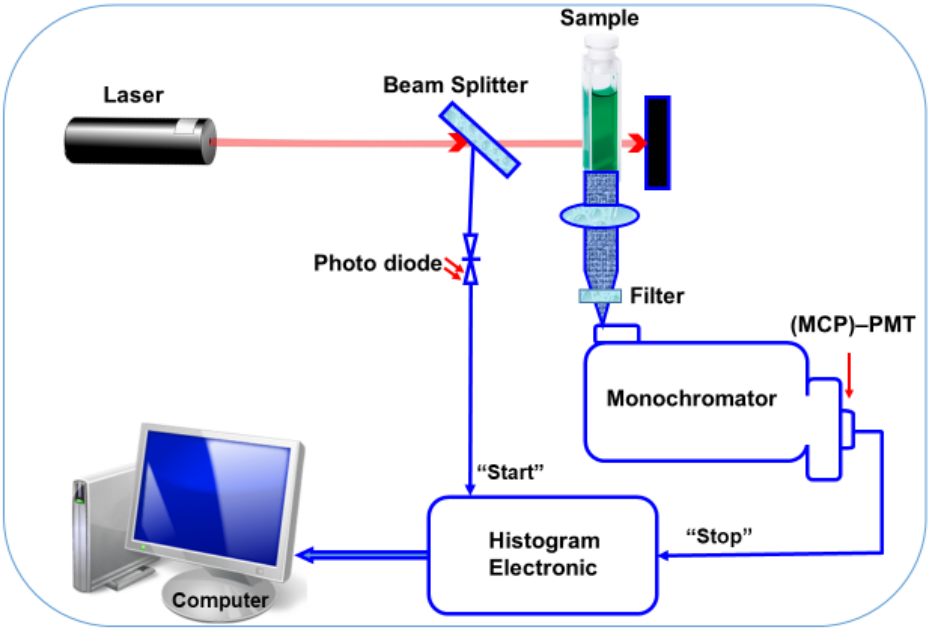

Figure 2.1: Schematic representation of time correlated single photon counting (TCSPC) set–up. (MCP)–PMT = (Multichannel plate detector) Monochromator Photomultiplier Tube

viii) A laser flash photolysis system was used to determine the triplet quantum yields. The excitation pulses were produced using a tunable laser system consisting of an Nd:YAG laser (355 nm, 135 mJ/4–6 ns) pumping an optical parametric oscillator (OPO, 30 mJ/3–5 ns) with a wavelength range of 420–2300 nm (NT-342B, Ekspla, **Figure 2.2**). The signal from a PMT detector was recorded on an oscilloscope. A new system consisting a LP980 spectrometer with a PMT-LP detector, Tektronix digital storage oscilloscope and an ICCD camera (Andor DH320T-25F03) was also used, **Figure 2.3**.

The absorbance of the sample solution and the standard were ~1.5 at the Q–band. The solution was introduced into a 1 cm path length quartz cell and deaerated using argon for 10 min.

Thereafter the solution was sealed and illuminated using an appropriate excitation wavelength source (the crossover wavelength of the sample and the standard is utilized as the laser excitation source wavelength). The maximum triplet absorption detection wavelength was determined from the transient curve. The triplet lifetimes were determined by exponential fitting of the kinetic curves using OriginPro® 8 software.

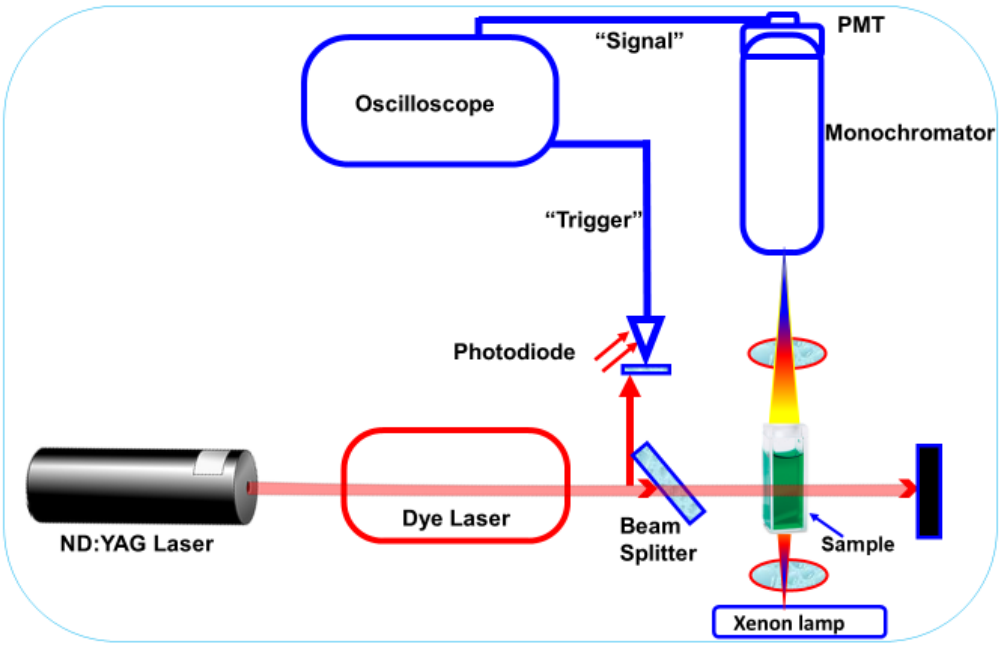

Figure 2.2: Schematic diagram for a laser flash photolysis set–up (old system).

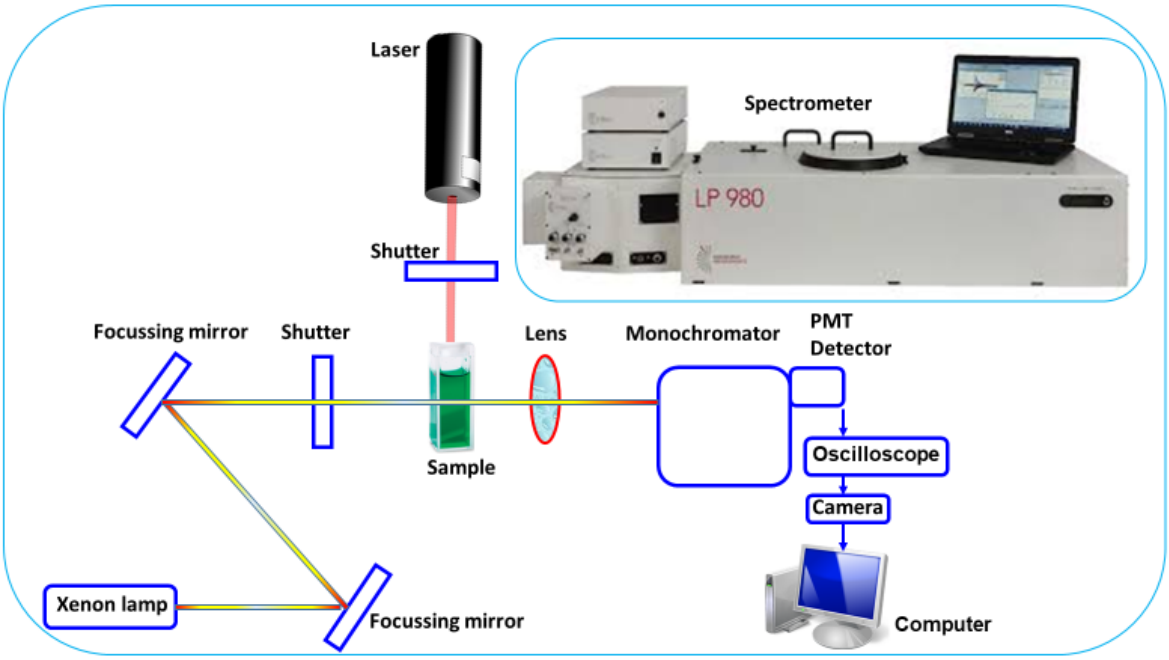

Figure 2.3: Schematic diagram for a LP980 laser flash photolysis set–up (new system; insert shows the LP980 laser flash photolysis spectrometer).

ix) Irradiation for singlet oxygen quantum yield was performed using a general electric quartz lamp (300 W) as irradiation source. A 600 nm cut-off glass filter (Schott) for ultra violet radiation and a water filter for infrared radiation were used. An interference filter, 670 nm with a band of 40 nm was additionally used before the sample chamber. Light intensity was measured with a POWER MAX 5100 (Molelectron detector incorporated) power meter. Solutions of photosensitizer containing DPBF in DMSO or ADMA in aqueous media, were prepared in the dark and irradiated in the Q-band region. DPBF and ADMA degradation at 417 nm and 380 respectively, was monitored during irradiation to quantify the singlet oxygen quantum yield with reference to a standard. The layout of the photochemical set–up is shown in **Figure 2.4**.

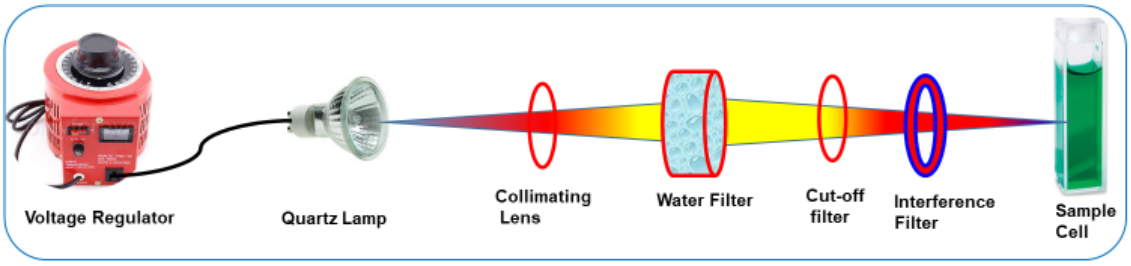

Figure 2.4: Schematic illustration of photochemical set–up

x) X-ray powder diffraction (XRD) patterns were recorded using a Cu kα radiation (1.5405˚A, nickel filter), on a Bruker D8 Discover equipped with a proportional counter. Scanning was at 10 min^{-1} with a filter time-constant of 2.5 s per step and a slit width of 6.0 nm. The data were obtained in the range from 2θ = 5˚to 100˚. A zero background silicon wafer slide was used for sample placement. The data analysis was carried out using Eva (evaluation curve fitting) software. Subtraction of spline fitted to the curved background was used for baseline correction of each diffraction pattern and the full-width at half maximum value was obtained from the fitted curve.

xi) Transmission electron microscope (TEM) images were obtained using a ZEISS LIBRA model 120 operated at 90 kV and iTEM software was used for TEM micrographs processing.

xii) Dynamic light scattering (DLS) experiments were done on a Malvern Zetasizer nanoseries, Nano-ZS90.

xiii) The X-ray photoelectron spectroscopy (XPS) data were acquired using a Kratos Axis Ultra DLD spectrometer, with an Al

(monochromatic) anode, equipped with charge neutralizer and the operating pressure was kept below 5 ×10-9 torr. The resolution was 10 eV pass energy in the slot mode. For the XPS wide scan, the following parameters were used: emission current was kept at 12.5 mA and the anode (HT) voltage at 15 kV. The resolution was maintained at 160 eV pass energy using a hybrid lens in the slot mode. For the high-resolution scans, the resolution was changed to 40 eV pass energy in the slot mode.

xiv) Illumination for PDT studies of Pcs and conjugates were performed using a Modulight Medical Laser system (ML) 7710-680 channel Turnkey laser system coupled with 2 × 3W channels at 680 nm, cylindrical output channels, aiming beam, integrated calibration module, foot/hand switch pedal, fibre sensors (subminiature version A) connectors and safety interlocks. The iIllumination kit for *in vitro* PDT studies with capacity to hold 127.76 × 85.48 mm 96 well tissue culture plate was used.

xv) The MCF-7 cells were cultured in a humidified atmosphere incubator with ~5% CO_2 and temperature at 37 ˚C (Heal Force).

xvi) The cells were viewed under phase contrast using a Zeiss AxioVert.A1 Fluorescence LED (FL-LED) inverted microscope.

xvii) The cell viability was measured with Synergy 2 multi-mode microplate reader (BioTek).

2.3. Synthesis of phthalonitrile and phthalocyanines

One phthalonitrile and six MPcs are reported here for the first time and their synthetic details are provided in this section. Details for the already known phthalonitriles (4-glycosylated phthalonitrile [80], 4-[4-(benzothiazol-2-yl)phenoxy] phthalonitrile [39], 4-[2-(2-thienyl)ethoxy] phthalonitrile [40]) and MPcs (indium(III) tetra–(3–carboxyphenoxy) phthalocyanine (**1**) [37], zinc(II) tetra-(benzothiazol-2-yl phenoxy) phthalocyanine (**3a**) [38], indium(III) chloride tetra-(benzothiazol-2-yl phenoxy) phthalocyanine (**3b**) [39] and zinc(II) tetra-(thiophine ethoxy) phthalocyanine (**4a**) [40]) are as reported in literature.

2.3.1. Synthesis of 4-[3-(4-phenoxy)propanoic acid] phthalonitrile, Scheme 3.1.

3-(4-Hydroxyphenyl) propionic acid (1.44 g, 8.66 mmol) and 4-nitrophthalonitrile (1.5 g, 8.66 mmol) were dissolved in DMF (20 mL) under nitrogen atmosphere and the mixture was stirred at room temperature for 15 min. Finely ground K_2CO_3 (2.11g,15.31 mmol) was added thereafter, and the reaction mixture was left to stir for a further 36 h at room temperature. The mixture was then added to ice water (150 mL). The resulting precipitate was filtered off, thoroughly washed with water, dried and recrystallized from ethanol to give 4-[3-(4-phenoxy)propanoic acid] phthalonitrile. Yield: 2.24g (89%). IR [cm^{-1}]: 3300 (COOH) 2890-3030 (C–H), 2230 (C≡N), 1668-1583 (C=C), 1437-1387 (C–O), 1322-1275 (C-O), 1228 (Ar-O-Ar). ^{1}H NMR (DMSO–

d$_6$): δ, ppm 7.89 (d, *J* = 7.52 Hz, 1H, Ar–H), 7.56 (d, *J* = 7.35 Hz, 1H, Ar–H), 7.37 – 7.32 (m, 3H, Ar–H), 7.12 (m, 2H, Ar–H), 3.48 (s, 1H, OH), 2.85 (t, *J* = 5.17 Hz, 2H, CH_2), 2.55 (t, J = 6.54 Hz, 2H, CH_2). Anal. Calc. for ($C_{17}H_{12}N_2O_3$): C, 69. 86; H, 4.14; N, 9.58. Found: C, 68.69: H, 3.89; N, 9.87.

2.3.2. Synthesis of zinc(II) tetra–[3–(4–phenoxy) propanoic acid] phthalocyanine (2), Scheme 3.2.

A mixture of 4-[3-(4-phenoxy)propanoic acid] phthalonitrile (0.25 g, 0.86 mmol), dry 1–pentanol (3 mL), zinc(II) acetate dihydrate (0.25 g, 1.1 mmol) and DBU (0.3 mL) was transferred into a round bottom flask. The reaction mixture was refluxed at 180 °C for 6 h with constant stirring in the presence of nitrogen. After 6 h, the product was cooled to room temperature, washed successively under centrifugation with methanol. The product, zinc(II) tetra–[3–(4–phenoxy) propanoic acid] phthalocyanine (**2**) was dried under vacuum and purified by column chromatography (silica gel, THF-methanol, 9:1). Yield: 0.46g (43%). IR (cm^{-1}): 3420 (COOH), 2954 (C–H), 1603-1554 (C=C), 1431-1401 (C–O), 1225 (Ar-O-Ar). UV/Vis (DMSO), λ_{max} (nm) (log ε): 680 (4.80), 613 (4.08), 367 (4.50). ^{1}H NMR (600 MHz, DMSO-*d*$_6$) δ 8.89 (s, 3H, Ar-H), 8.57 – 8.25 (s, 3H, Ar-H), 7.78 – 7.57 (m, 3H, Ar-H), 7.58 – 7.28 (m, 17H, Ar-H), 7.19 – 7.05 (m, 2H, Ar-H), 4.02 – 3.50 (s, 4H, H from COOH), 3.07 – 2.85 (m, 8H, CH_2), 2.98 – 2.67 (m, 8H, CH_2). Anal. Calc. for ($C_{68}H_{48}N_8O_{12}Zn$): C, 66.16; H, 3.92; N, 9.08. Found: C, 65.21: H, 3.56; N, 8.09. MS (MALDI-TOF) *m/z*: Calcd: 1234.54; Found: 1234.23 $[M]^+$.

2.3.3. Synthesis of indium(III) chloride tetra-(thiophine ethoxy) phthalocyanine (4b), Scheme 3.3.

Indium(III) chloride tetra-(thiophine ethoxy) phthalocyanine was synthesised in two steps; the first step was the synthesis of the metal-free phthalocyanine (H_2Pc) derivative and the second step involves the metalation of the H_2Pc. The synthesis of the H_2Pc is as follows: 4-[2-(2-thienyl) ethoxy] phthalonitrile (0.58 g, 2.28 mmol) was dissolved in dry 1-pentanol (4 mL), in the presence of DBU (0.3 mL, mmol). The reaction mixture was refluxed at ~140 °C for 6 h with constant stirring under nitrogen atmosphere. On cooling the product to room temperature, methanol was added to the crude product and centrifuged. The washing with methanol was repeated successively until a pure metal free compound was obtained (H_2Pc).

Yield: 0.45 g (77%). IR [ν_{max}/cm^{-1}]: 3073 (Ar-H), 2923 (C-H stretch), 1654, 1600 (C=C), 1513, 1352, 1226 (Ar-O-Ar). UV/Vis (DMSO), λ_{max} nm: 706, 673, 645, 616, 392, 343. ^{1}H NMR (600 MHz, DMSO-d_6) δ 8.95 (d, J = 8.12 Hz, 3H, Ar-H), 8.54 (d, J = 6.62 Hz, 3H, Ar-H), 7.61 – 7.04 (m, 18H, Ar-H), 4.72 (t, J = 4.88 Hz, 8H, CH_2), 4.32 (s, 2H, NH), 3.59 (t, J = 5.67 Hz 8H, CH_2). Anal. Calc. for ($C_{56}H_{42}N_8O_4S_4$): C, 65.99; H, 4.15; N, 10.99; S, 12.58. Found: C, 66.54: H, 3.98; N, 10.78; S, 13.03. MS (MALDI-TOF) *m/z*: Calcd: 1019.24; Found: 1019.30 $[M]^+$.

The conversion of the H_2Pc to an MPc was achieved by mixing the H_2Pc (0.20 g, 1.96 mmol) with indium chloride (0.20 g, 0.90 mmol) in 5 mL 1-chloronaphthalene) and heating at ~ 100 °C for 5 h. Upon cooling the product to room temperature, methanol was added, and the resulting precipitate

centrifuged, and washed several times with methanol. The product indium(III) chloride tetra-(thiophine ethoxy) phthalocyanine (**4b**) was dried under vacuum and purified by column chromatography (silica gel, THF-methanol, 9:1).

Indium(III) chloride tetra-(thiophine ethoxy) phthalocyanine **(4b)**: Yield: 0.15g (75%). IR [ν_{max}/cm^{-1}]: 3069 (Ar-H), 2921 (C-H stretch), 1599 (C=C), 1515, 1348, 1228 (Ar-O-Ar). UV/Vis (DMSO), λ_{max} nm (log ε): 696 (4.89), 627 (4.43), 332 (4.55). ^{1}H NMR (600 MHz, DMSO-d_6) δ 8.99 (d, J = 7.83 Hz, 3H, Ar-H), 8.54 (d, J = 6.69 Hz, 3H, Ar-H) , 7.67 – 7.08 (m, 18H, Ar-H), 4.75 (t, J = 5.42 Hz, 8H, CH_2), 3.52 (t, J = 5.99 Hz 8H, CH_2). Anal. Calc. for ($C_{56}H_{40}ClInN_8O_4S_4$): C, 57.61; H, 3.45; N, 9.60; S, 10.99. Found: C, 57.94: H, 3.63; N, 9.51; S, 10.69. MS (MALDI-TOF) *m/z*: Calcd: 1167.50; Found: 1167.26 $[M]^+$.

2.3.4. Zinc(II) mono–[3–(4–phenoxy) propanoic acid] phthalocyanine (5), Scheme 3.2.

A mixture of 4-[3-(4-phenoxy)-propanoic acid] phthalonitrile (0.20 g, 0.68 mmol), 1,2-dicyanobenzene (0.44 g, 3.42 mmol), zinc(II) acetate dihydrate (0.25 g, 1.1 mmol) and DBU (0.3 mL), dissolved in dry 1-pentanol (3 mL) was refluxed at 180 °C with constant stirring, in the presence of nitrogen for 6 h. The product was cooled and washed with methanol several times. Column chromatography was done over silica with THF: methanol (9:1) as an eluent. Several fractions were collected until zinc(II) mono-[3-(4-phenoxy)propanoic acid] phthalocyanine (**5**) was obtained.

Yield: 0.67g. IR [υ_{max}/cm^{-1}]: 3204-3020 (COOH), 2912 (C-H stretch), 1701 (-C=O), 1596 (C=C), 1471-1398 (C–OH), 1223 (Ar-O-Ar). UV/Vis (DMSO), λ_{max} nm (log ε): 675 (4.90), 608 (4.46), 356 (4.70). ^{1}H NMR (600 MHz, DMSO-d_6) δ 8.25 – 8.03 (d, *J* = 7.87 Hz, 2H, Ar-H), 7.80 – 7.62 (d, J = 7.73 Hz, 2H, Ar-H), 7.5 – 7.25 (m, 9H, Ar-H), 7.24 – 7.04 (m, 6H, Ar-H), 3.55 – 3.27 (s, 1H, H from COOH), 2.89 (t, *J* = 5.47 Hz, 2H, CH_2), 2.73 (t, *J* = 6.21 Hz, 2H, CH_2). Anal. Calc. for ($C_{41}H_{24}N_8O_3Zn$): C, 66.36; H, 3.26; N, 15.10. Found: C, 65.42: H, 2.89; N, 15.02. MS (MALDI-TOF) *m/z*: Calcd: 742.06; Found: 743.19 $[M+H]^+$.

2.3.5. Zinc(II) [tris-(4-(benzothiazol-2-yl)phenoxy)- 3-(4-phenoxy)propanoic acid] phthalocyanine (6), Scheme 3.4.

A mixture of 4-[4-(benzothiazol-2-yl)phenoxy] phthalonitrile 0.64g, 1.73 mmol), 4-[3(4-phenoxy)propanoic acid] phthalonitrile (0.10 g, 0.33 mmol) and zinc(II) acetate dihydrate (0.23 g, 1.1 mmol) was dissolved in dry 1-pentanol (7 mL), after which DBU (0.4 mL) was added. The reaction mixture was refluxed at ~140 °C with constant stirring for 6 h, under nitrogen atmosphere. The crude product was cooled to room temperature and precipitated out of solution using methanol. The precipitate was successively purified with methanol under centrifugation, dried under vacuum and finally purified by column chromatography (silica gel, THF-pentane, 4:1).

Zinc(II) [tris(4-(benzothiazol-2-yl)phenoxy)- 3-(4-phenoxy)propanoic acid] phthalocyanine (**6**): Yield: 0.14 g (19%), IR [υ_{max}/cm^{-1}]: 3049 (OH), 2942 (C-H stretch), 1715 (C=O), 1596 (C=C), 1470, 1327, 1223 (Ar-O-Ar). UV/Vis (DMSO), λ_{max} nm (log ε): 680 (4.89), 612 (4.26), 341 (4.60). ^{1}H NMR (600 MHz,

DMSO-d_6) δ 12.27 (s, 1H, OH), 8.82 (m, 4H, Ar-H), 8.34 (m, 4H, Ar-H), 8.11 – 8.06 (m, 6H, Ar-H), 7.82-7.73 (dd, J = 14.5, 8.7 Hz, 6H, Ar-H), 7.54-7.35 (m, 16H, Ar-H), 6.89 (s, 3H, Ar-H), 6.70 (s, 1H, Ar-H), 4.07 (t, J = 6.1 Hz, 2H, CH_2), 3.02 (t, J = 5.8 Hz, 2H, CH_2). Anal. Calc. for ($C_{80}H_{45}N_{11}O_6S_3Zn$): C, 67.77; H, 3.20; N, 10.87; S, 6.78. Found: C, 67.84: H, 3.42; N, 10.51; S, 7.02. MS (MALDI-TOF) *m/z*: Calcd: 1417.86; Found: 1416.74 $[M-H]^+$.

2.3.6. Zinc(II) [tris-(3-(4-phenoxy)propanoic acid)-4-(bezothiazol-2-yl) phenoxyl] phthalocyanine (7), Scheme 3.4.

A mixture of 4-[4-(benzothiazol-2-yl)phenoxy] phthalonitrile (0.11g, 0.31 mmol), 4-[3-(4-phenoxy)propanoic acid] phthalonitrile (0.46 g, 1.56 mmol) and zinc(II) acetate dihydrate (0.20 g, 0.96 mmol) was dissolved in dry 1-pentanol (4 mL), after which DBU (~0.1 mL) was added. The reaction mixture was refluxed at 160 °C for 6 h, under nitrogen atmosphere. On cooling, methanol was added and the precipitate was collected under centrifugation. The precipitate was successively purified with methanol under centrifugation, dried and further purified by column chromatography using THF and methanol (9:1) as eluent, yielding zinc(II) [tris-(3-(4-phenoxy)propanoic acid)-4-(bezothiazol-2-yl) phenoxyl] phthalocyanine (**7**).

Yield: 0.08g (14.0%). IR [υ_{max}/cm^{-1}]: 3065 (OH), 2921 (C-H stretch), 1719 (C=O), 1596, 1475 (C=C), 1230 (Ar-O-Ar). UV/Vis (DMSO), λ_{max} nm (log ε): 681 (4.85), 614 (4.16), 356 (4.48). ^{1}H NMR (600 MHz, DMSO-d_6) δ 11.32 (s, 3H, OH), 7.81 (d, J = 8.8 Hz, 2H, Ar-H), 7.37−7.09 (m, 30H, Ar-H), 2.89−2.85 (dd, J = 6.9, 1.5 Hz, 6H, CH_2), 2.68−2.65 (t, J = 5.7 Hz, 6H, CH_2), Anal. Calc. for

($C_{72}H_{47}N_9O_{10}SZn$): C, 66.74; H, 3.66; N, 9.73; S, 2.47. Found: C, 66.29: H, 3.89; N, 9.41; S, 3.00. MS (MALDI-TOF) *m/z*: Calcd: 1295.64; Found: 1295.40 $[M]^+$.

2.3.7. Zinc(II) [(tris- (2,2,7,7-tetramethyltetrahydro-3aH-bis([1,3] dioxolo)[4,5-b:4',5'-d]pyran-5-yl)methoxy)-2-(4-benzothiazol-2-yl)phenoxy] phthalocyanine (8), Scheme 3.5.

A mixture of 4-glycosylated phthalonitrile (0.55 g, 1.42 mmol), 4-[4-(benzo thiazol-2-yl)phenoxy] phthalonitrile (0.1 g, 0.28 mmol), zinc(II) acetate dihydrate (0.25 g, 1.1 mmol) and DBU (0.3 mL), was dissolved in dry 1-pentanol (3 mL). The reaction mixture was refluxed at 180 °C with constant stirring, in the presence of nitrogen for 6 h. The product was cooled to room temperature and successively precipitated out of solution using methanol. Zinc(II) [tris- (2,2,7,7-tetramethyltetrahydro-3aH-bis([1,3]dioxolo)[4,5-b:4',5'-d]pyran-5-yl)methoxy)-2-(4-(benzothiazol-2-yl)phenoxy] phthalocyanine (**8**) was obtained using silica packed column chromatography with THF:methanol (9:1) as an eluent.

Yield: 0.11 g (16.9%). IR [υ_{max}/cm^{-1}]: 3196, 2921 (C-H stretch), 1710, 1605 (C=C), 1474-1371 (C=C), 1217 (Ar-O-Ar). UV/Vis (DMSO), λ_{max} nm (log ε): 682 (5.55), 612 (4.52), 320 (4.78). ^{1}H NMR (400 MHz, $CDCl_3$) δ 8.13 (d, *J* = 8.7 Hz, 2H), 8.02 (d, *J* = 8.1 Hz, 1H), 7.87 (d, *J* = 7.8 Hz, 1H), 7.71 (d, *J* = 8.7 Hz, 1H), 7.64 (d, *J* = 8.8 Hz, 2H), 7.52 – 7.41 (m, 1H), 7.39 – 7.29 (m, 3H), 7.25 (dd, *J* = 8.9, 2.5 Hz, 3H), 7.16 (dd, *J* = 10.8, 5.7 Hz, 6H), 5.50 (d, *J* = 5.0 Hz, 6H),

4.61 (dd, J = 7.9, 2.5 Hz, 6H), 4.33 – 4.09 (m, 9H), 1.44 (m, 24H), 1.29 (s, 12H). Anal. Calc. for ($C_{81}H_{77}N_9O_{19}SZn$): C, 61.65; H, 4.92; N, 7.99; S, 2.03. Found: C, 62.02: H, 5.09; N, 7.02; S, 1.92. MS (MALDI-TOF) *m/z*: Calcd: 1577.97; Found: 1578.44 $[M + H]^+$.

2.4. Synthesis of nanoparticles (NPs) and composites.

The syntheses of GSH capped AgNSs-GSH [179], AuNSs-GSH [180], as well as the CTAB capped AuNSs-CTAB, AuNRs-CTAB [181] and CTAC capped AuNTs-CTAC [182] have been reported before. CTAC was chosen as a capping agent over CTAB for the synthesis of nanotriangles since it results in a high yield [182].

2.4.1. Synthesis glutathione (GSH) functionalized Ag_xAu_y alloy and AuNTs nanoparticles.

Firstly oleic acid/oleylamine (OA/OLA) capped Ag_xAu_y alloys with different mole ratios (3:1 and 1:3) were synthesised as reported in literature with modifications [122]. For the formation of Ag_3Au_1 (this is a Ag rich alloy), a mixture of silver acetate (0.38 g, 2.26 mmol) and gold(III) chloride trihydrate (0.251 g, 0.74 mmol) was employed. For the formation of Ag_1Au_3 (this is an Au rich alloy), a mixture of silver acetate (0.062 g, 0.37 mmol) and gold(III) chloride trihydrate (0.38 g, 1.11 mmol) was employed. The mixtures above were separately placed into 250 mL round bottom flasks containing diphenyl ether (DPE, 30 g, 176.3 mmol), oleylamine (OLA, 10 mL) and oleic acid (OA, 5

mL). The reaction mixtures were refluxed at 160 °C and maintained under argon atmosphere for 5 h, followed by cooling to room temperature. The products were successively purified with ethanol and dried in enclosed fume hood and are represented as Ag_3Au_1NSs-OA/OLA and Ag_1Au_3NSs-OA/OLA

The surface of Ag_3Au_1NSs-OA/OLA, Ag_1Au_3NSs-OA/OLA and AuNTs-CTAC were separately modified with glutathione (GSH) as follows: Ag_3Au_1NSs-OA/OLA, Ag_1Au_3NSs-OA/OLA and AuNTs-CTAC (0.40 g) were each transferred into separate round bottom flasks containing cyclohexane (3 mL). A solution containing methanol (20 mL), GSH (0.25 g, 0.81 mmol) and KOH (0.50 g, 8.93 mmol) was added to the NPs mixture. The mixtures were stirred for 2 h at room temperature. Afterwards, the formed GSH capped NPs were precipitated out of solution using ethanol and purified with methanol. The obtained solid precipitates were air dried in an enclosed fume hood. The nanoparticles are represented as Ag_3Au_1NSs-GSH, Ag_1Au_3NSs-GSH and AuNTs-GSH.

2.4.2. Doping of Ag_3Au_1NSs-OA/OLA into SiNSs to form Ag_3Au_1SiNSs-APTES, Scheme 3.6B.

The doping of the Ag_3Au_1NSs-OA/OLA into SiNSs was done using a method adopted from literature [183] as follows: Triton X–100 (1.80 mL), 1–hexanol (1.80 mL) and cyclohexane (7.5 mL) were introduced into a 50 mL round bottom flask and stirred for 20 min. Afterwards 0.20 g of Ag_3Au_1NSs-OA/OLA in cyclohexane was added and the mixture was further stirred for 10 min. TEOS (0.15 mL) was then added, followed by dropwise addition of H_2O (0.4

mL) and 25% NH_3OH solution (0.06 mL) for 1 h. The mixture was kept stirring for 24 h to allow for nucleation and particle growth of the SiNSs around Ag_3Au_1NSs to form Ag_3Au_1SiNSs. The obtained product was isolated out of solution using ethanol, purified with ethanol and air dried in an enclosed fume hood.

The functionalisation of the Ag_3Au_1SiNSs using APTES was done as reported in the literature [184] with modifications. Briefly, 0.09 g of Ag_3Au_1SiNSs was weighed into a 50 mL round bottom flask, then, APTES (0.2 mL, 0.85 mmol) and toluene (2 mL) were added. The mixture was refluxed at 110 °C for 5 h. The obtained product was purified with ethanol and acetonitrile. Finally, the solid was air dried in an enclosed fume hood. The product is represented as Ag_3Au_1SiNSs-APTES.

2.4.3. Synthesis of gold-speckled silica (GSS) nanoparticles, Scheme 3.7.

Gold-speckled silica (GSS) nanoparticles were synthesized using 3-aminopropyl)-triethoxysilane (APTES) functionalised silica nanoparticles (SiNSs-APTES) [183,184] and gold nanoparticles seeds [185] which were synthesized as reported in the literatures with slight modifications. For the attachment of gold nanoparticles seeds onto functionalized silica cores, 40 mg of APTES functionalized silica nanoparticles were dispersed in THF and placed in a 150 ml flask with an excess of gold nanoparticles seeds. The mixture was stirred gently for 5 min and then allowed to stand for 2h. The mixture was

then centrifuged, washed with water and the gold decorated SiNSs (GSS) were dried.

2.4.4. Synthesis of a gold chitosan (AuCT) composite, Scheme 3.8.

A gold-chitosan (AuCT) composite [186,187] was prepared as reported in the literature with slight modifications; briefly CT (100 mg) was dissolved in 1% (v/v) aq. solution of acetic acid (40 mL) and stirred for 1 h at room temperature until a homogeneous viscous solution was obtained. The aqueous CT solution (20 mL) was then added to an excess solution of gold nanoparticles seeds synthesized as reported in literature [185], followed by stirring at room temperature for 24 h. The obtained product (AuCT) was successively washed with acetone and centrifuged until a clear supernatant was observed.

2.5. Conjugation of MPcs to NPs and composites.

2.5.1. Covalent (amide bond) linkage of complexes to GSH or APTES functionalised NPs, Scheme 3.9.

The MPc–NPs conjugates were synthesized as follows: complex **1** (0.02 g, 0.017 mmol), complex **2** (0.02 g, 0.017 mmol), complex **5** (0.013 g, 0.017 mmol), complex **6** (0.023 g, 0.016 mmol) and complex **7** (0.022 g, 0.017 mmol) were dissolved in 2 mL of dry DMF. The coupling agents, DCC (0.01 g, 0.049 mmol) and DMAP (0.005 g, 0.042 mmol) were added to activate the carboxylic acid group of the MPc complexes to allow for covalent linkage to NPs via amide bond formation. The reaction was stirred for 48 h at room temperature after which 0.05 g of NPs (either Ag_1Au_3NSs-GSH, Ag_3Au_1NSs-GSH, Ag_3Au_1SiNSs-

APTES, AuNSs-GSH, AgNSs-GSH or AuNTs-GSH) was added and the reaction mixture was stirred for further 48 h at room temperature (**Scheme 3.9**, complex **1** as a representative). The conjugates formed were centrifuged, successively purified with ethanol and allowed to dry in the fume hood. The conjugates are represented as **1**-Ag_1Au_3NSs-GSH, **1**-Ag_3Au_1NSs-GSH, **1**-Ag_3Au_1SiNSs-APTES, **2**-AuNSs–GSH, **2**-AgNSs–GSH, **2**-AuNTs-GSH, **2**-Ag_3Au_1NSs–GSH, **5**-AuNSs–GSH, **5**-AgNSs–GSH, **5**-AuNTs-GSH, **5**-Ag_3Au_1NSs–GSH, **6**-AuNTs–GSH, **6**-AuNSs–GSH, **7**-AuNTs–GSH and **7**-AuNSs–GSH)

2.5.2. Linkage (Au-S/Au-N) of complexes 3a, 3b, 4a, 4b, 6, 7 and 8 to AuNPs, Scheme 3.10.

The presence of gold in AuNPs, is expected to foster the formation of sulphur-gold (Au-S) or nitrogen-gold (Au-N) bonds between NPs and complexes, through self-assembly since the thiophine portion of complexes **4a** and **4b** contain sulphur while the benzothiazole in complexes **3a**, **3b**, **6, 7** and **8** contains both sulphur and nitrogen groups.

The MPcs were linked to AuNSs-CTAB, AuNTs-CTAC and AuNRs-CTAB (for complex **8** only) as follows: complex **3a** (0.02 g, 0.014 mmol), complex **3b** (0.02 g, 0.013 mmol), complex **4a** (0.021 g, 0.019 mmol), complex **4b** (0.02 g, 0.017 mmol), complex **6** (0.02g, 0.014 mmol), complex **7** (0.02 g, 0.015 mmol) and complex **8** (0.02g, 0.0127mmol) were separately dissolved in dry DMF (2 mL) and 0.5 mg of NPs (AuNSs-CTAB or AuNTs-CTAC or AuNRs-CTAB) in 3 mL

water were added and the reaction mixture was stirred for 24 h at room temperature (**Scheme 3.10**, shows the linkage of complex **8** to AuNSs-CTAB as a representative).

The conjugates were centrifuged, successively washed with ethanol and allowed to dry in the fume hood. The conjugates are represented as **3a**-AuNSs-CTAB, **3a**-AuNTs-CTAC, **3b**-AuNSs-CTAB, **3b**-AuNTs-CTAC, **4a**-AuNSs-CTAB, **4a**-AuNTs-CTAC, **4b**-AuNSs-CTAB, **4b**-AuNTs-CTAC, **6**-AuNSs-CTAB, **6**-AuNTs-CTAC, **7**-AuNTs-CTAC, **8**–AuNSs-CTAB and **8**–AuNRs-CTAB

2.5.3. Linkage of complexes 3a, 3b, 4a and 4b to gold-speckled silica NPs, Scheme 3.7.

The MPc–GSS conjugates were synthesized as follows: complex **3a** (0.02 g, 0.014 mmol), complex **3b** (0.02 g, 0.013 mmol), complex **4a** (0.02 g, 0.018 mmol) or complex **4b** (0.02 g, 0.017 mmol) were separately dissolved in dry DMF (2 mL). GSS (0.05 g in 5 mL DMF) were added and the reaction mixture was stirred for 24 h at room temperature (**Scheme 3.7**, shows the linkage of complex **4b** to GSS as a representative). The conjugates were centrifuged, successively purified with ethanol and allowed to dry in the fume hood. The conjugates are represented as **3a**-GSS, **3b**-GSS, **4a**-GSS and **4b**-GSS.

2.5.4. Linkage of complex 6 to CT and AuCT, Scheme 3.8.

The CT composites were prepared as beads using the reported coacervation precipitation method reported previously [120] with slight modifications. Briefly complex **6** (0.02g, 0.014 mmol) in DMF (5 mL) was mixed with CT (0.024 g in 10 mL of 1% (v/v) aqueous acetic acid solution) or AuCT (0.047 g in 10 mL of 1% (v/v) aqueous acetic acid solution). The mixtures were stirred for 48 h at room temperature. The conjugates were successively purified with ethanol under centrifugation and allowed to dry in the fume hood. The conjugates are represented as **6**-CT and **6**–AuCT.

2.6 *In vitro* dark cytotoxicity and photodynamic therapy studies.

The *in vitro* dark cytotoxicity and PDT studies of complex **3b**, **3b**-GSS and GSS; complex **6**, **6**-AuCT and AuCT; complex **8**, **8**-AuNSs-CTAB, **8**-AuNRs-CTAB, AuNSs-CTAB and AuNRs-CTAB were tested against epithelial breast cancer cell lines (MCF–7). Complexes and some conjugates are not soluble in aqueous media, hence they were first dissolved in DMSO and made up to the desired volume with supplemented DMEM.

2.6.1. Culturing of MCF–7 cells.

The MCF–7 cells were cultured using Dulbecco's modified Eagle's medium (DMEM) supplemented with 10% (v/v) heat inactivated fetal calf serum (FCS) and 100 unit/mL penicillin–100 µg/mL streptomycin–amphotericin B. The cells were cultured in T75 flasks, incubated at 37 ˚C and 5% CO_2 in a

humidified atmosphere until a cell confluence of 80 % was achieved. The cells were rinsed with Dulbecco's modified phosphate buffer saline (DPBS) before routine trypsinisation. The viable trypsinised cells were counted with the aid of a trypan blue dye exclusion assay (0.40% trypan blue solution) using a hemocytometer. The cells were seeded at a cell density of 10,000 cells/well in supplemented DMEM containing phenol red in 96–well plates. They were further incubated under similar conditions for 24 h to allow cell attachment to the wells. The attached cells were rinsed with 100 µL DPBS once, followed by administration of 100 µL supplemented DMEM containing gradient doses of the respective drugs (complexes, conjugates and NPs). The stock drug concentrations were prepared in DMSO and made up to the desired volume with supplemented DMEM. Plates were re-incubated again at 37°C and 5% CO_2 in the dark for 24 h. The effect of DMSO on the cells was investigated by the incubation of cells with 1.6% (v/v) DMSO in supplemented DMEM which represents the highest percentage of DMSO in the drug gradient solutions. Control cells were given supplemented DMEM with phenol red without the drug. After 24 h, the cells were rinsed with 100 µL DPBS once and were ready for *in vitro* dark cytotoxicity

2.6.2. In vitro dark cytotoxicity and PDT activity.

For *in vitro* dark toxicity supplemented DMEM with phenol red was added and the plates were re-incubated for 24 h.

For PDT studies, supplemented phenol red free DMEM was added and the plates were subsequently illuminated with fixed light dosimetry of 170 J/cm^2

using a Modulight ML7200 series illumination set–up as a light source. After illumination, the supplemented phenol red free DMEM was replaced with supplemented DMEM with phenol red and the plates were re-incubated for 24 h.

For both *in vitro* dark cytotoxicity and PDT activity, each experiment was performed in triplicate replicate and surviving cells were quantified after re–incubation using WST-1 viability assay

2.6.3. Cell viability determination

The WST–1 assay was used to assess the toxicity and cell proliferation in the monolayer of the cells treated with the drugs and the control, respectively. This was performed as specified in the manufacturer's instruction and a Synergy 2 multi–mode microplate reader (BioTek) set at a wavelength of 450 nm was used to quantify the stained viable cells. The percent cell viability was determined using equation 2.1:

$$\% \text{ cell viability} = \frac{\text{Absorbance sample}}{\text{Absorbance control}} \times 100 \qquad (2.1)$$

where the absorbance of sample is for cells containing drugs while absorbance of control is for control cells containing only supplemented DMEM with phenol red.

2.6.4 Statistical analysis

The data obtained from the experiments was statistically analysed. Each sample was run 3 times and each experiment was repeated three times. One–way analysis of variance (ANOVA) for the in vitro dark cytotoxicity and PDT data of the drugs against MCF-7 cell was evaluated. A p–value < 0.05 was considered to be statistically significant.

RESULTS AND DISCUSSIONS

3. Synthesis and characterization

4. Photophysical and photochemical properties

5. *In vitro* dark cytotoxicity and photodynamic therapy activity

Publications

1. Edith Dube, David O. Oluwole, Tebello Nyokong Photophysicochemical behaviour of anionic indium phthalocyanine when grafted onto Ag_xAu_y and porous silica nanoparticles, **J. Luminescence**, **190 (2017) 353-363**.
2. Edith Dube, Nwaji Njemuwa, David O. Oluwole, John Mack, Tebello Nyokong, Investigation of photophysicochemical properties of zinc phthalocyanines conjugated to metallic nanoparticles, **J. Photochem. Photobiol A. 349 (2017) 148-161** *(Invited Feature article).*
3. Edith Dube, David O. Oluwole, Tebello Nyokong, Improved photophysical and photochemical properties of thiophene ethoxy substituted metallophthalocyanines on immobilization with gold–speckled silica nanoparticles, **Photochemistry Photobiology 94 (2018) 521-531.**
4. Edith Dube, David O. Oluwole, Nwaji Njemuwa, Tebello Nyokong**,** Glycosylated zinc phthalocyanine-gold nanoparticle conjugates for photodynamic therapy: Effect of nanoparticle shape, **Spectrochim Acta, 203 (2018) 85-95**.
5. Edith Dube, David O. Oluwole, E. Prinsloo, Tebello Nyokong,Gold–chitosan composite with low symmetry zinc phthalocyanine for enhanced singlet oxygen generation and improved photodynamic therapy activity, **New J. Chem. 42 (2018) 10214-10225.**
6. Edith Dube, Nwaji Njemuwa, John Mack, Tebello Nyokong, Photophysicochemical behavior of symmetric and asymmetric zinc

phthalocyanines, surface assembled onto gold nanotriangles, **New J. Chem, 42 (2018) 14290-14299.**

7. Edith Dube, Tebello Nyokong,. Effect of gold nanoparticles shape and size on the photophysicochemical behaviour of symmetric and asymmetric zinc phthalocyanines, **J. Luminescence, 205 (2019) 532-539.**
8. Edith Dube, David O. Oluwole, Nwaji Njemuwa, Earl Prinsloo, Tebello Nyokong, Photophysicochemical and photodynamic therapy properties of metallophthalocyanines linked to gold speckled silica nanoparticles. In preparation.
9. Edith Dube, Tebello Nyokong, Effect of gold nanoparticle shape on the photophysicochemical properties of sulphur containing metallophthalocyanines. Submitted to Journal of Molecular Structure.

Extra publications

10. D. O. Oluwole, F. A. Sarı, E. Prinsloo, E. Dube, A. C. Yuzer, T. Nyokong, M. Ince, Photophysicochemical properties and photodynamic therapy activity of highly water-soluble Zn(II) Phthalocyanines, **Spectrochim Acta: A**. **203 (2018) 236-243.**
11. D. O. Oluwole, N. Njemuwa, L. C. Nene, L. Mokone, E. Dube, T. Nyokong, Novel nano–dyad of homoleptic sandwich–type phthalocyanines with nitrogen doped graphene quantum dots for nonlinear optics, **New J Chem**. **42 (2018) 10124-10133**

CHAPTER 3

3. Synthesis and characterizaton

This chapter gives details of the synthesis and the characterization of the MPcs, nanoparticles (NPs) and the MPc-NPs conjugates used in this work.

3.1. Metalophthalocyanines (MPcs-complexes).

The syntheses of complexes **1**, **3a**, **3b** and **4a** have been previously reported [37–40] thus their characterisation will not be discussed in this work. The characterization of new complexes **2**, **4b** and **5–8** will be discussed in detail in the following subsections. The synthesis of a new phthalonitrile, 4-[3-(4-phenoxy)-propanoic acid] phthalonitrile which was used for the synthesis of complexes **2**, **5**, **6** and **7** will also be discussed.

3.1.1. 4-[3-(4-phenoxy)-propanoic acid] phthalonitrile.

The formation of 4-[3-(4-phenoxy)propanoic acid] phthalonitrile was via a nucleophilic substitution reaction of the hydroxyl moiety of the 3-(4-hydroxyphenyl) propionic acid and the nitro group of the 4-nitrophthalonitrile, **Scheme 3.1**.

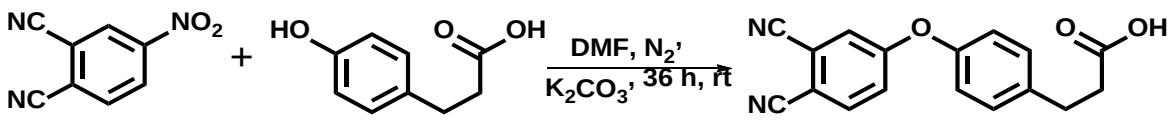

Scheme 3.1: Synthetic route for 4-[3-(4-phenoxy)propanoic acid] phthalonitrile.

The compound was characterised using FT–IR, ^{1}H NMR and elemental analyses. The FT-IR spectrum of the substituted phthalonitrile (**Figure 3.1**) showed the presence of C≡N (2230 cm^{-1}) and Ar-O-Ar (1228 cm^{-1}) which is typical of ether substituted phthalonitrile. The presence of a carboxylic acid OH group (3300 cm^{-1}) and C=O (1688 cm^{-1}) show the successful substitution of 4-nitrophthalonitrile with 3-(4-hydroxyphenyl) propionic acid.

The ^{1}H NMR showed the aromatic protons between 7.89 - 7.12 ppm, the COOH proton was observed at 3.48 ppm and the CH_2 groups of the propanoic acid chain at 2.85 ppm and 2.55 ppm. Peak integration gave the anticipated number of protons, confirming the purity of the phthalonitrile. The elemental analysis agreed with the proposed structure.

3.1.2. Zinc(II) tetra–[3-(4-phenoxy)propanoic acid] phthalocyanine (2) and zinc(II) mono–[3-(4-phenoxy)propanoic acid] phthalocyanine (5).

The synthesis of complex **2** was achieved by cyclocondensation of 4-[3-(4-phenoxy)propanoic acid] phthalonitrile in the presence of a catalytic amount of DBU, Zn salt, and 1-pentanol. Complex **5** was formed by cross–condensation of 1,2-dicyanobenzene and 4-[3-(4-phenoxy)propanoic acid] phthalonitrile in the presence of DBU, Zn salt, and 1-pentanol (**Scheme 3.2**). The disappearance of a dinitrile peak at 2230 cm^{-1} in the FT-IR spectrum of **2** and **5** (**Figure 3.1**, using complex **2** as an example) confirmed the formation of the complexes.

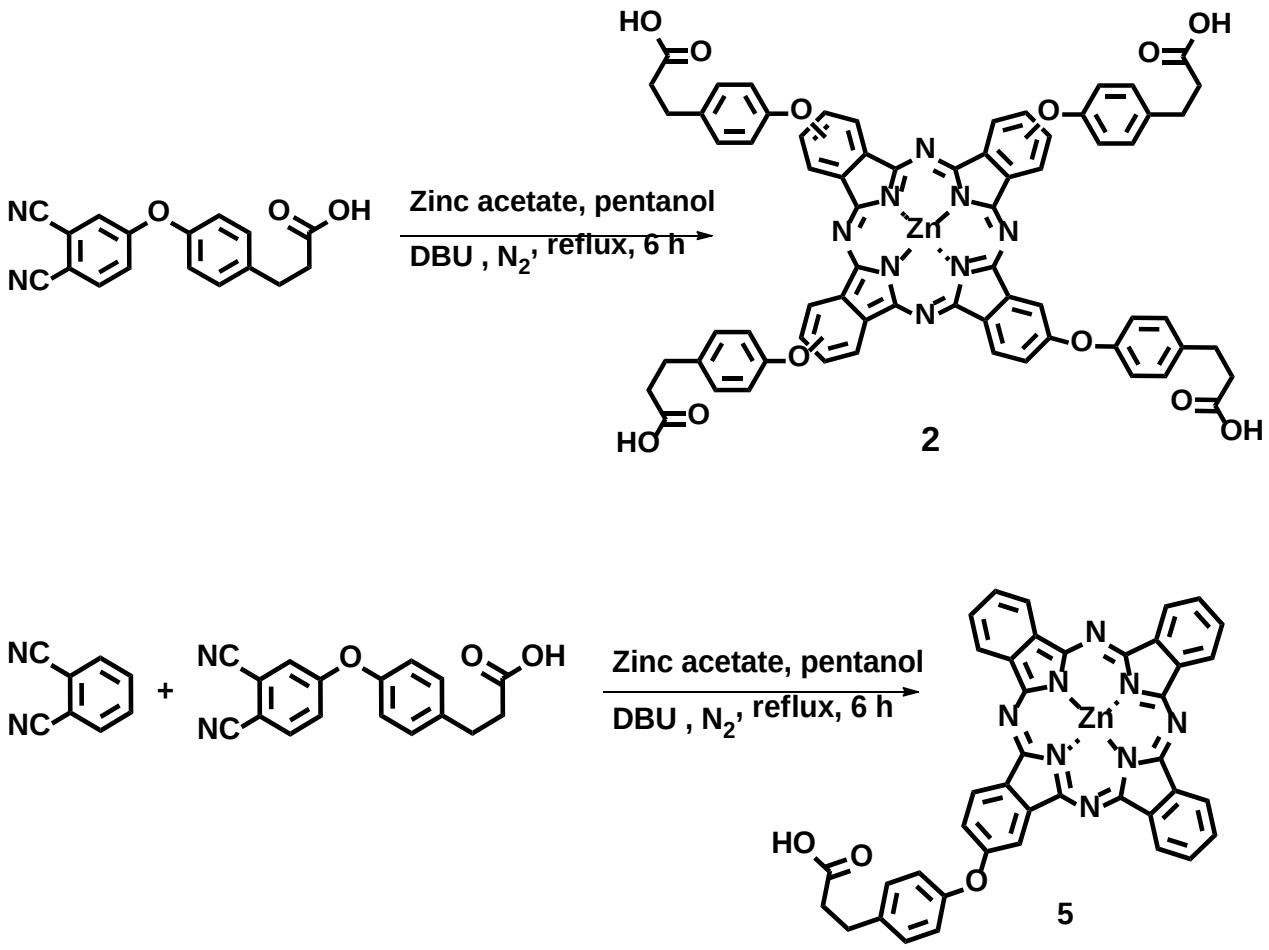

Scheme 3.2: Synthetic routes for complexes **2** and **5**.

The ^{1}H NMR spectra for complexes **2** and **5**, showed aromatic ring proton peaks between 8.89−7.04 ppm, the COOH protons between 4.02 – 3.27 ppm and the CH_2 groups of the propanoic acid chain were observed between 3.07 – 2.67 ppm. Peak integration gave the anticipated number of protons for both complexes, confirming their purity.

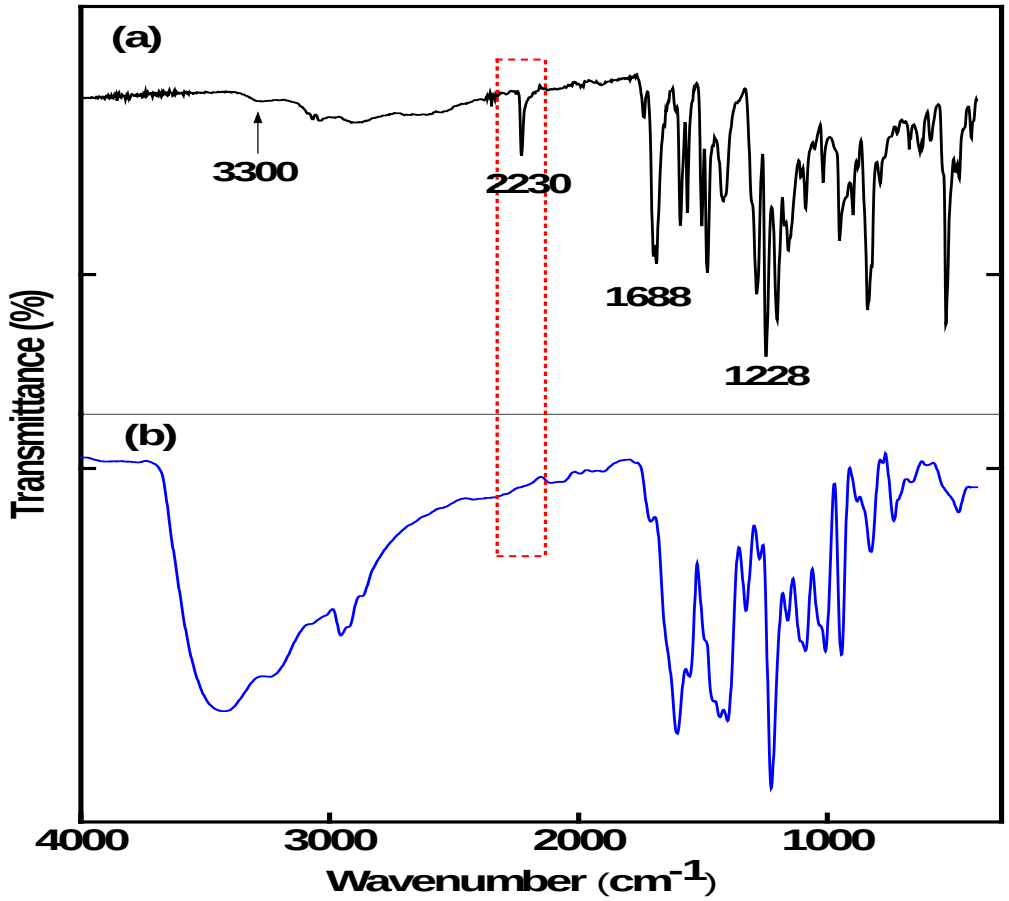

Figure 3.1: FT-IR spectra for 4-[3-(4-phenoxy)propanoic acid] phthalonitrile (a) and complex **2** (b).

The mass spectrum of **2** showed the molecular ion peak at *m/z*: 1234.23 $[M]^+$, while that of **5** was found at *m/z*: 743.19 $[M+H]^+$ and these agreed with the proposed structure in **Schemes 3.2.** The obtained elemental analyses agreed with the calculated inferring the purity of the complexes.

The ground state absorption spectra for complexes **2** and **5** (**Figure 3.2**) showed monomeric behaviour of the complexes as evidenced by a single narrow Q band at 680 nm and 675 nm respectively (**Table 3.1**), as typically observed for metalated phthalocyanines with degenerate D_{4h} symmetry [188].

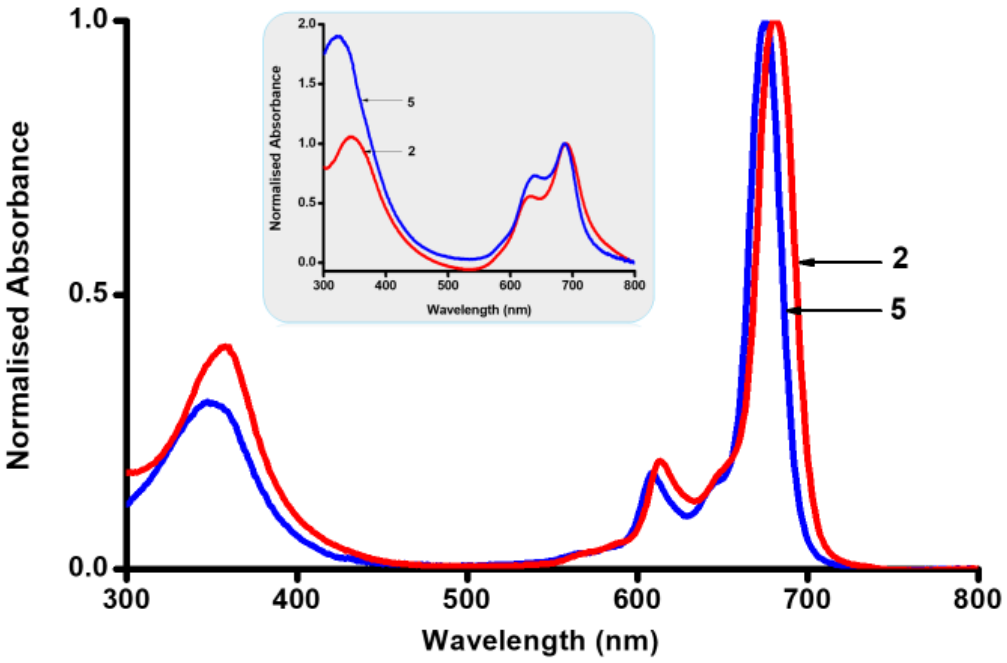

Figure 3.2: The ground state absorption spectra for complexes **2** and **5** in DMSO (insert: absorption spectra in water containing 1.6% DMSO).

The red shift in the Q band of complex **2** compared to **5**, can be attributed to a relative destabilization of the highest occupied molecular orbital (HOMO) due to the electron donating ability of the four phenoxy propionic acid groups in complex **2**, compared to one phenoxy propionic acid group in complex **5**. This in turn decreases the energy gap between the HOMO and lowest unoccupied molecular orbital (LUMO) of complex **2** [189].

In water containing 1.6% DMSO (**Figure 3.2,** insert), the Q-bands are broad due to aggregation, typical of Pcs in aqueous solution due to π–π stacking interaction of the aromatic rings of Pcs [190]. The effect of aggregation is usually reduced by solubilization of the drug in a biocompatible surfactant for therapeutic formulations. Complexes and some conjugates are not soluble in water, hence 1.6% (v/v) DMSO in water was used for cell studies hence the importance of determining the parameters in its presence.

3.1.3. Indium(III) chloride tetra-(thiophine ethoxy) phthalocyanine (4b).

Complex **4b** was synthesised through a cyclocondensation reaction of 4-[2-(2-thienyl)ethoxy] phthalonitrile in the presence of DBU and 1-pentanol to form an H_2Pc. This was followed by metallation of the H_2Pc using an indium salt to form complex **4b**, **Scheme 3.3**.

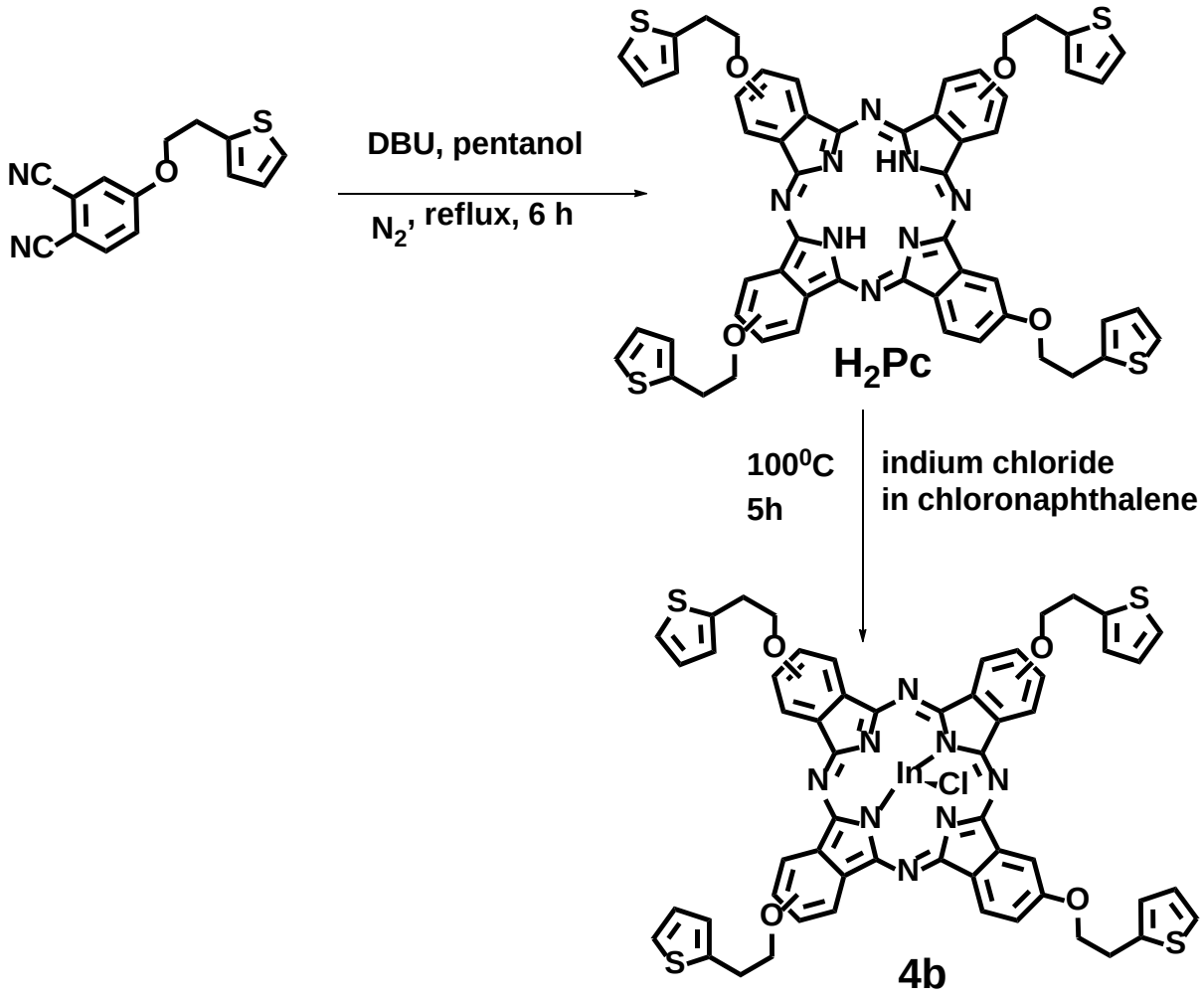

Scheme 3.3:. Synthetic route for complex **4b**.

The disappearance of the C≡N peak of the phthalonitrile at 2228 cm^{-1} (Figure not shown) observed in the FT-IR spectra for complex **4b** confirmed successful formation of a Pc. The ^1H NMR spectrum for the H_2Pc (**Figure 3.3**) displayed

aromatic ring proton peaks between 8.95–8.54 ppm and 7.61 – 7.04 ppm. The protons of the CH_2 of the ethoxy groups were observed at 4.72 ppm and 3.59 ppm. The NH peaks were shown at 4.32 ppm. Upon metallation with indium chloride similar peaks were observed with the disappearance of the NH peaks (**Figure 3.3**) showing successful metallation. Due to the presence of isomers most aromatic signals overlap resulting in the broadening of signals, however peak integration gave the expected total number of protons, confirming the purity of the complex. Mass spectral data (H_2Pc *m/z*: 1019.30 $[M]^+$ and complex **4b** *m/z*: 1167.26 $[M]^+$) and elemental analyses agreed with the proposed structure in **Scheme 3.3**.

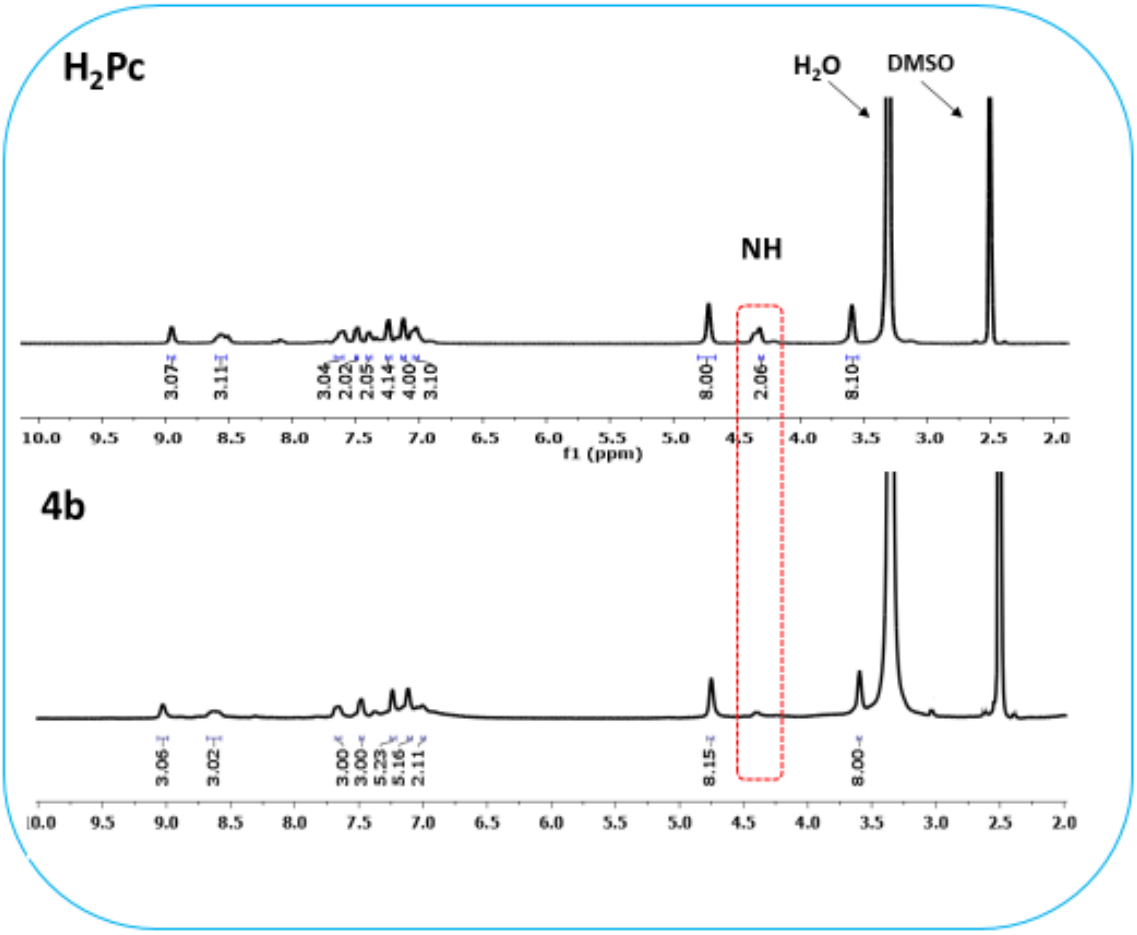

Figure 3.3: Mass spectra for H_2Pc and complexes **4b**.

The absorption spectra for complex **4b** and the already reported Zn(II) counterpart (complex **4a**) [40] in DMSO are overlayed in **Figure 3.4.** These complexes showed monomeric behaviour as evidenced by narrow, single Q bands at 682 and 695 nm, for complexes **4a** and **4b**, respectively (**Table 3.1**). The Q band of complex **4b** is slightly red shifted compared to **4a**. The red shifting is attributed to the non-planar effect of the indium(III) ion, with a relatively bigger atomic radius than the zinc(II) as the central metal ion in the Pc cavity, and this relatively destabilizes the HOMO as explained before [189,191,192]. In water (containing 1.6% DMSO), there is broadening of Q bands (**Figure 3.4,** insert) but not split as observed above.

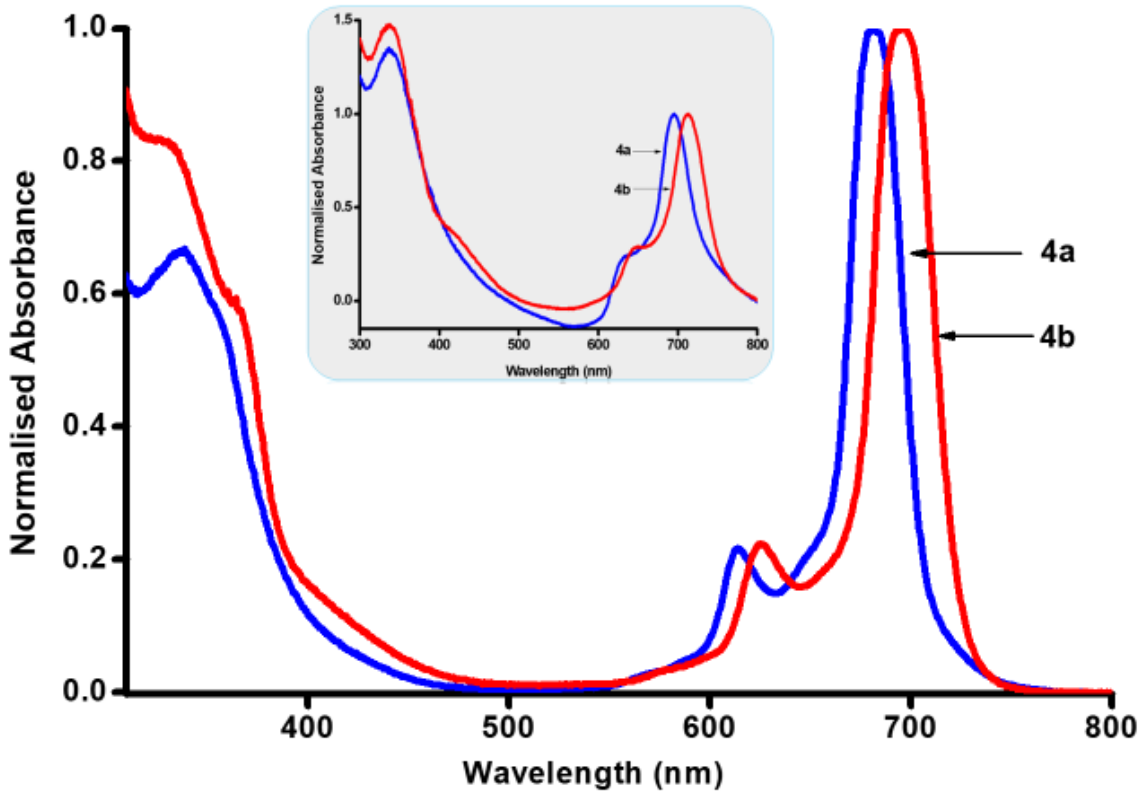

Figure 3.4: The ground state absorption spectra for complexes 4a and 4b in DMSO (and water containing 1.6% DMSO, insert).

3.1.4. Zinc(II) [tris-(4-(benzothiazol-2-yl)phenoxy)- 3-(4-phenoxy)propanoic acid] phthalocyanine (6) and zinc(II) [tris-(3-(4-phenoxy)propanoic acid)-4-(bezothiazol-2-yl) phenoxyl] phthalocyanine (7).

Complexes **6** and **7** were synthesized by a statistical cross–condensation reaction of 4-[4-(benzothiazol-2-yl)phenoxy] phthalonitrile and 4-[3-(4-phenoxy)propanoic acid] phthalonitrile (mole ratios 5:1 and 1:5 respectively) in the presence of DBU, Zn salt and 1-pentanol as illustrated in **Scheme 3.4**.

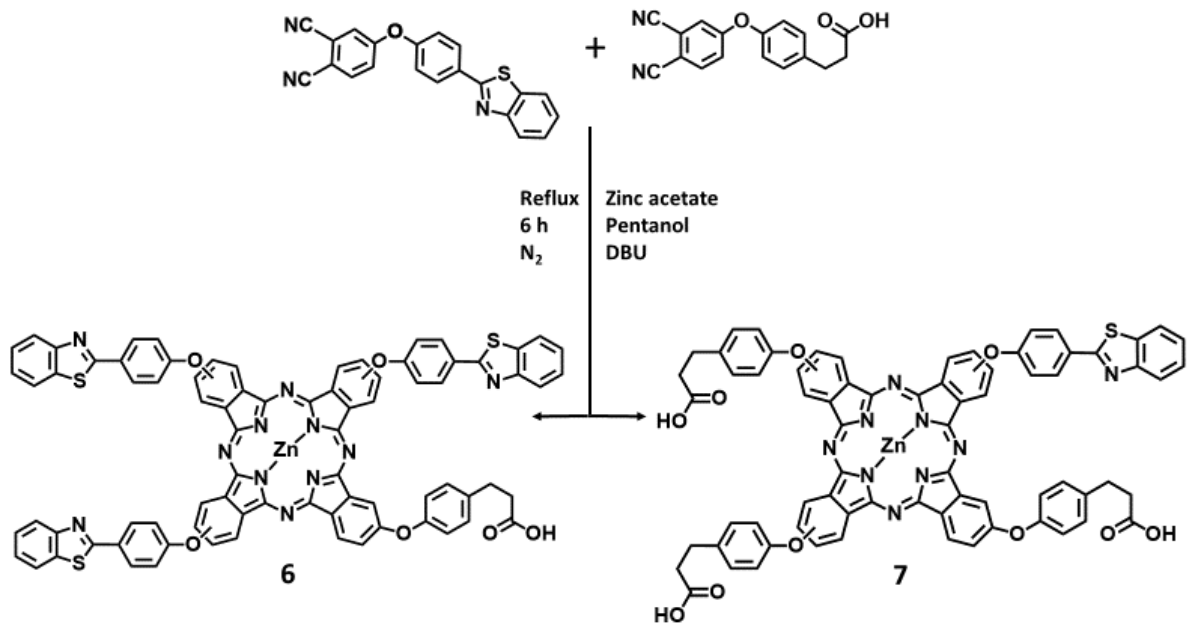

Scheme 3.4: Synthetic route for complexes **6** and **7**.

The disappearance of the characteristic C≡N peak of the dinitriles at 2238 cm^{-1} and 2230 cm^{-1} in the FT-IR spectrum for complexes **6** and **7** respectively confirmed the conversion of the phthalonitriles to phthalocyanines.

The ^{1}H NMR spectrum for complex **6** displayed peaks due to aromatic ring protons at 8.82 – 6.70 ppm, the CH_2 protons at 4.07 ppm and 3.02 ppm, and the proton due to the hydroxyl group of a carboxylic acid at 12.27 ppm.

On the other hand, the ^{1}H NMR spectrum for complex **7** exhibited aromatic ring proton peaks between 7.81–7.09 ppm, the CH_2 protons of the propionic acid chain at 2.89 ppm and 2.65 ppm, and the protons due to the hydroxyl groups of the carboxylic acid moiety at 11.32 ppm. Peak integration for both complexes gave the expected number of protons, confirming the purity of the Pcs. The mass spectral data (**Figure 3.5**) for complex **6** gave *m/z*: 1416.74 $[M-H]^+$) and complex **7** gave *m/z*: 1295.40 $[M]^+$, and elemental analyses agreed with the proposed structure in **Scheme 3.4**.

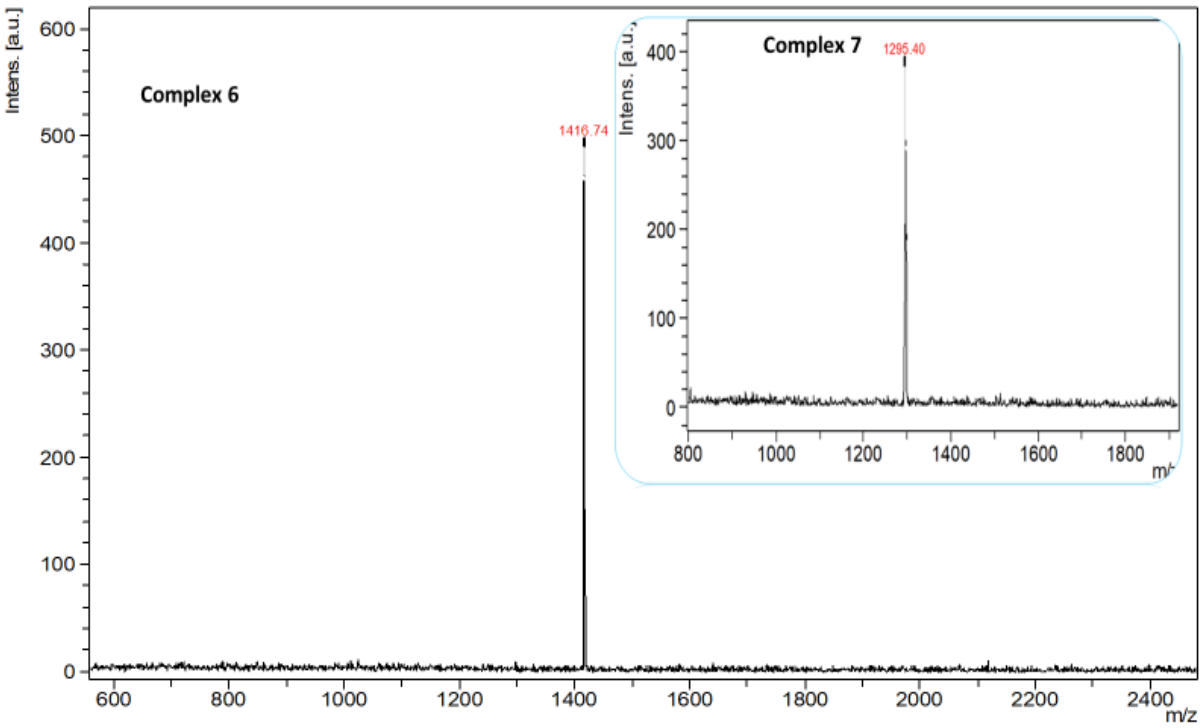

Figure 3.5: The MS (Maldi-TOF) for complexes **6** (and **7** insert).

An overlay of the normalized absorption spectra of complexes **6** and **7**, is shown in **Figure 3.6**.

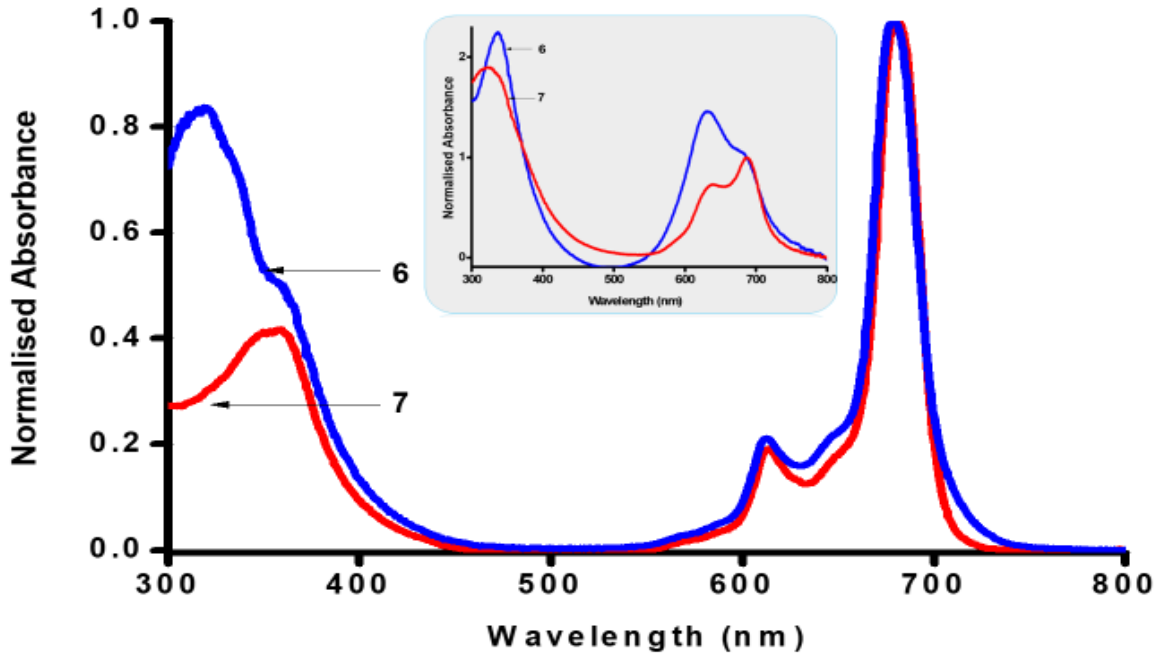

Figure 3.6: The ground state absorption spectra for complexes **6** and **7** in DMSO (and water with 1.6% DMSO; insert).

The complexes displayed a single Q band at 680 nm and 681 nm in DMSO, (**Table 3.1)**. There is insignificant difference between the absorption spectra of the two complexes except that complex **6** with three benzothiazole groups showed intense absorption in the B-band region. This is probably because benzothiazole groups absorb within the same region. In water with 1.6% DMSO (**Figure 3.6** insert), the Q-bands are broad due to aggregation, typical of Pcs in aqueous solution due to π–π stacking interaction of the aromatic rings of Pcs as explained above.

3.1.5. Zinc(II) [(tris- (2,2,7,7-tetramethyltetrahydro-3aH-bis([1,3] dioxolo)[4,5-b:4',5'-d]pyran-5-yl)methoxy)-2-(4-benzothiazol-2-yl)phenoxy] phthalocyanine (8)

Complex **8** was synthesized through cross–condensation of a 4-glycosylated phthalonitrile and 4-[4-(benzothiazol-2-yl)phenoxy] phthalonitrile in the presence of DBU, zinc acetate, and 1-pentanol in an inert nitrogen atmosphere, **Scheme 3.5**.

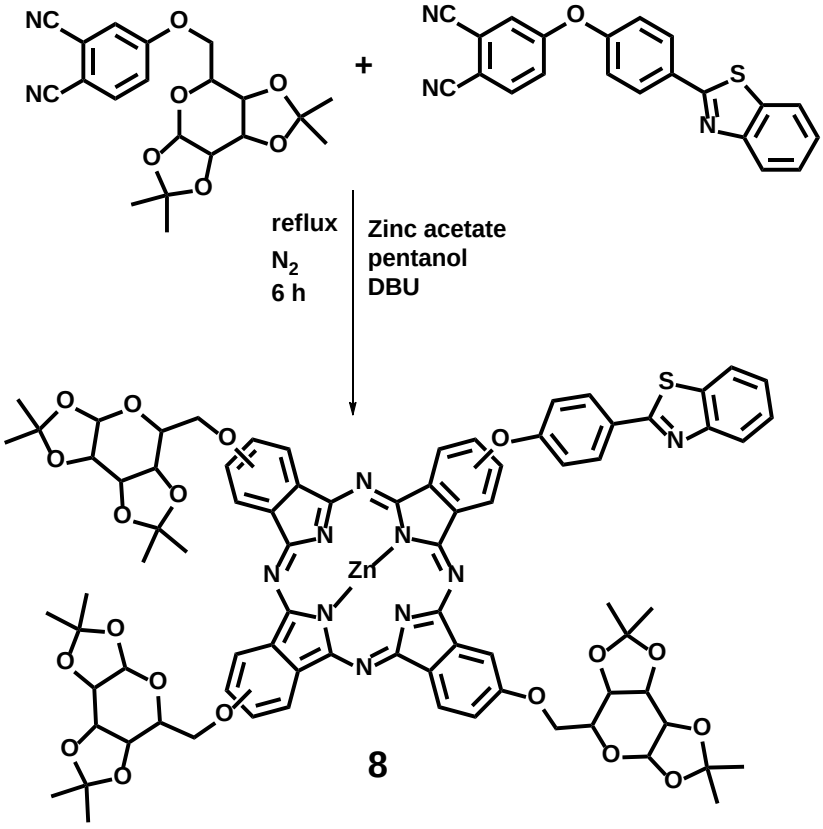

Scheme 3.5: Synthetic route for complex **8**.

The disappearance of a phthalonitrile C≡N peak at 2234 cm^{-1} in the FT-IR spectrum for **8** confirmed the formation of the MPc. The ^{1}H NMR spectrum displayed aromatic ring proton signals between 8.13 – 7.16 ppm.

The propyledene sugar ring protons were observed between 5.50 – 4.09 ppm, while the CH_3 protons on the sugar were observed between 1.44 – 1.29 ppm. Signal integration gave the anticipated number of protons, confirming the purity of the complex. Mass spectral data (*m/z*: 1578.44 $[M+H]^+$) and elemental analyses agreed with the proposed structure for complex **8**.

The complex displayed a single Q band at 681 nm in DMSO, however in water with 1.6% DMSO there was broadening of the Q band due to aggregation as previously mentioned.

Table 3.1: Q-band absorbance of complexes and their conjugates in DMSO

Pc	**Q band (nm)[a]**
Complex **1**	691 (708)
1-Ag_1Au_3NSs-GSH	687 (704)
1-Ag_3Au_1NSs-GSH	689 (705)
1-Ag_3Au_1SiNSs- APTES	691 (702)
Complex **2**	680 (689)
2-AuNTs-GSH	680 (687)
2-AuNSs-GSH	679 (685)
2-AgNSs -GSH	680 (686)
2-Ag_3Au_1NSs-GSH	678 (694)
Complex **3a**	679 (688)
3a-AuNTs-CTAC	679 (684)
3a-AuNSs-CTAB	680 (685)
3a-GSS	680 (687)
Complex **3b**	690 (705)
3b-AuNTs-CTAC	693 (687)
3b-AuNSs-CTAB	692 (686)
3b-GSS	693 (701)
Complex 4a	682 (695)
4a-AuNTs-CTAC	681 (684)
4a-AuNSs-CTAB	682 (685)
4a-GSS	681(694)
Complex 4b	695 (712)
4b-AuNTs-CTAC	694 (707)
4b-AuNSs-CTAB	695 (701)
4b-GSS	697 (711)
Complex 5	675 (686)
5-AuNTs-GSH	673 (685)
5-AuNSs-GSH	674 (684)
5-AgNSs -GSH	674 (683)
5-Ag_3Au_1NSs-GSH	673 (684)
Complex 6	680 (687)
6-AuNTs-GSH	681 (685)
6-AuNSs-GSH	679 (684)
6-AuNTs-CTAC	680 (689)

6-AuNSs-CTAB	680 (687)
[b] **6**-AuCT	679 (681)
[b]**6**-CT	681 (683)
Complex 7	681(687)
7-AuNTs-GSH	680 (686)
7-AuNSs-GSH	681(685)
7-AuNTs-CTAC	681 (682)
Complex 8	681 (684)
8-AuNSs-CTAB	681 (684)
8-AuNRs-CTAB	682 (684)

[a]numbers in brackets are the values in water (with 1.6% DMSO). CTAB and CTAC left on the conjugate names to show the starting capping agent on the NPs.
[b]values obtained in 1% acetic acid in DMSO or water (with 1.6% DMSO).

3.2. Nanoparticles and composites

This section outlines the synthesis and the characterization of the nanoparticles (NPs) and composites

3.2.1. Gold and silver nanoparticles

The syntheses of GSH capped AgNSs-GSH [179], AuNSs-GSH [180], as well as the CTAB capped AuNSs-CTAB, AuNRs-CTAB [181] and CTAC capped AuNTs-CTAC [182] have been reported before. Ag_3Au_1NSs-GSH, Ag_1Au_3NSs-GSH [122], GSS [183,184] and AuCT [186,187] are also known but were synthesised with modification. The synthesis and characteisation of Ag_1Au_3NSs-APTES and AuNTs-GSH are reported for the first time.

The alloy nanoparticles Ag_1Au_3NSs-OA/OLA and Ag_3Au_1NSs-OA/OLA were synthesised using oleic acid and oleylamine as surfactants, solvents, reducing and stabilizing agents. This method was chosen specifically for alloys since the amine group in oleylamine can co-reduce both gold and silver ions to produce nanoalloys at high temperature [193,194]. The weakly bound OA/OLA on the nanoparticles are readily displaced with either glutathione or APTES.

AuNRs, AuNSs and AuNTs were synthesised using the seed growth method, using CTAB as a capping agent for AuNRs and AuNSs, and CTAC for AuNTs. The capping agent that produced a high yield based on literature was chosen [181,182]. For the GSH functionalised NPs, the weakly absorbed

capping agent on the nanoparticles are readily displaced with GSH.

The absorption spectra of the spherical silver (AgNSs-GSH) and gold (AuNSs-CTAB/ AuNSs-GSH) nanoparticles showed their characteristic surface plasmon resonance (SPR) peaks at 420 nm and 525/532 nm respectively (spectra not shown). The normalised absorption spectra of AuNTs-CTAC and AuNRs-CTAB are shown in **Figure. 3.7**.

For AuNTs-CTAC, an intense band (dipole) around 638 nm and a weak shoulder (quadrupole) around 528 nm are observed, and these are attributed to the in-plane dipole and out-of-plane dipole resonance of gold nanoplates, respectively, which are characteristic bands of AuNTs [195,196], **Figure. 3.7A**. The absorption spectrum for AuNTs-GSH (not shown) was similar to that of AuNTs-CTAC with the dipole peak at 607 nm and the quadrupole peak around 532 nm. The differences in the positions of the dipole peaks for AuNTs-ATAC and AuNTs-GSH could be due to the differences in the sizes of NTs (AuNTs-CTAC 52.7/62.3 nm and AuNTs-GSH, 33.2 nm edge length) as shown in **Table 3.2**.

The insert in **Figure. 3.7A** shows the TEM micrographs of the AuNTs-CTAC as a representative for AuNTs-GSH. The image shows different sizes of nanotriangles, which could be responsible for the dipole peak at 638 nm (for larger size) and a shoulder peak at 600 nm (for smaller size) in the absorption spectrum of AuNTs- CTAC, **Figure 3.7A**. In addition to AuNTs, the TEM image also shows a few irregular nanoparticles, hexagons and

spheres, which could be responsible for the quadrupole peak in the absorption spectrum [196].

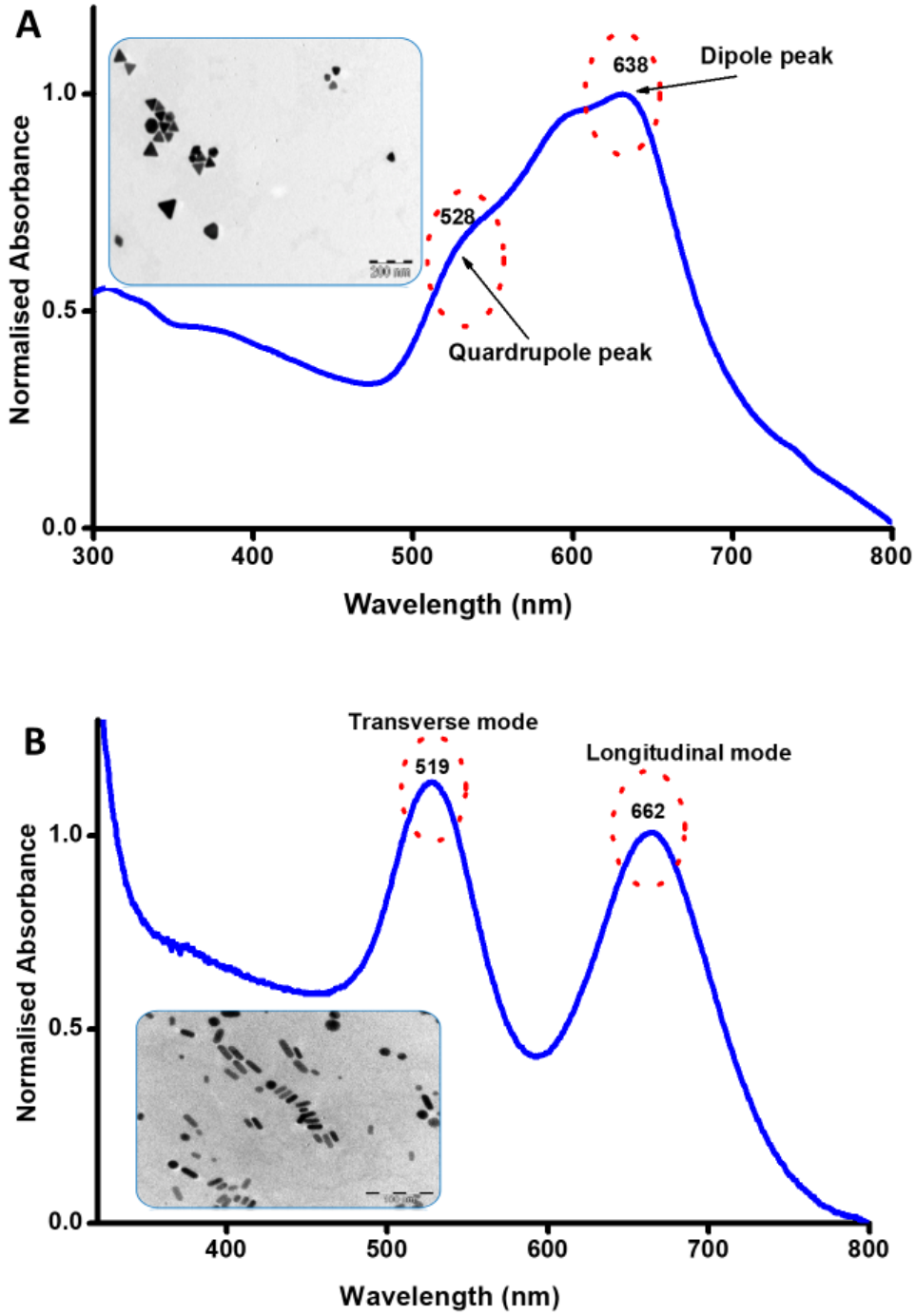

Figure 3.7: The normalized absorption spectrum for AuNTs-CTAC and AuNRs-CTAB (insert shows TEM images of NPs).

On the other hand, AuNRs–CTAB (**Figure. 3.7B**) displayed two SPR bands at 519 nm and 662 nm, due to their anisotropic shape (as shown by the TEM micrograph in **Figure. 3.7B**, insert) corresponding to their width and length known as the transverse mode and longitudinal mode, respectively [197].

X-ray diffractometry was used to give structural information of NPs and their conjugates with relation to the broadness or sharpness of the XRD peaks, which is indicative of their amorphous or crystalline nature. The powder XRD pattern for AuNSs-CTAB is shown in **Figure 3.8**, as a representative of other AuNPs (AuNSs-GSH, AuNRs-CTAB, AuNTs-GSH and AuNTs-CTAC). The XRD displayed peaks around 2θ = 38.4°, 44.7°, 64.9°, 77.6° and 81°, showing crystallinity (matching the pattern in card number, 03-065-2870; NIST:N AL3280 from the powder diffraction database). These peaks were assigned to the 111, 200, 220, 311 and 222 planes respectively, corresponding to the face centered cubic crystal (FCC) structure of metallic gold [198,199].

Size estimates from XRD were obtained only for some NPs using the Debye–Scherrer [200] as shown in equation 3.1, by focusing on the peaks at plane 111:

$$d = \frac{k\lambda}{\beta\cos\theta} \qquad (3.1)$$

where λ is the wavelength of the X-ray source (1.5405 Å), k is an empirical constant equal to 0.9, β is the full width at half maximum of the diffraction peak and θ is the angular position. The size estimates are shown in **Table 3.2** and will be discussed later.

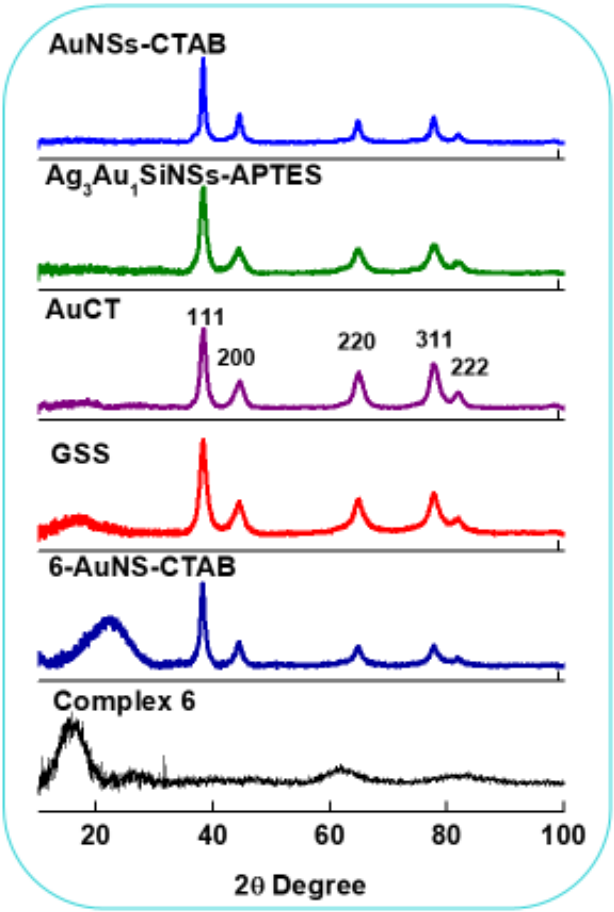

Figure 3.8: XRD patterns for AuNSs-CTAB, Ag_3Au_1SiNSs–APTES, AuCT, GSS, **6**-AuNSs-CTAB and complex **6** as representatives.

Table 3.2: Sizes and loading of conjugates.

Sample	**Size[a] (nm)**	**Loading (μg/mg)**
Complex 1		
1-Ag_1Au_3NSs-GSH	21.1 (18.9) XRD	[c]
1-Ag_3Au_1NSs-GSH	17.5 (15.1) XRD	[c]
1-Ag_3Au_1SiNSs- APTES	[b](73)	19
Complex 2		
2-AuNTs-GSH	34.9 (33.2)	22
2-AuNSs-GSH	14.9 (13.6)	27
2-AgNSs -GSH	14.7 (11.1)	9
2-Ag_3Au_1NSs-GSH	17.3 (15.1)	41
Complex 3a		
3a-AuNTs-CTAC	54.6 (52.7)	15
3a-AuNSs-CTAB	16.4 (15.2)	22
3a-GSS	88.1 (81.7)	50
Complex 3b		
3b-AuNTs-CTAC	55.9 (52.7)	20
3b-AuNSs-CTAB	16.9 (15.2)	32
3b-GSS	86.4 (81.7)	48
Complex 4a		
4a-AuNTs-CTAC	54.9 (52.7)	24
4a-AuNSs-CTAB	17.2 (15.2)	37
4a-GSS	81.7 (78.4)	51
Complex 4b		
4b-AuNTs-CTAC	[b] (52.7)	17
4b-AuNSs-CTAB	16.7 (15.2)	29
4b-GSS	82.3 (78.4)	49
Complex 5		
5-AuNTs-GSH	36.9 (33.2)	16
5-AuNSs-GSH	13.8 (13.6)	20
5-AgNSs-GSH	12.2 (11.1)	10
5-Ag_3Au_1NSs-GSH	16.5(15.1)	28
Complex 6		
6-AuNTs-GSH	37.1 (33.2)	30
6-AuNSs-GSH	19.8 (17.7)	37
6-AuNTs-CTAC	66.8 (62.3)	42

6-AuNSs-CTAB	13.4 (11.7) DLS	37
6-AuCT	357 (345) DLS	32
6-CT	329 (324) DLS	28
Complex 7		
7-AuNTs-GSH	35.3 (33.2)	26
7-AuNSs-GSH	17.1 (14.9)	38
7-AuNTs-CTAC	65.7 (62.3)	33
Complex 8		
8-AuNSs-CTAB	15.28 (13.4)	8
8-AuNRs-CTAB	3.2 (2.1)	14

[a]numbers in brackets are the sizes of NPs alone and the sizes are from TEM unless otherwise stated.

[a]The the edge length was measured for all nanotriangles and diameters for the spheres. Aspect ratios were used for the nanorods.

[a]Note: Size of the NPs of the same shape varies because they were prepared in different batches.

[b]Sizes not obtained due to extensive aggregation.

[c]Sample no longer available for the study and since both NP synthesis and loading are sensitive to conditions it will be difficult if not impossilbe to reproduce the conjugate with the same loading.

3.2.2. Ag_xAu_y alloy nanoparticles.

The alloy NPs Ag_3Au_1NSs-GSH, Ag_1Au_3NSs-GSH and Ag_3Au_1SiNSs-APTES were synthesised as illustrated in **Scheme 3.6.** The weakly bound OA/OLA on the nanoparticles were replaced by glutathione, **Scheme 3.6A**.

For the synthesis of Ag_3Au_1SiNSs-APTES, silica was grown on Ag_3Au_1NSs surfaces using hydrolysis and condensation of tetraethyl orthosilicate (TEOS) under basic conditions, allowing a slow, controlled growth of a shell around the alloys [183]. The silica shell was further functionalised through the displacement of hydroxyl groups on the silica shell with the alkoxy groups on APTES thus forming a covalent -Si-O-Si- bond, **Scheme 3.6B**.

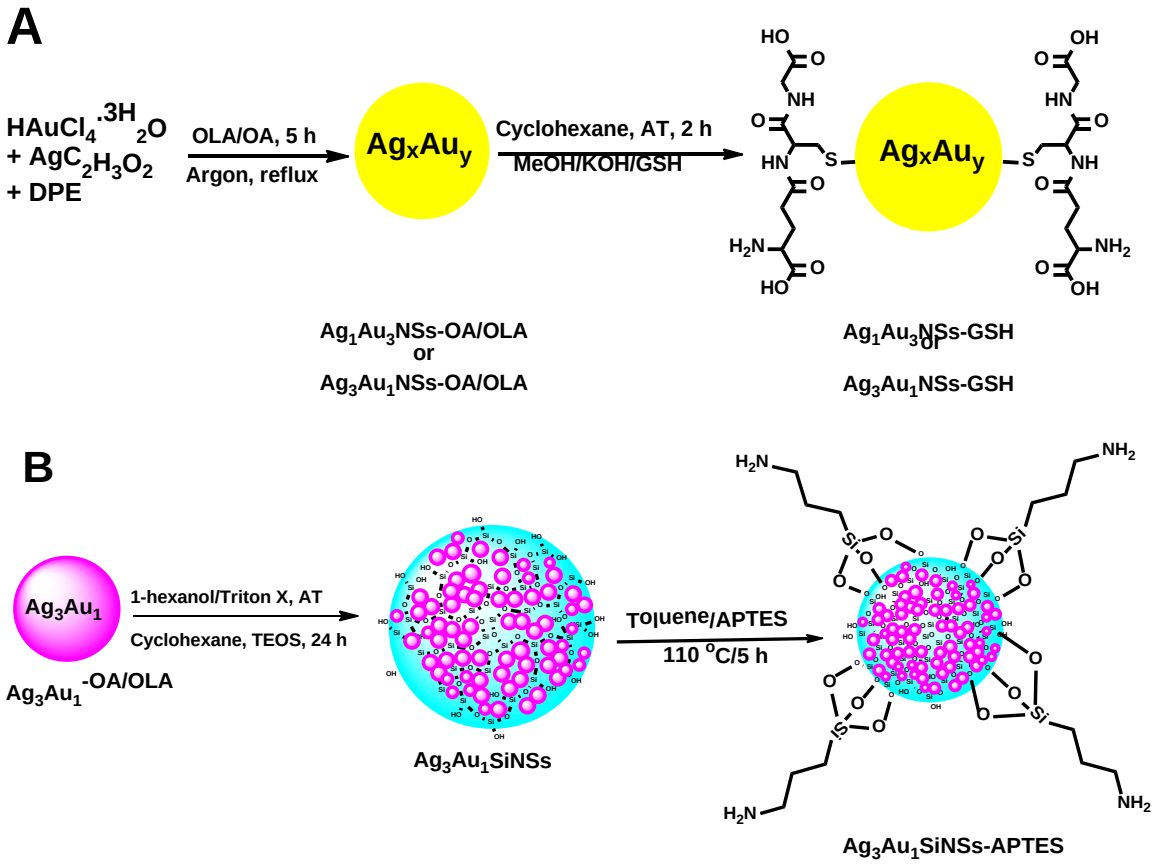

Scheme 3.6: Synthetic route for (A) Ag_3Au_1NSs-GSH, Ag_1Au_3NSs-GSH and (B) Ag_3Au_1SiNSs-APTES.

The surface plasmon resonance peaks of Ag_3Au_1NSs-GSH and Ag_1Au_3NSs-GSH were observed at 410 nm and 506 nm in DMSO, respectively (**Figure 3.9**). The SPR peaks of these alloys are very close to the SPR positions of individual AgNSs and AuNSs, depending on the composition of Ag or Au present in the alloys [201].

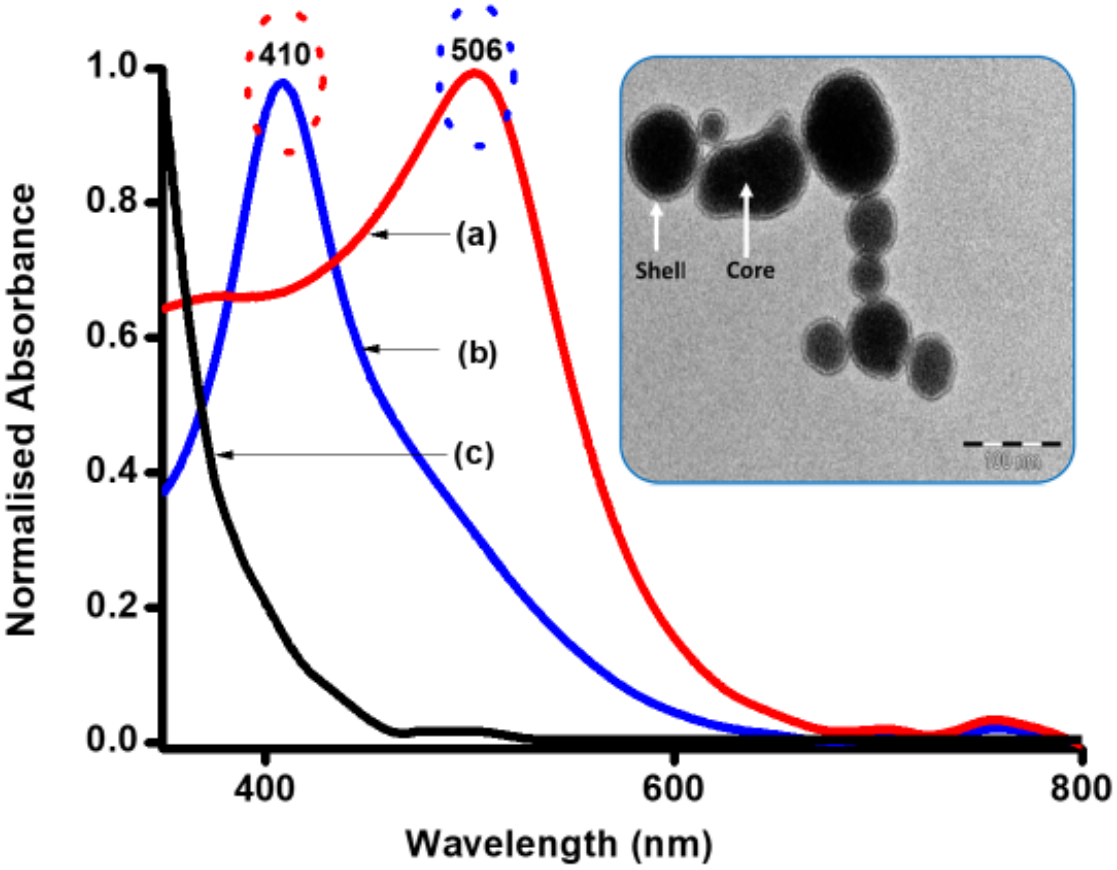

Figure 3.9: The normalized absorption spectrum for Ag_1Au_3NSs-GSH (a) Ag_3Au_1NSs-GSH (b) and Ag_3Au_1SiNSs- APTES (c) (insert shows TEM image of Ag_3Au_1SiNSs- APTES).

No significant absorption peak was observed for Ag_3Au_1NSs in Ag_3Au_1SiNSs-APTES (**Figure 3.9c**) which could be attributed to successful doping of the NPs into SiNSs. Hence the Ag_3Au_1NSs are not exposed and do not show the SPR band. This confirms that the Ag_3Au_1NSs are embedded within the SiNSs.

The TEM image of the Ag_3Au_1SiNSs–APTES, **Figure 3.9** insert, shows a dark core with a light ring around it (shell), an indication that silica has formed a coat on the Ag_3Au_1NSs surface.

The powder XRD pattern for Ag_3Au_1SiNSs–APTES is shown in **Figure 3.8**, and it is a representative for Ag_3Au_1NSs-GSH and Ag_1Au_3NSs-GSH. The pattern corresponds to the FCC structure of metallic gold as previously explained. However it should be noted that gold and silver have the same pattern [198,199], (which matches the pattern in card number, 01-071-9134; ICSD 104385 from the powder diffraction database).

It is important to note that XRD pattern is observed for Ag_3Au_1 within Ag_3Au_1SiNSs–APTES while the SPR band was not observed in the absorption spectrum (**Figure 3.9c**) due to the penetrating nature of the XRD. The diffraction pattern does confirm the presence of Ag_3Au_1 within the SiNSs.

3.2.3. Gold speckled silica (GSS) nanoparticles.

Gold-speckled silica (GSS) nanoparticles were synthesized using 3-aminopropyl-triethoxysilane (APTES) functionalised silica nanospheres (SiNSs-APTES) [183,184] and gold nanoparticles seeds [185] as explained in literature, **Scheme 3.7**.

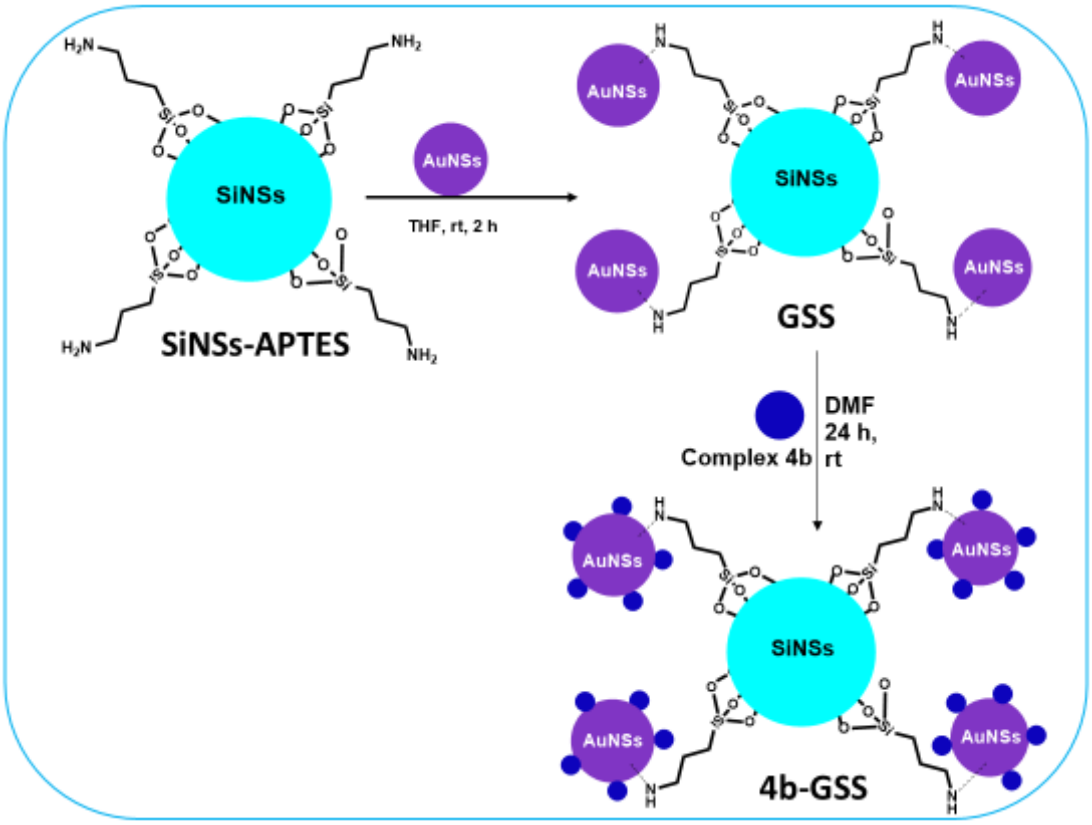

Scheme 3.7. Synthetic route of GSS (rt = room temperature).

GSS displayed a maximum absorption band at 599 nm (**Figure 3.10)** which is attributed to the surface plasmon resonance (SPR) peak of the nanogold on silica surfaces which is more red-shifted compared to the reported values [93] for GSS, probably due to the larger size of GSS.

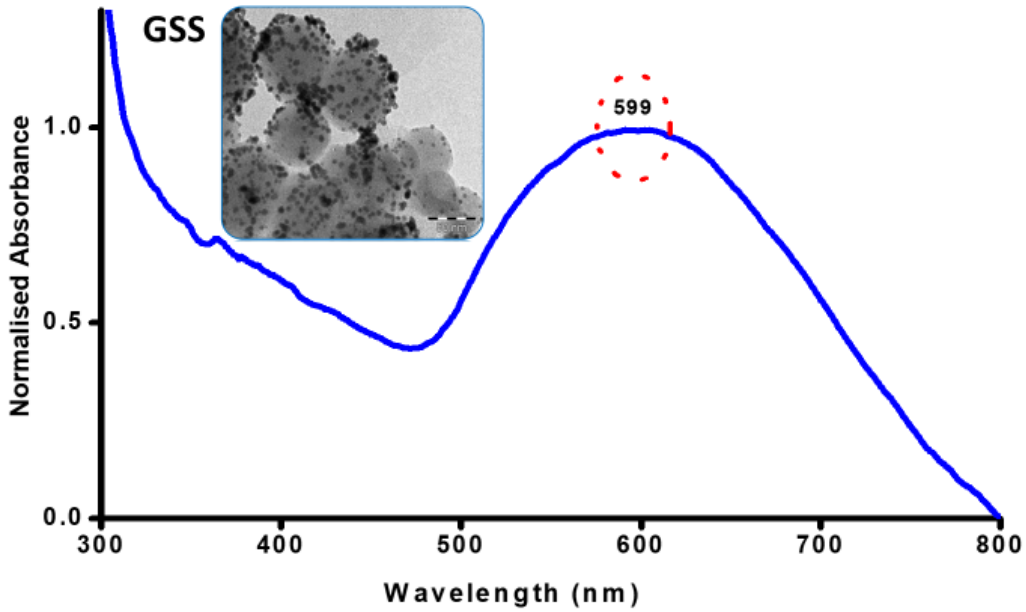

Figure 3.10: The normalized absorption spectrum for GSS (insert shows TEM images of NPs).

The TEM micrograph for GSS, **Figure 3. 10** (insert), shows discontinuous and random deposits of nanogold (as shown by small darker spheres) on silica surfaces, confirming the formation of gold speckled SiNSs (GSS).

The powder XRD pattern for GSS is shown in **Figure 3.8**. The pattern corresponds to the FCC structure of metallic gold as previously explained, however a broad peak was observed at $2\theta = 10°$ to $22°$, and it was attributed to the amorphous nature of SiNSs in GSS.

3.2.4. Chitosan and gold chitosan composite.

The AuCT composite was synthesised using a CT solution and AuNSs as illustrated in **Scheme 3.8.**

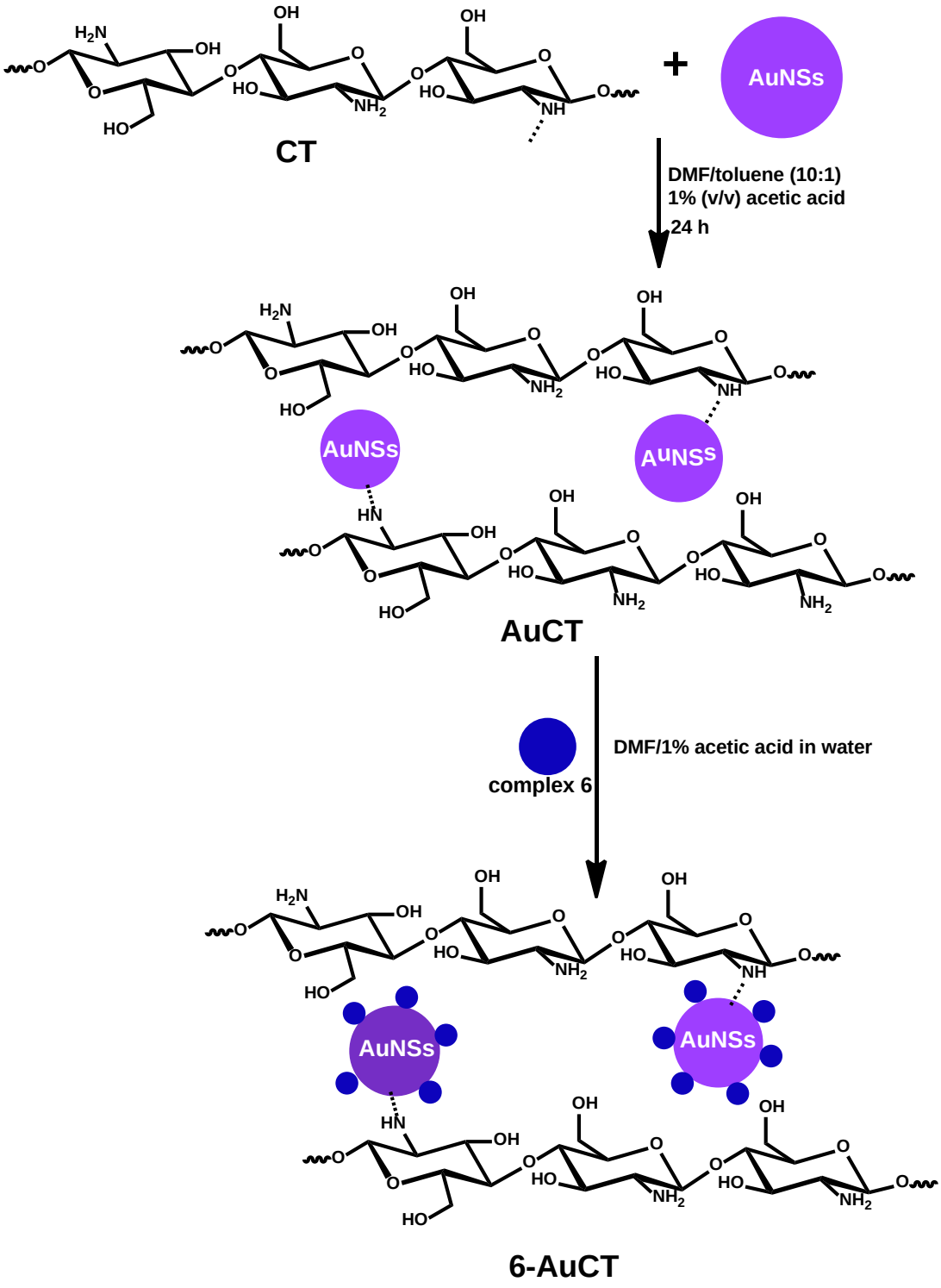

Scheme 3.8: Synthetic route for AuCT and **6**-AuCT.

CT alone (**Figure 3.11**), showed minimal absorption between 500 nm and 800 nm. After linkage with AuNPs to form AuCT, an SPR peak was observed at 548 nm, signifying the presence AuNPs in chitosan, **Figure 3.11**. The reduced intensity of the Au SPR peak could be an indication that some of the Au is embedded inside the biopolymer.

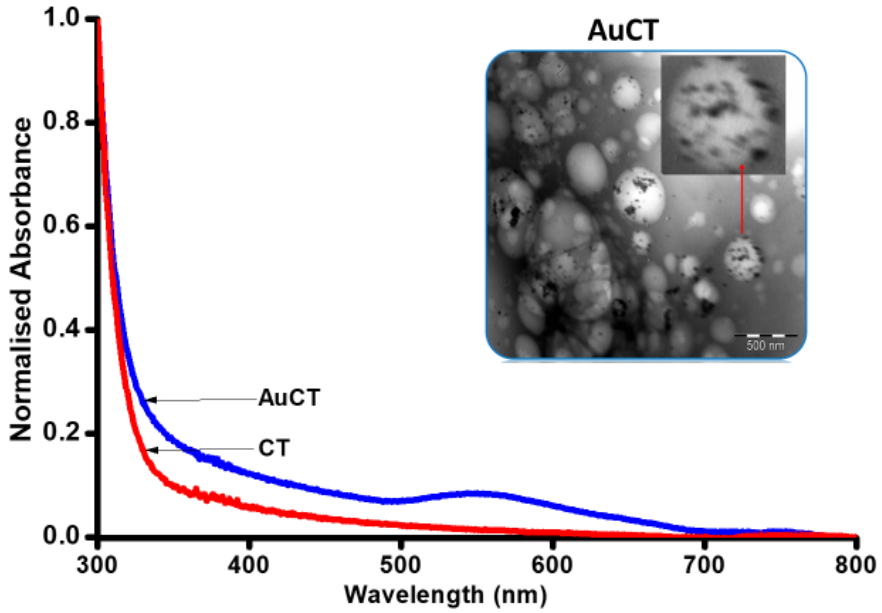

Figure 3.11: The normalized absorption spectrum for CT and AuCT (insert shows TEM images of AuCT composite).

The powder XRD pattern for AuCT corresponds to the FCC structure of metallic gold as previously explained (**Figure 3.8**) and slight boadening was observed between 2θ = 10° to 22°, probably due to the amorphous nature of CT.

Dynamic light scattering (DLS) is a light scattering technique used to determine the size-distribution profile of molecules (emulsions, micelles, polymers or nanoparticles) in solution. DLS was used to determine the size of CT, AuCT and their conjugates to complex **6**, **Figure 3.12** and the size estimates are shown in **Table3.2**. The sizes will be discussed below (section 3.3.3).

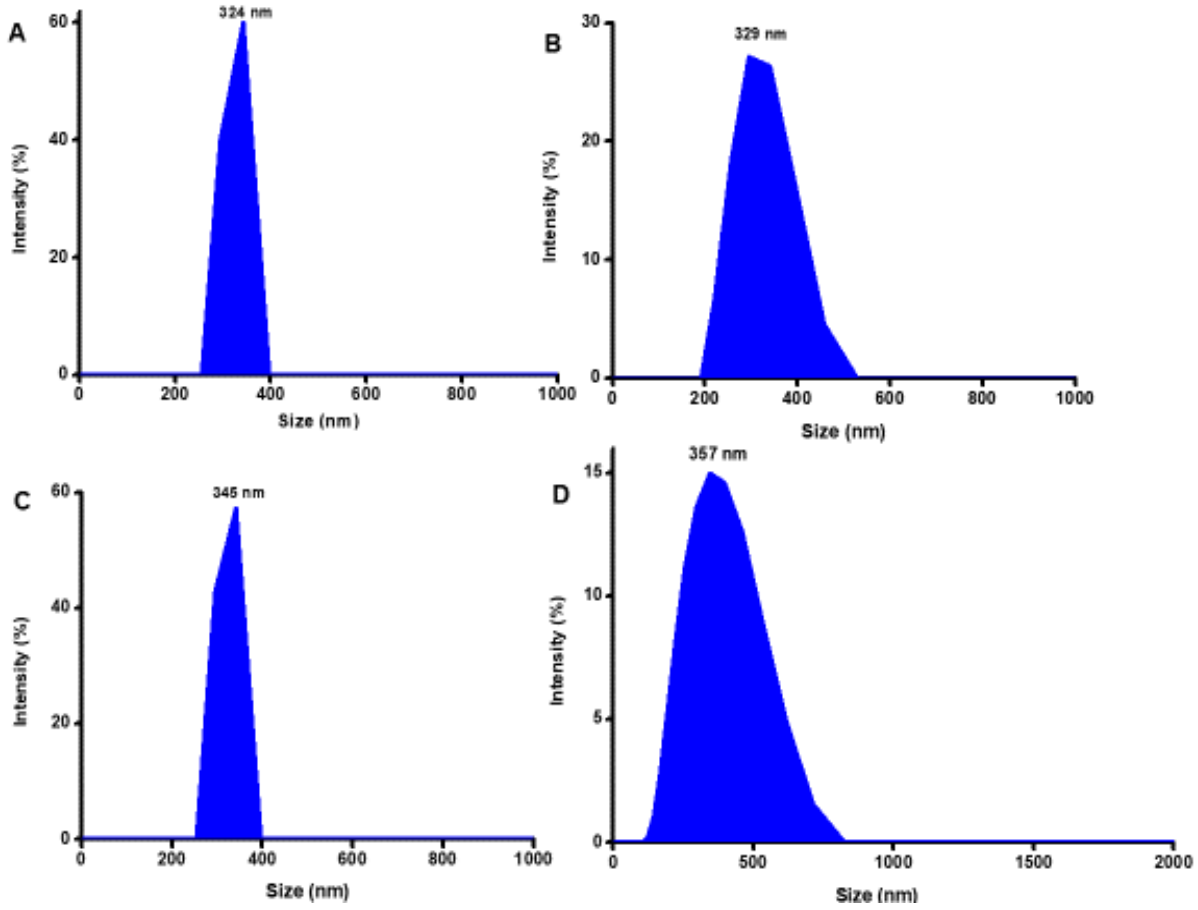

Figure 3.12. Dynamic light scattering curves for CT (A), 6-CT (B), AuCT (C) and **6**-AuCT (D) in 1% (v/v) aqueous acetic acid solution (containing 1.6% (v/v) DMSO for **6**-CT and **6**-AuCT).

3.3. Metallophthalocyanines–nanoparticles conjugates.

MPcs were linked to NPs through either an amide bond formed between the -COOH group of the MPcs and the -NH_2 of the GSH or APTES functionalised NPs or directly through self-assembly, taking advantage of the affinity of gold within the NPs for S or N in the complexes.

3.3.1. Conjugates to GSH or APTES functionalised NPs (amide bond).

Complexes **1**, **2**, and **5**-**7**, all with a -COOH group (**Table 1.1**), were covalently linked to glutathione functionalised NPs (and 3-aminopropyl-triethoxysilane functionalized NPs for complex **1**) via an amide bond. **Scheme 3.9** shows the covalent linkage of complex **1** to Ag_3Au_1SiNSs-APTES and Ag_1Au_3NSs-GSH (as examples).

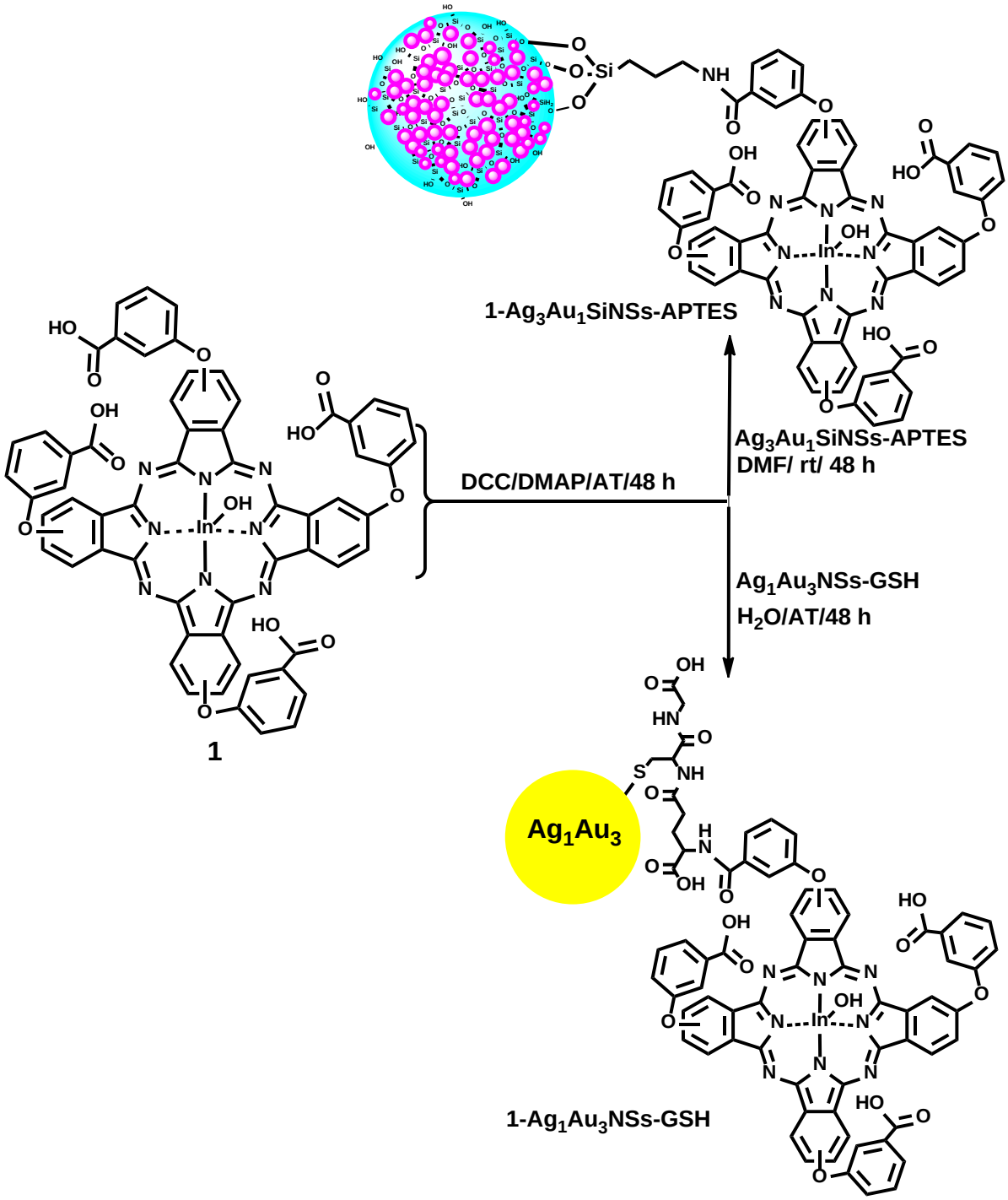

Scheme 3.9: Synthetic route for **1**-Ag_3Au_1SiNSs-APTES and **1**-Ag_1Au_3NSs-GSH (DCC= N,N'-dicyclohexylcarbodiimide; DMAP= 4-(dimethylamino)pyridine; rt= room temperature)

The FTIR spectra (**Figure. 3.13,** using AuNTs-GSH, **2**-AuNTs-GSH and complex **2**, as examples) were employed to prove amide bond formation between the Pc complexes and the NPs.

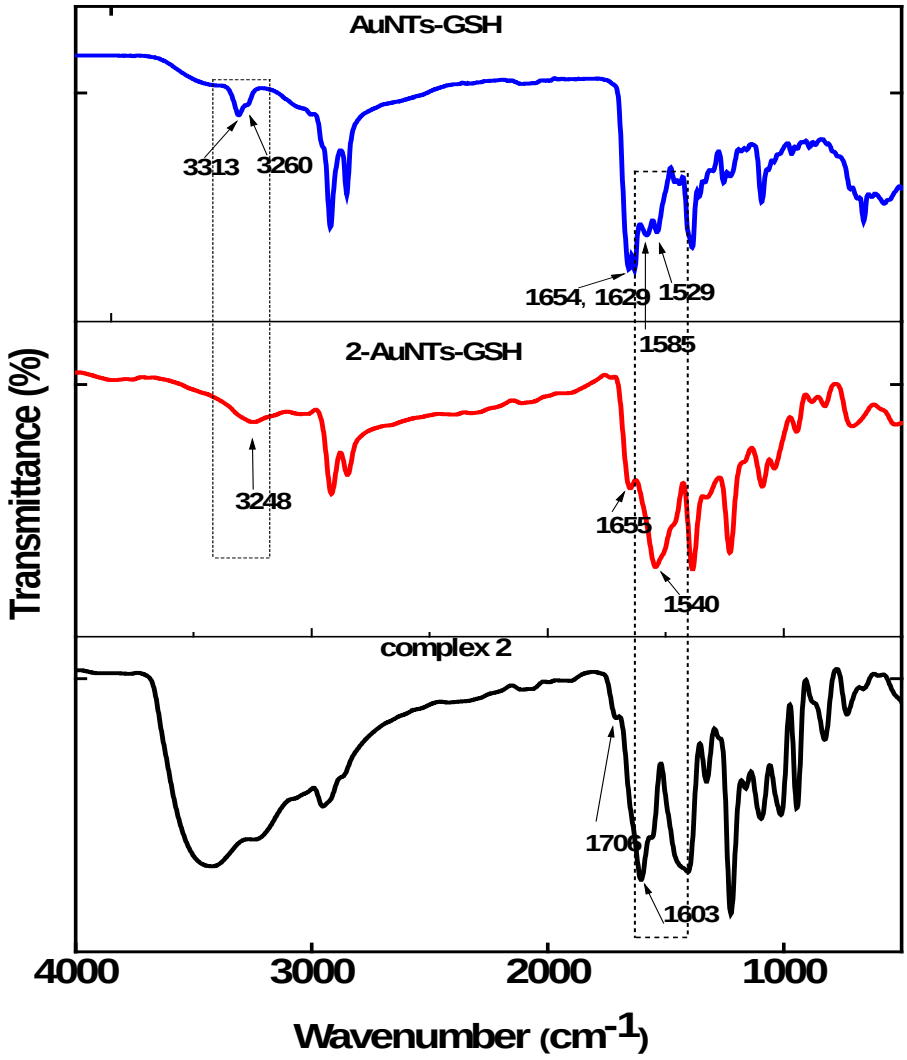

.

Figure 3.13: FTIR spectra of AuNTs-GSH, **2**-AuNTs-GSH and complex **2**.

The FTIR spectrum of AuNTs-GSH exhibited characteristic primary amide double peaks at 1529 cm^{-1} and 1585 cm^{-1} and also at 3260 cm^{-1} and 3313 cm^{-1} which changed to single (secondary amide) peaks at 1540 cm^{-1} and 3248 cm^{-1}, respectively on linkage of AuNTs-GSH to complex **2**, confirming the formation of an amide bond between glutathione functionalized NPs and the Pc complex. Also observed was the disappearance of 1706 cm^{-1} and 1603 cm^{-1} peaks in complex **2** and 1629 cm^{-1} in AuNTs-GSH. Shifts and changes in the IR bands confirm structural change [202]. An amide peak was observed

at 1655 cm^{-1} after conjugation; however, it should be noted that GSH alone has amide bonds shown by peaks at 1654 cm^{-1} and 1629 cm^{-1} in AuNTs-GSH. The same trend was observed for the conjugates: **1**-Ag_1Au_3NSs-GSH, **1**-Ag_3Au_1NSs-GSH, **1**-Ag_3Au_1SiNSs-APTES, **2**-AuNSs-GSH, **2**-AgNSs-GSH, **2**-Ag_3Au_1NSs-GSH, **5**-AuNTs-GSH, **5**-AuNSs-GSH, **5**-AgNSs-GSH, **5**-Ag_3Au_1NSs-GSH, **6**-AuNTs-GSH, **6**-AuNSs-GSH, **7**-AuNTs-GSH and **7**-AuNSs-GSH.

Figure 3.14A and **B**, shows the normalized absorption spectra for the conjugates of complexes **1** and **2** respectively, to glutathione functionalised NPs as examples. Slight blue shifts in the Q band of the conjugates (except for **1**-Ag_3Au_1SiNSs-APTES in DMSO) when compared to complex **1** alone were observed in both DMSO and water with 1.6% DMSO (**Table 3.1**). The slight blue shifts could be attributed to the electron deficiency induced on the Pcs upon coordination with NPs as reported before [203]. However, for complexes **2** and **5-8**, insignificant or no shifts in the Q-bands were observed (**Table 3.1**).

Phthalocyanines do not display any significant absorbance between the Soret band and the Q band; however on conjugation to gold NPs or silver NPs or gold-silver alloy NPs, all conjugates except **1**-Ag_3Au_1SiNSs-APTES, displayed increased absorption between the Soret and the Q band (**Figure 3.14A,B**)

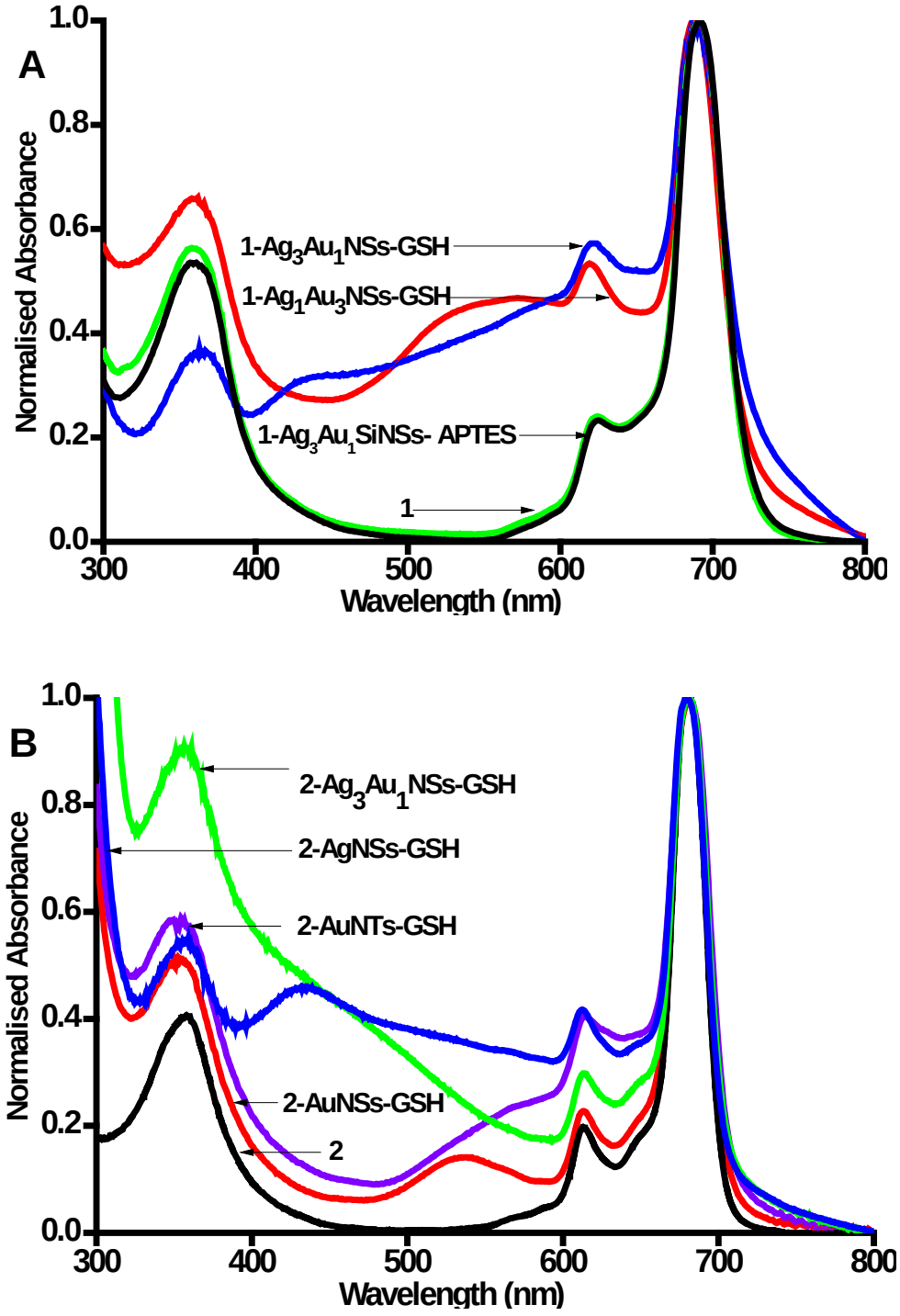

Figure 3.14: The normalized absorption spectra for (A) complex **1**, **1**-Ag_1Au_3NSs-GSH, **1**-Ag_3Au_1NSs-GSH and **1**-Ag_3Au_1SiNSs-APTES; (B) complex **2**, **2**-AuNTs-GSH, **2**-AuNSs-GSH, **2**-AgNSs-GSH and **2**-Ag_3Au_1NSs-GSH.

corresponding to the SPR band for the respective NPs, confirming the conjugation of NPs to complexes. The same enhancements were also observed for the conjugates in water with 1.6% DMSO (spectra not shown). The spectrum of **1**-Ag_3Au_1SiNSs-APTES both in DMSO (**Figure 3.14A**) or water with 1.6% DMSO (spectrum not shown) did not show these SPR bands as also observed for Ag_3Au_1SiNSs-APTES alone. Since complex **1** is linked to the surface of the SiNSs in **1**-Ag_3Au_1SiNSs-APTES, its spectrum is observed unlike for Ag_3Au_1SiNSs-APTES where the AuNSs and AgNSs are embedded within SiNSs, hence the SPR band is not observed.

The TEM micrographs of the conjugates (**Figure 3.15**, using **2**-AuNSs-GSS and **6**-AuNTs-GSH as representatives) generally displayed aggregation, possibly due to π-π stacking between the Pcs on adjacent nanoparticles. Pcs are known for their π-π stacking to form H aggregates [190].

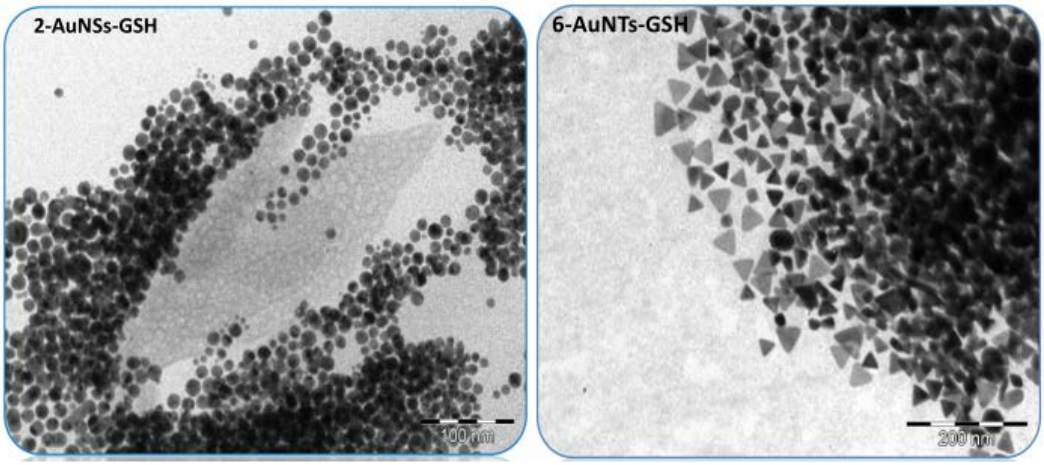

Figure 3.15: TEM images for **2**-AuNSs-GSH and **6**-AuNTs-GSH.

3.3.2. Au-S or Au-N self-assembly conjugates.

Complexes **3a**, **3b**, **6**, **7** and **8**, with a thiazole group together with **4a** and **4b**, with a thiophine group (**Table 1.1**), were linked to gold containing NPs (either AuNTs-CTAC or AuNSs-CTAB or AuNRs-CTAB or GSS or AuCT) via Au-S or Au-N interaction (the latter for the complexes with both N and S). **Scheme 3.10** shows the Au-S/Au-N interaction of complex **8** with AuNSs-CTAB, as a representative. The Au-S/Au-N interaction is also represented in **Scheme 3.8**, using **6**-AuCT.

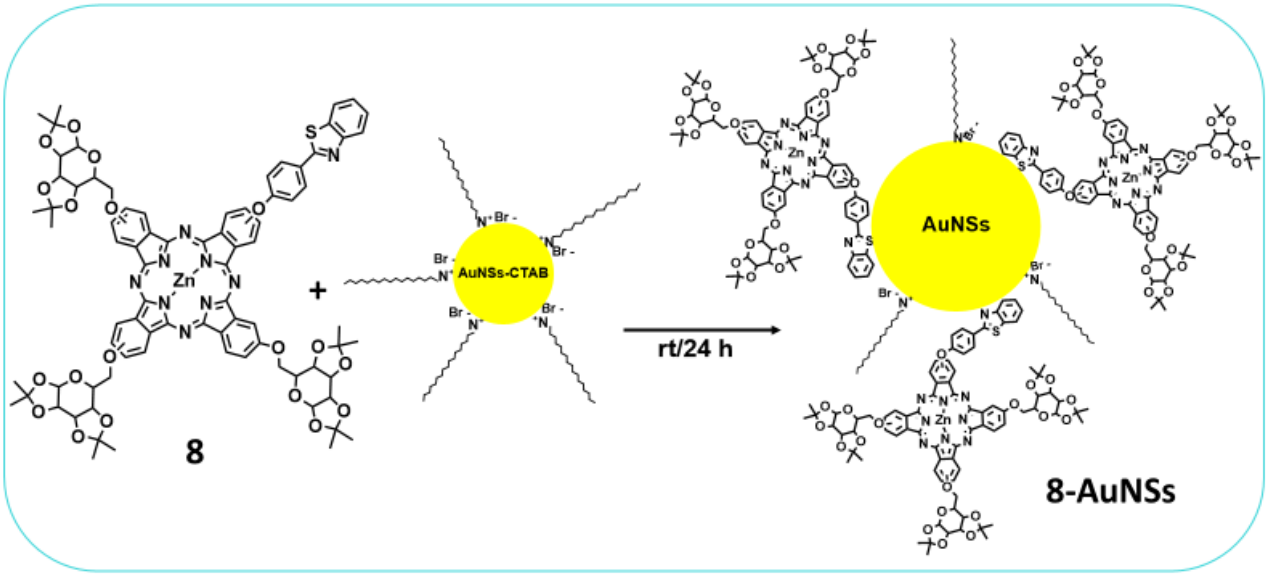

Scheme 3.10: Synthetic route for **8**-AuNSs-CTAB (rt = room temperature)

The capping agents CTAB and CTAC are loosely bound on the AuNPs, however on conjugation some of the capping agents are replaced by MPc complexes to form Au-S or Au-N bonds.

Upon conjugation of complexes **3a**, **3b**, **4a**, **4b**, **6**, **7** to AuNSs-CTAB and AuNTs-CTAC, and complex **8** to AuNSs-CTAB and AuNRs-CTAB, an

enhancement in absorption between the Q band and 500 nm was observed (**Figure. 3.16**, using the normalized absorption spectra of **8**, **8**-AuNSs-CTAB and **8**-AuNRs-CTAB as representatives), confirming successful linkage of the complexes to nanoparticles.

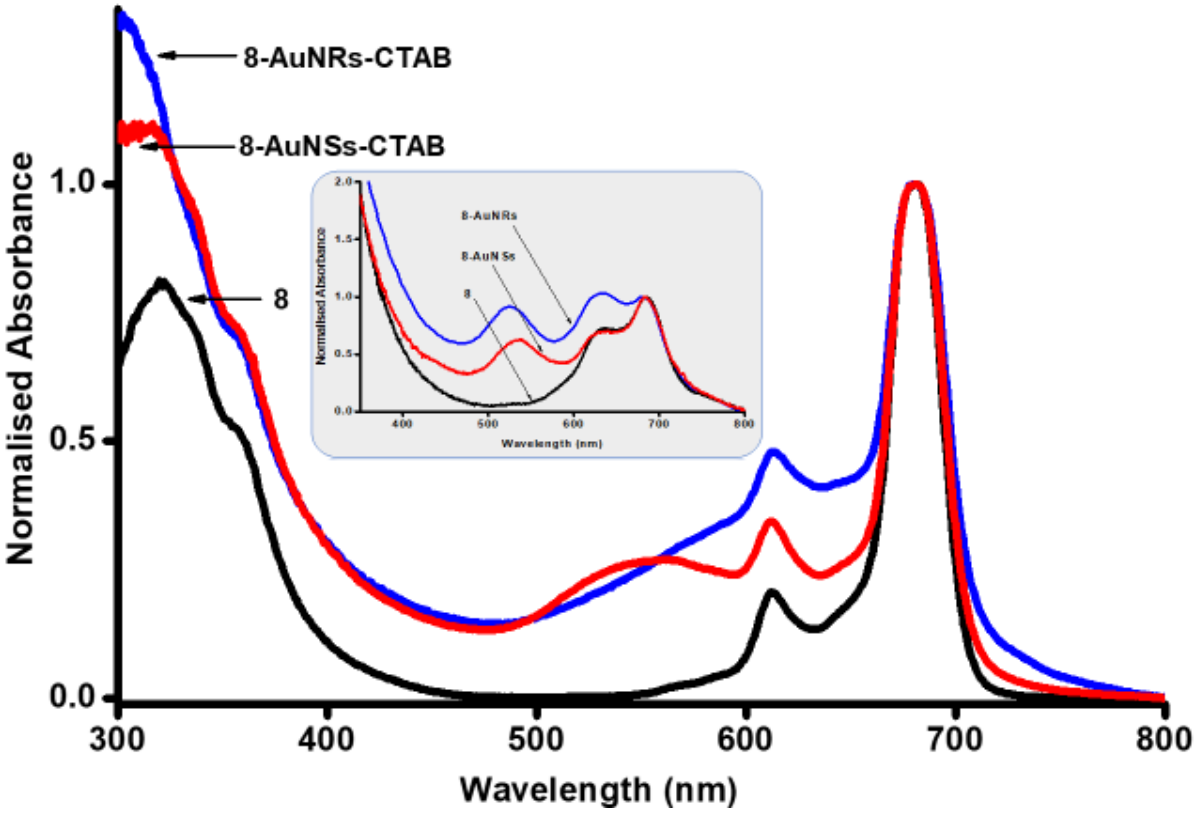

Figure. 3.16. The normalized absorption spectra for **8**, **8**-AuNSs-CTAB and **8**-AuNRs-CTAB in DMSO (and in water with 1.6% DMSO as shown by the insert).

Table 3.1 shows insignificant shifts in the Q-band absorbance of Pc complexes **3a**, **3b**, **4a**, **4b** and **6-8** in DMSO on conjugation. In water (with 1.6% DMSO), there is aggregation as discussed above (**Figure. 3.16** insert)

To confirm interaction between the gold containing NPs (AuNTs-CTAC, AuNSs-CTAB, AuNRs-CTAB, GSS and AuCT) and Pc complexes, XPS analysis was done. **Figure. 3.17** shows high resolution XPS spectra for complex **6** S2p, complex **6** N1s, **6**-AuCT S2p and AuCT N1s as representatives for other complexes and conjugates.

The S2p deconvolution for complex **6** alone (**Figure 3.17A**) exhibited two sub-peaks corresponding to –S–C– (161.9 eV) and –S– (163.0 eV) and similarly the N1s of the complex alone (**Figure 3.17B**) exhibited two sub-peaks corresponding to –N–C– (396.1 eV) and –N– (397.9 eV). The N1s peak for AuCT (**Figure 3.17D**) displayed three peaks attributed to –N–C– (397.8eV), –N– (399.7eV) and –N–Au– (400.7 eV). The nitrogen to gold interaction (–N–Au–) confirms successful linkage of CT to Au in AuCT **Figure 3.17D**.

The gold containing conjugate displayed three peaks (**Figure 3.17C**) attributed to –S–C– (162.3 eV), –S– (163.7 eV) and –S–Au– (164.9 eV). The sulphur to gold interaction (–S–Au–) confirms successful linkage of complex **6** to AuCT to form **6**-AuCT. Since complex **6** contains both S and N, a nitrogen to gold interaction (N-Au) was also expected, however this was not observed in the XPS spectra for **6**-AuCT.

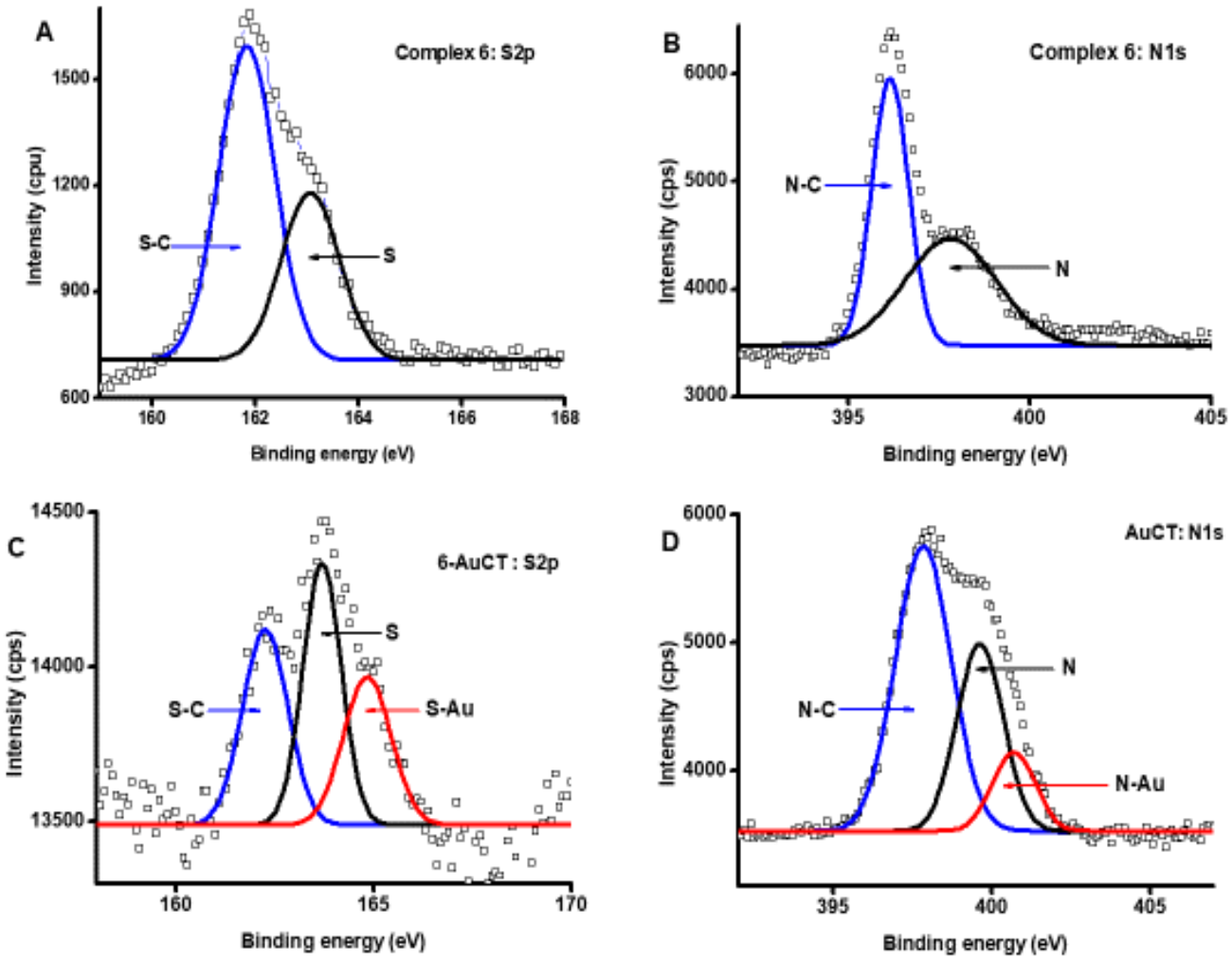

Figure. 3.17: High resolution XPS spectra for (A) complex **6** (S 2p), complex **6** (N1s), **6**-AuCT (S 2p) and AuCT (N 1s).

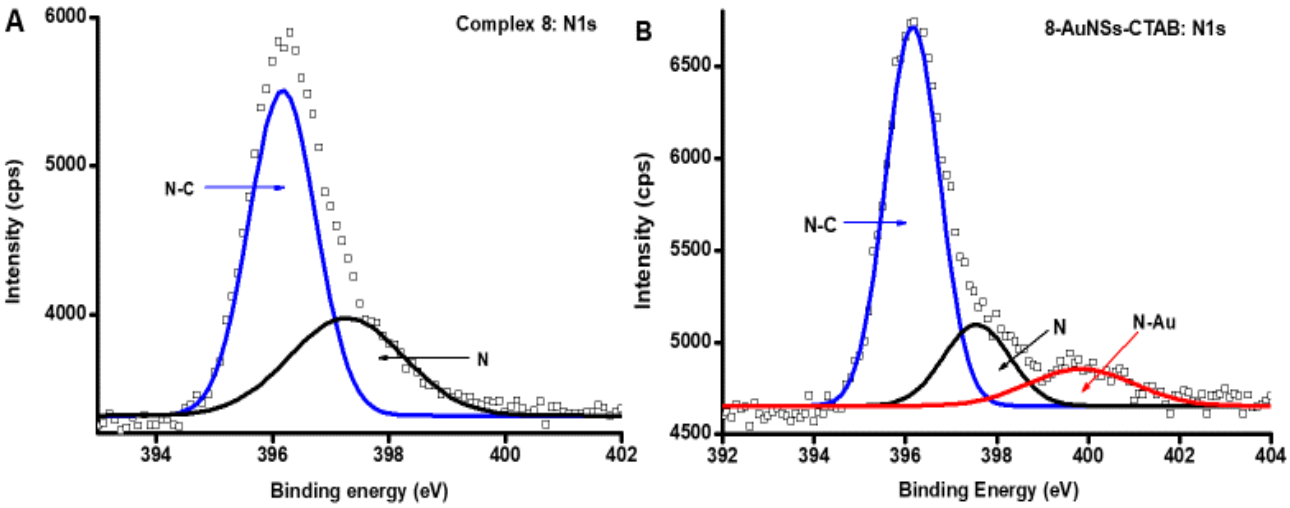

Figure. 3.18: High resolution XPS spectra for (A) complex **8** (N1s), **8**-AuNSs-CTAB (N 1s).

Figure. 3.18 shows high resolution XPS spectra for complex **8** N1s and **3**–AuNSs-CTAB N1s as representatives for conjugates with Au-N and Au-S interactions. The N1s peak for complex **8** alone (**Figure 3.18A**) showed two subpeaks corresponding to –N–C– (396.2eV) and –N– (397.3eV), while the conjugate (**Figure 3.18B**,) displayed three peaks attributed to –N–C– (396.3eV), –N– (397.3eV) and –N–Au– (399.9 eV), confirming a Au-N bond.

It should be noted that some conjugates (**7**-AuNTs-CTAC, **8**-AuNSs-CTAB and **8**-AuNRs-CTAB) displayed the presence of both the gold to sulfur and gold to nitrogen interactions (–N–Au– and –S–Au–) suggesting that both S and N on the same Pc molecule are linked to AuNPs or that some molecules were adsorbed on the surface of metallic nanoparticles through S-Au interactions while others utilized the N-Au interactions since gold has a strong affinity for both sulphur and nitrogen.

The X-ray diffraction pattern of all the conjugates (except **6**-CT) was similar to that of the NPs, with a characteristic powder diffraction pattern of gold and silver (**Figure 3.8,** using **6**-AuNSs-CTAB as a representative for conjugates) as explained before due the presence of the NPs with gold or silver in the conjugates. Broad peaks between 2θ = 15–23°, were observed for Pc complexes alone (**Figure 3.8,** using complex **6** as a representatives for Pcs), typical of the amorphous nature of phthalocyanines [204] and these were also observed in all conjugates, providing evidence for the presence of the phthalocyanines in the conjugates.

The TEM micrographs of the conjugates (**Figure 3.19**, using **4b**-GSS and **7**-AuNTs-CTAC as representative) generally displayed extensive aggregation when compared to NPs alone (**Figure 3.7** insert and **Figure 3.10** insert). Aggregation is possibly due to π-π stacking between the Pcs on adjacent nanoparticles as previously stated.

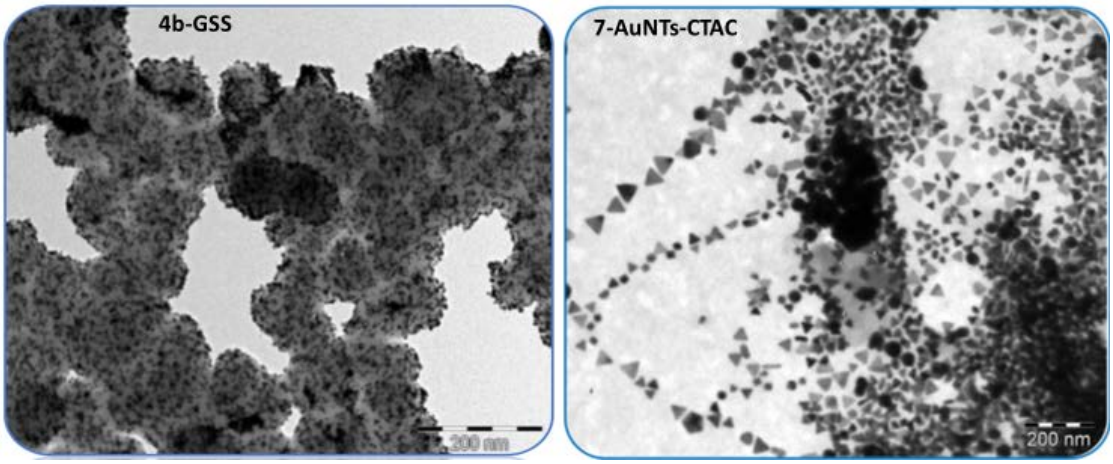

Figure. 3.19: TEM images of **4b**-GSS and **7**-AuNTs-CTAC.

3.3.3. Sizes of NPs and conjugates

The sizes of NPs and their conjugates are as shown in **Table 3.2**. It should be noted that the average size of the NPs of the same shape varies because they were prepared in different batches. The size (and shape) of NPs is greatly affected by many factors including temperature, volume and pH of the solution, pressure, time, synthesis method used, surfactant amount used, exposure to light, concentration of starting material and the stirring rate during synthesis [205–209], hence it is expected that different batches will

differ in size since it difficult to follow the exact steps of the previous protocol due to variations (however slight) in the above stated conditions.

As shown in **Table 3.2**, the sizes of the GSH functionalised alloy NPs are 18.9 nm and 15.1 nm for Ag_1Au_3NSs-GSH and Ag_3Au_1NSs-GSH respectively. The differences in size could be due to differences in the concentration of the gold and silver salt used, in addition to slight differences in the synthesis protocol as explained above.

The large size for the Ag_3Au_1SiNSs-APTES (73 nm) shows that the SiNSs formed a coat on aggregates of Ag_3Au_1NSs-OA/OLA forming large particles. This is confirmed by the TEM image in **Figure 3.9** (insert), showing a dark core with a light ring around it.

The synthesis protocol of AuNTs is very sensitive to temperature, hence the differences in sizes for AuNTs-CTAC (52.7nm and 62.3 nm edge length) are probably due to fluctuations in the room temperature in addition to other conditions as previously explained. The same applies to AuNSs-GSH (13.6 nm, 14.9 nm or 17.7 nm in diameter) and AuNSs-CTAB (11.7, 13.4 nm or 15.2 nm diameter). Only one size was used for AuNTs-GSH (33.2 nm edge length) and AgNSs-GSH (11.1 nm) since these were prepared in one batch.

The large size for the GSS is due to the large SiNSs used as shown by the TEM image in **Figure 3.10** (insert), showing the large SiNSs in grey and small speckles of gold in black. CT is a biopolymer hence it is large as shown by the

DLS size (and the white spheres in **Figure 3.11**, insert), however it should be noted that DLS gives the hydrodynamic diameter hence the sizes are always larger. Generally, all sizes increased following conjugation.

3.3.4. Loading of MPcs to NPs.

The size of an MPc is ~1 nm while that of NPs is usually greater 1 nm. Thus, more than one Pc can bind to NPs, and this is termed loading. The loading of complexes onto the nanoparticles was investigated following literature methods [210]. Briefly this involved comparing the Q band absorbance intensity of the MPc in the conjugate with that of the MPc before conjugation. The representative loading values are shown in **Table 3.2**.

Less loading of MPcs on the AuNTs-CTAC (52.7 nm and 62.3 nm edge lengths) was observed for MPc–AuNTs-CTAC conjugates, unlike AuNSs-CTAB (11.7, 13.4 nm or 15.2 nm diameter) which afforded more loading of MPcs on their surface compared to the former, **Table 3.2**. The same applies to AuNTs-GSH (33.2 nm edge length) compared AuNSs-GSH (13.6 nm, 14.9 nm or 17.7 nm in diameter). This could be due to the plate like nature of these nanotriangles (also termed nanoplates) that tends to stack on each other face-to-face or edge to edge [211] in addition to the larger size as shown by the longer edge length. This reduces the loading capacity of the nanoparticles. The loading capacity is greatly influenced by the nanoparticle surface area [212], which in this case is greatly affected by the particle size and aggregation [213]. Size reduction increases the percentage of atoms at the surface [214], hence more loading.

Conjugates with GSS (78.4 nm and 81.7 nm diameter), displayed the highest loading probably due to the porous nature of silica in GSS which provides more surface area for loading than other NPs.

Thus it can be inferred that the NPs having either small sizes or are porous generally displayed more loading of the Pcs onto their surfaces than those with bigger sizes due to the high surface area which allows for high loading [215].

3.4. Summary of chapter

The synthesis and characterizations of Pcs, NPs and the conjugates were presented in this chapter. The Pcs were characterized using ^{1}H NMR, mass, UV-Vis, FTIR spectroscopies and elemental analysis to confirm the respective substituted Pcs. All the studied complexes **1-8** showed monomeric Q-band in DMSO, however in water (with 1.6% DMSO) there was broadening of the Q band due to aggregation.

UV Vis, X-ray diffractometry, DLS (for CT and AuCT) and TEM were used for the characterisation of NPs. NPs were synthesised in different batches hence there are different sizes for the same shape NPs (AuNSs-CTAB, 11.7 (DLS), 13.4 nm and 15.2 nm in diameter; AuNSs-GSH 13.6 nm, 14.9 nm and 17.7 nm in diameter; AuNTs-CTAC, 52.7 nm and 62.3 nm in edge lengths; AuNTs-GSH, 33.2 nm in edge length and GSS, 78.4 and 81.7 nm in diameter).

The X-ray diffraction pattern of all the conjugates (except **6**-CT, which showed only broad amorphous peaks) was similar to that of the NPs, with a characteristic powder diffraction pattern of gold (or silver) showing the presence of gold or silver in the conjugates. The presence of the amorphous phthalocyanines in the conjugates was shown by broad peaks between 2θ = 15–23°.

FT–IR and X–ray photoelectron spectroscopic techniques were used to confirm the linkage of Pcs to NPs. FTIR confirmed successful formation of the amide bonds and XPS confirmed Au-S/Au-N interactions.

The conjugates to AuNSs generally displayed high loading of the Pcs onto their surfaces than their AuNTs counter parts and this was attributed to the large surface area associated with small particle sizes which allows for high loading. Conjugates to GSS also displayed high loading due to the porous nature of SiNSs in GSS which increases the surface area for loading.

CHAPTER 4

4. Photophysical and Photochemical Properties

The chapter discusses the photophysical and photochemical behaviour; fluorescence quantum yields and life-times, triplet quantum yields and life-times, and singlet oxygen quantum yields of phthalocyanines when alone and when conjugated to nanoparticles.

4.1. Fluorescence spectra, lifetimes and quantum yields

4.1.1. Fluorescence excitation and emission spectra

Figure 4.1 shows an overlay of the absorption, emission and excitation spectra of complex **7** and **7**-AuNTs-CTAC in DMSO as representatives for other complexes and their conjugates. The ground state absorption and excitation spectra are mirror images of the emission spectrum. The closeness of the Q-band absorption and excitation maxima (**Figure 4.1A**) shows that the nuclear configurations of the ground and excited states are similar and are not affected by excitation in DMSO. It also shows that the complexes are not aggregated in DMSO. Similar fluorescence behaviour was observed for all Pc complexes alone. The slight differences between absorbance and excitation wavelengths for some complexes are due to the differences in equipment used, while the differences observed in the conjugates (**Figure 4.1B**) are attributed to the absorbance by the nanoparticles in the conjugate.

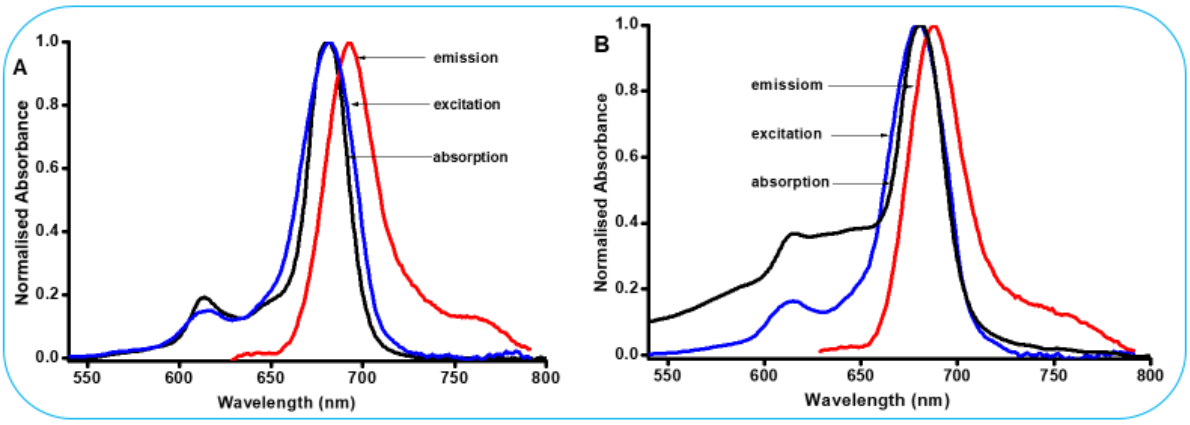

Figure 4.1: Absorption (black), excitation (blue) and emission (red) spectra of complex **7** (A) and **7**-AuNTs-CTAC (B) in DMSO as a solvent.

4.1.2. Fluorescence quantum yields (Φ_F) and lifetimes (τ_F)

The fluorescence quantum yields (Φ_F) were determined by a comparative method [163,164] and calculated according to Equation 1.1, using unsubstituted ZnPc in DMSO (Φ_F = 0.2) [46] as a standard. The fluorescence lifetimes (τ_F) were obtained using the time correlated single photon counting (TCSPC) method. **Table 4.1** shows the Φ_F and τ_F values of the complexes and their respective conjugates in DMSO. The Φ_F values in water with 1.6% DMSO were <0.01 probably due to aggregation, thus were not shown in **Table 4.1**.

The fluorescence decay curve for **4a**-AuNTs-CTAC is shown as an example in **Figure 4.2**, and this is used as a representative for all the Pcs and their conjugates.

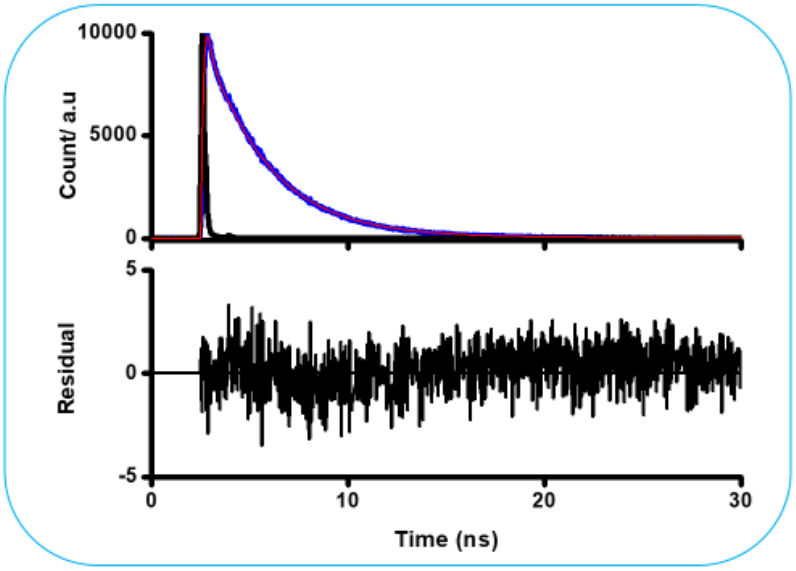

Figure 4.2: Fluorescence decay (blue), x^2 fitting (red) and IRF (black) curves for **4a**-AuNTs-CTAC in DMSO.

Table 4.1: Fluorescence quantum yield and lifetime parameters of the Pcs and the respective conjugates in DMSO.

Sample	Φ_F **(±0.01)**	$\tau_{F(ns)}$ **(%) (±0.01)**	**Mean** τ_F **(ns)**	τ_0 **(ns)**	[a]**Size of NPs alone (nm)**	**Loading (µg/mg)**
Complex 1	0.02	2.43 (100)	2.43	121.5		
1-Ag_1Au_3NSs-GSH	< 0.01	0.32 (51) 3.26 (49)	1.75	-	18.9 XRD	[c]
1-Ag_3Au_1NSs-GSH	< 0.01	0.34 (78) 3.27 (22)	0.98	-	15.1 XRD	[c]
1-Ag_3Au_1SiNSs-APTES	0.01	0.31 (81) 5.15 (19)	1.25	125.0	73	19
Complex 2	0.19	3.36 (100)	3.36	17.7		
2-AuNTs-GSH	0.13	3.05 (100)	3.05	23.5	33.2	22
2-AuNSs-GSH	0.03	2.88 (98) 2.38 (2)	2.87	95.7	13.6	27
2-AgNSs -GSH	0.11	2.95 (100)	2.95	26.8	11.1	9
2-Ag_3Au_1NSs-GSH	0.04	2.90 (96.8) 1.96 (3.2)	2.87	71.8	15.1	41
Complex 3a	0.17	3.08 (100)	3.08	18.1		
3a-AuNTs-CTAC	0.16	2.90 (96.7) 1.99 (3.3)	2.87	17.9	52.7	15
3a-AuNSs-CTAB	0.14	2.71 (89.1) 1.98 (10.9)	2.63	18.8	15.2	22
3a-GSS	0.13	2.81 (97.6) 1.98 (2.4)	2.79	21.4	81.7	50
Complex 3b	0.03	0.78 (100)	0.78	26.0		
3b-AuNTs-CTAC	<0.01	0.66 (72) 0.37 (28)	0.58	-	52.7	20
3b-AuNSs-CTAB	<0.01	0.58 (65) 0.32 (35)	0.49	-	15.2	32
3b-GSS	0.01	0.73 (82.1) 0.40 (17.9)	0.67	67.0	81.7	48
Complex 4a	0.15	3.12 (100)	3.12	20.8		
4a-AuNTs-CTAC	0.12	3.00 (98.7) 1.46 (1.3)	2.98	24.8	52.7	24
4a-AuNSs-CTAB	0.08	2.88 (89.3) 3.25 (10.7)	2.92	36.5	15.2	37
4a-GSS	0.10	3.03 (100)	3.03	30.3	78.4	51
Complex 4b	0.02	0.88 (100)	0.88	44.0		
4b-AuNTs-CTAC	<0.01	0.75 (80.9) 0.44 (19.1)	0.69	-	52.7	17
4b-AuNSs-CTAB	<0.01	0.66 (81) 0.08 (19)	0.55	-	15.2	29
4b-GSS	0.01	0.69 (74) 1.23 (26)	0.83	83.0	78.4	49

Complex 5	0.18	3.21 (100)	3.21	17.8		
5-AuNTs-GSH	0.06	3.09 (100)	3.09	51.5	33.2	16
5-AuNSs-GSH	0.02	2.99 (98.5) 0.23 (1.5)	2.98	149.0	13.6	20
5-AgNSs-GSH	0.16	3.10 (100)	3.10	19.4	11.1	10
5-Ag_3Au_1NSs-GSH	0.13	3.17 (100)	3.17	24.4	15.1	28
Complex 6	0.15	2.86 (100)	2.86	19.1		
6-AuNTs-GSH	0.08	2.32 (97.4) 1.55 (2.6)	2.30	28.8	33.2	30
6-AuNSs-GSH	0.06	2.22 (98.9) 4.04 (1.1)	2.24	37.3	17.7	37
6-AuNTs-CTAC	0.12	3.05 (100)	3.05	25.4	62.3	42
6-AuNSs-CTAB	0.11	2.46 (100)	2.46	22.4	11.7 DLS	37
6-AuCT	0.12	2.72 (98.3) 0.96 (1.7)	2.69	22.4	345 DLS	32
6-CT	0.14	2.84 (100)	2.84	20.3	324 DLS	28
Complex 7	0.13	3.04 (100)	3.04	23.4		
7-AuNTs-GSH	0.10	2.82 (95.4) 2.17 (4.6)	2.79	27.9	33.2	26
7-AuNSs-GSH	0.06	2.51 (100)	2.51	41.8	14.9	38
7-AuNTs-CTAC	0.11	2.82 (97.7) 3.25 (2.3)	2.83	25.7	62.3	33
Complex 8	0.15	2.95 (100)	2.95	19.6		
8-AuNSs-CTAB	0.12	2.89 (95.9) 0.94 (4.1)	2.81	23.42	13.4	8
8-AuNRs-CTAB	0.11	<0.01	<0.01	-	2.1	14

Note: Size of the NPs of the same shape varies because they were prepared in different batches. [a]Sizes are from TEM unless otherwise stated. [c]Loading not determined due to unavailability of the sample.

The Pc complexes showed a mono-exponential fluorescence decay as expected [216] while the corresponding conjugates displayed bi-exponential decays, and hence there are two lifetime values for the conjugates. Only the average lifetimes for the conjugates are presented in **Table 4.1**.

The bi-exponential lifetimes observed for the conjugates, could be associated with the monomeric non-interacting MPc molecules, and the interaction between the MPc framework and the nanoparticles, resulting in unquenched and quenched photo-excited singlet states, respectively [217]. Different orientations of the phthalocyanines on the NPs could be responsible for the two lifetimes [218].

Metal centres [41,42], substituents [45,46] and symmetry [32,33] of Pcs together with the shape and size of the linked nanoparticles [219], influence the fluorescence lifetime and quantum yield of complexes.

i) Effect of central metal

Complexes **3a** and **3b**, have a similar macrocycle and ring substituents but differ in the central metal, and this is the same for complexes **4a** and **4b.** Complexes **3b** (Φ_F = 0.03) and **4b** (Φ_F =0.02), containing indium as the central metal, displayed lower fluorescence quantum yields than their zinc counterparts (complex **3a** (Φ_F = 0.17) and **3b** (Φ_F = 0.15)). This shows that indium quenches the fluorescence lifetime and lowers the fluorescence quantum yield of Pcs more than zinc, **Table 4.1**. This is because indium is a heavier atom than zinc since heavy atoms are known to encourage

intersystem crossing to the triplet state through spin orbit coupling. A further decrease in the fluorescence quantum yields of complexes was observed on conjugation to NPs, and this was attributed to the presence of gold, another heavy atom in the NPs.

The fluorescence lifetimes decreased for Pc complexes **3a**, **3b, 4a** and **4b** in the presence of NPs, corresponding to a decrease in the fluorescence quantum yield.

ii) Effect of nanoparticle shape and size

The shape and size of the nanoparticles seems to influence the fluorescence behaviour of dyes. In all cases were the Φ_F was significant (> 0.01), the conjugates to nanospheres displayed low Φ_F compared to their nanotriangle counterparts. This may be attributed to the smaller size of the AuNSs compared to AuNTs, since smaller NPs have been shown to exhibit a greater fluorescence quenching effect [219]. Additionally, nanospheres resulted in more loading of complexes than nanotriangles, **Table 4.1**, and this could result in more aggregation. Aggregates are known to convert electronic excitation energy to vibrational energy which consequently decreases the fluorescence quantum yield of molecules [220].

The behaviour is different when complexes **3a** and **4a** are linked to GSS. Though GSS has the largest size (78.4 and 81.7 nm; **Table 4.1**), the conjugate **3a**-GSS (Φ_F = 0.13) displayed lower Φ_F values than **3a**-AuNTs-CTAC (52.7 nm; Φ_F = 0.16) and this was attributed to high Pc loading in **3a**-GSS as shown in

Table 4.1, hence aggregation in **3a**-GSS. Similarly, the conjugate **4a**-GSS (Φ_F = 0.10) displayed lower Φ_F values than **4a**-AuNTs-CTAC (Φ_F = 0.12). For **3b** and **4b**, the Φ_F values were too low to be compared.

iii) Effect of substituents.

Complexes **2**, **3a** and **4a** are symmetric and have zinc as a central metal, however they differ in their substituents. **3a** (Φ_F = 0.17) has a phenoxy benzothiazole group, complex **2** (Φ_F = 0.19) has a phenoxy propionic acid group and complex **4a** has a thiophine ethoxy group (**Table 1.1**). The low Φ_F for complex **4a** suggest that the thiophine ethoxy group quenches fluorescence more than the phenoxy benzothiazole and phenoxy propionic acid groups, even though the differences in Φ_F are small.

Complexes **1, 3b** and **4b**, are symmetrical Pcs with indium as a central metal in the cavity. However, these complexes have different ring substituents but there was insignificant difference in their Φ_F values (0.02, 0.03 and 0.02 respectively). The low Φ_F values are due to the heavy atom effect of indium as previously explained.

Complexes **7** and **8** are asymmetrical Pcs with one common ring substituent (a phenoxy benzothiazole group) as shown in **Table 1.1**. The complexes displayed Φ_F of 0.13 and 0.15, respectively showing that the phenoxy propanoic acid group quenches fluorescence more than the di-*O*-

isopropylidene-α-D-glucopyranose moiety, probably due to the presence of extra phenyl rings in complex **7** which are reported to contribute to effective population of the triplet state [48], hence lowering fluorescence.

It is expected that Φ_F and τ_F decrease in unison, however in some cases there was a significant decrease in Φ_F compared to τ_F. Following the kinetic model, the excited state lifetimes are directly related to the radiative lifetime (τ_0) hence these were determined using the measured fluorescence quantum yield (Φ_F) and lifetime (τ_F) as shown in equation 4.1 [221,222].

$$\tau_0 = \frac{\tau_F}{\Phi_F} \qquad (4.1)$$

With this model, increase in radiative lifetime will result in a corresponding increase in fluorescence lifetime and a decrease in fluorescence quantum yield. This suggests that a decrease in fluorescence quantum yield can be significantly higher than the corresponding fluorescence lifetime. Indeed, all the complexes and the corresponding conjugates having high radiative lifetime showed lower fluorescence quantum yield (**Table 4.1**) in accordance with the model.

iv) Effect of symmetry

Asymmetry introduces distortions on the phthalocyanine macrocycle which affects their photophysical properties [32,33]. The effect of the number of propanoic acid groups on the fluorescence quantum yields and lifetimes was studied by comparing complexes **2** (with four phenoxy propanoic acid groups)

and **5** (with one phenoxy propanoic acid moiety). There was insignificant difference in the fluorescence quantum yields of the low symmetry complex **5** (Φ_F = 0.18) and the symmetrical complex **2** (Φ_F =0.19) when alone.

The effect of the number of benzothiazole phenoxy groups on the fluorescence quantum yields and lifetimes was studied using complexes **3a** (with four benzothiazole phenoxy groups), **6** (with three benzothiazole phenoxy groups and one phenoxy propanoic acid group) and **7** (with one benzothiazole phenoxy group and three phenoxy propanoic acid groups). The asymmetric complex **6** showed a lower fluorescence quantum yield of 0.15 as well as a shorter lifetime of 2.86 ns compared to the quantum yield of 0.17 and lifetime of 3.08 ns for the symmetrical complex **3a**. Similarly, the asymmetrical complex **7** showed a lower fluorescence quantum yield of 0.13 and a shorter lifetime of 3.04 ns compared to the symmetric complex **3a**. This suggests that the asymmetric molecular structures could be potential means of enhancing intersystem crossing to the triplet state, hence reducing fluorescence.

Further deactivation of the excited singlet state was observed after the conjugation of the complexes to metallic NPs, due to the heavy atom effect from Au [44]. The fluorescence lifetimes also decreased upon conjugation with NPs since fluorescence quantum yields and lifetimes have a direct relationship, except for **6**-AuNTs-CTAC with increased lifetimes after conjugation, due to a high radiative lifetime (**Table 4.1**) compared to complex **6** alone as previously explained.

4.2. Triplet state quantum yield (Φ_T) and lifetime (τ_T)

The triplet state quantum yield (Φ_T) represents the fraction of molecules that undergoes intersystem crossing to the excited triplet state. A high triplet state quantum yield corresponds to low fluorescence quantum yield suggesting high efficiency of intersystem crossing, which is an attractive feature for MPcs intended for PDT as photosensitizers. A high triplet quantum yield is of great importance since it influences the singlet oxygen production.

The Φ_T and τ_T values were measured by laser flash photolysis system in argon saturated solutions of the complexes or their conjugates in DMSO. The triplet quantum yield in aqueous media could not be obtained due to the plausible aggregation of Pcs, since aggregation is known to deactivate the photoactivity of molecules [223]. **Figure 4.3B**, shows the triplet decay curve of the conjugate **3**-AuNTs-CTAC in DMSO (as a representative) together with its transient curve (**Figure 4.3A**).

The transient absorption spectrum shows a broad band between 400–600 nm with a maximum absorption at 500 nm, attributed to the excited triplet-triplet state absorption ($T_1 \rightarrow T_n$). The negative peaks were also shown between 325 and 380 nm, and between 600 and 700 nm. Considering the shape and the position of the negative signals, which corresponds to the absorption in the ground state, these can be attributed to the depletion or photobleaching of the phthalocyanine ground state [224].

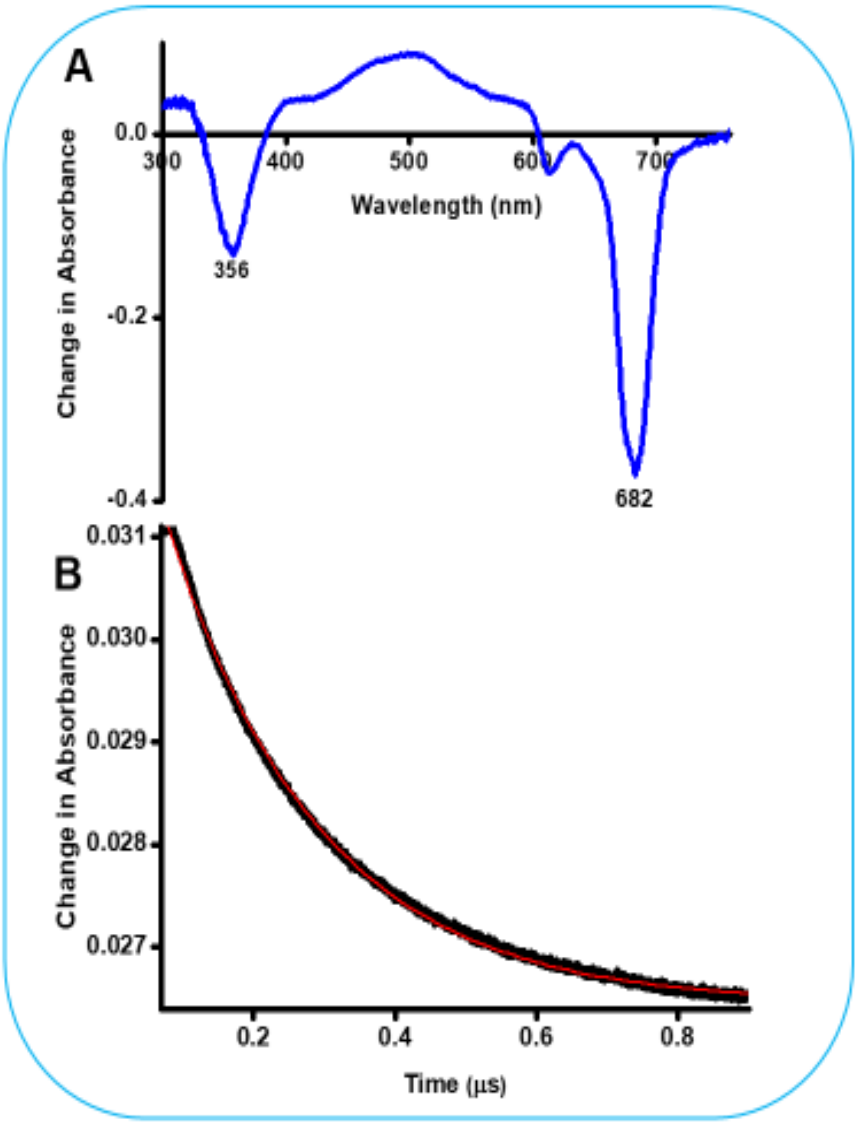

Figure 4.3: (A) Transient curve and (B) Triplet absorption decay curve (black) and fitting (red) for **4a**-AuNSs-CTAB in DMSO.

The triplet decay curve obeyed second order kinetics, typical of MPc complexes at high concentration, due to triplet-triplet recombination [225]. Fitting the decay curve at the absorption maximum produced the triplet lifetimes and the obtained values together with the triplet quantum yield are summarized in **Table 4.2**.

Table 4.2: Triplet quantum yield and lifetime parameters of the Pcs and respective conjugates

Sample	Φ_T **(±0.01)**	τ_T **(μs) (±1)**	Φ_F **(±0.01)**
Complex 1	0.65	58	0.02
1-Ag_1Au_3NSs-GSH	0.79	73	< 0.01
1-Ag_3Au_1NSs-GSH	0.73	58	< 0.01
1-Ag_3Au_1SiNSs-APTES	0.55	81	0.01
Complex 2	0.54	264	0.19
2-AuNTs-GSH	0.68	244	0.13
2-AuNSs-GSH	0.70	305	0.03
2-AgNSs -GSH	0.67	271	0.11
2-Ag_3Au_1NSs-GSH	0.69	314	0.04
Complex 3a	0.56	149	0.17
3a-AuNTs-CTAC	0.62	199	0.16
3a-AuNSs-CTAB	0.68	188	0.14
3a-GSS	0.68	132	0.13
Complex 3b	0.75	55	0.03
3b-AuNTs-CTAC	0.81	72	<0.01
3b-AuNSs-CTAB	0.86	67	<0.01
3b-GSS	0.82	48	0.01
Complex 4a	0.47	306	0.15
4a-AuNTs-CTAC	0.53	214	0.12
4a-AuNSs-CTAB	0.61	202	0.08
4a-GSS	0.64	242	0.10
Complex 4b	0.60	225	0.02
4b-AuNTs-CTAC	0.64	86	<0.01
4b-AuNSs-CTAB	0.70	78	<0.01
4b-GSS	0.72	49	0.01
Complex 5	0.73	233	0.18
5-AuNTs-GSH	0.80	247	0.06
5-AuNSs-GSH	0.87	262	0.02
5-AgNSs-GSH	0.82	274	0.16
5-Ag_3Au_1NSs-GSH	0.81	290	0.13
Complex 6	0.73	238	0.15
6-AuNTs-GSH	0.83	229	0.08
6-AuNSs-GSH	0.90	216	0.06

6-AuNTs-CTAC	0.86	180	0.12
6-AuNSs-CTAB	0.89	227	0.11
6-AuCT	0.81	231	0.12
6-CT	0.74	239	0.14
Complex 7	0.76	237	0.13
7-AuNTs-GSH	0.85	232	0.10
7-AuNSs-GSH	0.89	199	0.06
7-AuNTs-CTAC	0.82	124	0.11
Complex 8	0.51	308	0.15
8-AuNSs-CTAB	0.62	318	0.12
8-AuNRs-CTAB	0.71	210	0.11

The heavy atom effect of gold and silver was shown by the enhanced Φ_T on linkage of Pc complexes to NPs. This applies to all cases in **Table 4.2**, where the Φ_T increases for the NP-Pc conjugates. As expected high Φ_T values were accompanied by short τ_T [226], and in most cases where there is lengthening of τ_T with increase in Φ_T, it could be due to the protection of the Pc complexes by the NPs, since the NPs are much larger than the Pcs at ~1 nm [227,228].

Intrinsic factors such as central metal, ring substituents and nature of symmetry [32,33,41,42,45,46] of Pc complexes coupled with the nature of the nanoparticles forming conjugates with Pcs [219], have an influence on their triplet lifetime and quantum yield, hence their effects will be discussed in the following subsections.

i) Effect of central metal

The Pc complexes displayed high triplet quantum yields (Φ_T = 0.56 for **3a** and 0.75 for **3b**; Φ_T = 0.47 for **4a** and 0.60 for **4b**), (**Table 4.2**) corresponding to their low Φ_F, due to the presence of heavy atoms, Zn and In, as previously explained. The triplet lifetimes became shorter as the triplet quantum yields increased as expected [226], except for **3a**-AuNTs-CTAC, **3a**-AuNSs-CTAB , **3b**-AuNTs-CTAC, **3b**-AuNSs-CTAB due reasons explained above.

ii) Effect of nanoparticle shape and size

As shown in **Table 4.2**, the shape and size of the nanoparticles influences the triplet behaviour of conjugates. In all cases the Φ_T of conjugates to AuNSs is greater than that of AuNTs, corresponding to lower Φ_F for the former since the two are competing processes.

The conjugates to GSS (**4a**-GSS and **4b**-GSS) displayed higher Φ_T values (**Table 4.2**) than AuNTs-CTAC and AuNSs-CTAB conjugates regardless of their large size due to the high loading capacity of GSS as explained before.

iii) Effect of substituents.

Symmetric complexes **2** (Φ_T = 0.54) and **3a** (Φ_T = 0.56) showed higher Φ_T values compared to **4a** (Φ_T = 0.47), probably due to the advantage of an extra phenyl rings in complexes **2** and **3a**, as explained before [48]. When comparing **2** and **3a**, the former displayed slightly lower Φ_T than the latter, corresponding to a higher Φ_F for the former.

The MPcs with the benzothiazole phenoxy groups (complexes **3a** and **3b)**, together with their conjugates displayed high Φ_T compared to the corresponding thiophene ethoxy counterparts (complexes **4a** and **4b**) as shown in **Table 4.2**, suggesting that the former promotes intersystem

crossing to the triplet state more than the latter both in the presence and absence of NPs.

The asymmetrical complex **7**, displayed higher Φ_T values than complex **8** corresponding to its low Φ_F, probably due to the presence of extra phenyl rings in complex **7** which are reported to contribute to effective population of the triplet state [48].

iv) Effect of symmetry

The low symmetry complex **5** (with one phenoxy propanoic acid group) showed higher triplet quantum yield than the symmetrical complex **2** (four phenoxy propanoic acid groups), which is in agreement with the literature that low symmetrical phthalocyanines possess better triplet state behaviour than their corresponding symmetrical analogues [32,33,229]. As stated above, the enhancement of the triplet quantum yield upon conjugation to NPs could be attributed to the promotion of intersystem crossing to the triplet state due to the heavy atom effect of gold and silver in the nanoparticles.

Conjugates containing Au (a heavier atom than Ag), as expected have larger Φ_T values compared to the Ag counterparts. The **5-**Ag_3Au_1NSs-GSH gave a lower Φ_T when compared to **5**-AuNSs-GSH but was similar to **5**-AgNSs-GSH. For **2**-AuNSs-GSH, **2**-AgNSs-GSH and **2-**Ag_3Au_1NSs-GSH, there were only slight differences in Φ_T values (**Table 4.2**). It is also possible that the Pc loading on the NPs affected their excited state parameters. Ag_3Au_1NSs

conjugates with the larger loading gave lower Φ_T values than AgNSs conjugates with the lower loading (**Table 4.1**), probably due to aggregation in the former, which result in quenching of the triplet state.

The symmetric complex **3a** (with four benzothiazole phenoxy groups) displayed low Φ_T values (**Table 4.2**) compared to asymmetric complexes **6** (with three benzothiazole phenoxy groups and one phenoxy propanoic acid group) and **7** (with one benzothiazole phenoxy group and three phenoxy propanoic acid groups) as expected for asymmetric Pcs [32,33,229]. Even though the benzothiazole group seemed to promote intersystem crossing to the triplet state more than the phenoxy propanoic acid group when symmetric complexes **2** and **3a** are compared, the opposite was observed for asymmetrical complexes **6** and **7**. Complex **6**, with more benzothiazole groups displayed slightly lower Φ_T when compared to complex **7**, with more propanoic acid groups, suggesting that the propanoic acid group in an asymmetrical environment promotes intersystem crossing to the triplet state more than the benzothiazole group. The effect of the propanoic acid group was further displayed by the higher Φ_T values of complex **7** compared to complex **5**, with only one propanoic acid group.

There was insignificant difference between the Φ_T of complex **6** (Φ_T = 0.73) and its chitosan (CT) conjugate (**6**-CT Φ_T = 0.74) showing that CT has no effects on the photophysical properties of MPcs.

v) Effect of alloy NPs on complex 1, 2 and 5

The conjugates **1**-Ag_3Au_1NSs-GSH, **1**-Ag_1Au_3NSs-GSH, **2**-Ag_3Au_1NSs-GSH and **2**-Ag_3Au_1NSs-GSH showed increased Φ_T values in comparison to their respective Pc complexes alone (**Table 4.2**). As earlier stated, spin orbit coupling contribution from the heavy atoms in the NPs could be responsible for the marked increase in the Φ_T values of the conjugates as compared to their respective Pc complexes alone [44]. **1**-Ag_1Au_3NSs-GSH containing more Au (a heavier atom than Ag), has a larger Φ_T value compared to **1**-Ag_3Au_1NSs-GSH with less Au. The lengthening of lifetimes for complex **1** in the presence of Ag_1Au_3NSs-GSH, and complexes **2** and **5** in the presence of Ag_3Au_1NSs-GSH, may be due to the protection of the Pc complexes by the NPs. There was however, no change in lifetime for complex **1** in the presence of Ag_3Au_1NSs-GSH. It is possible that the larger Ag_1Au_3NSs-GSH (18.9 nm) protected complex **1** more effectively than the smaller Ag_3Au_1NSs-GSH (15.1 nm). For **1**-Ag_3Au_1SiNSs–APTES, a decrease in Φ_T is observed when compared to complex **1** alone. A decrease in Φ_T values when Pcs are covalently linked to SiNSs has been reported before [230], and is possibly due to Pcs interlinking with the SiNSs, resulting in the quenching of the excited states. The Φ_T value for **1**-Ag_3Au_1SiNSs–APTES, is however still reasonably high at 0.55 allowing for the conjugate to still be used for photosensitization. **1**-Ag_3Au_1SiNSs–APTES has a longer lifetime, corresponding to a decreased Φ_T.

4.3. Singlet oxygen quantum yields

A good photosensitizer should have high triplet and singlet oxygen quantum yields [231]. Production of singlet oxygen is dependent on the triplet state population and the effectiveness of energy transfer process between the excited triplet state of the photosensitizer and ground state molecular oxygen [203,232]. To determine the singlet oxygen quantum yield (Φ_{Δ}), the chemical photodegradation of singlet oxygen quenchers (DPBF in DMSO and ADMA in aqueous media) in the presence of an MPc were monitored over a period of time.

As shown in **Figure 4.4** (using complexes **7** and **3a** as representatives in DMSO and water with 1.6% DMSO, respectively), the Q-band of the complexes and their conjugates remained unchanged, proving their stability over the irradiation period, while DPBF and ADMA degraded. In the absence of the Pc complexes DPBF and ADMA bands remain unchanged. The Φ_{Δ} values are presented in **Table 4.3**.

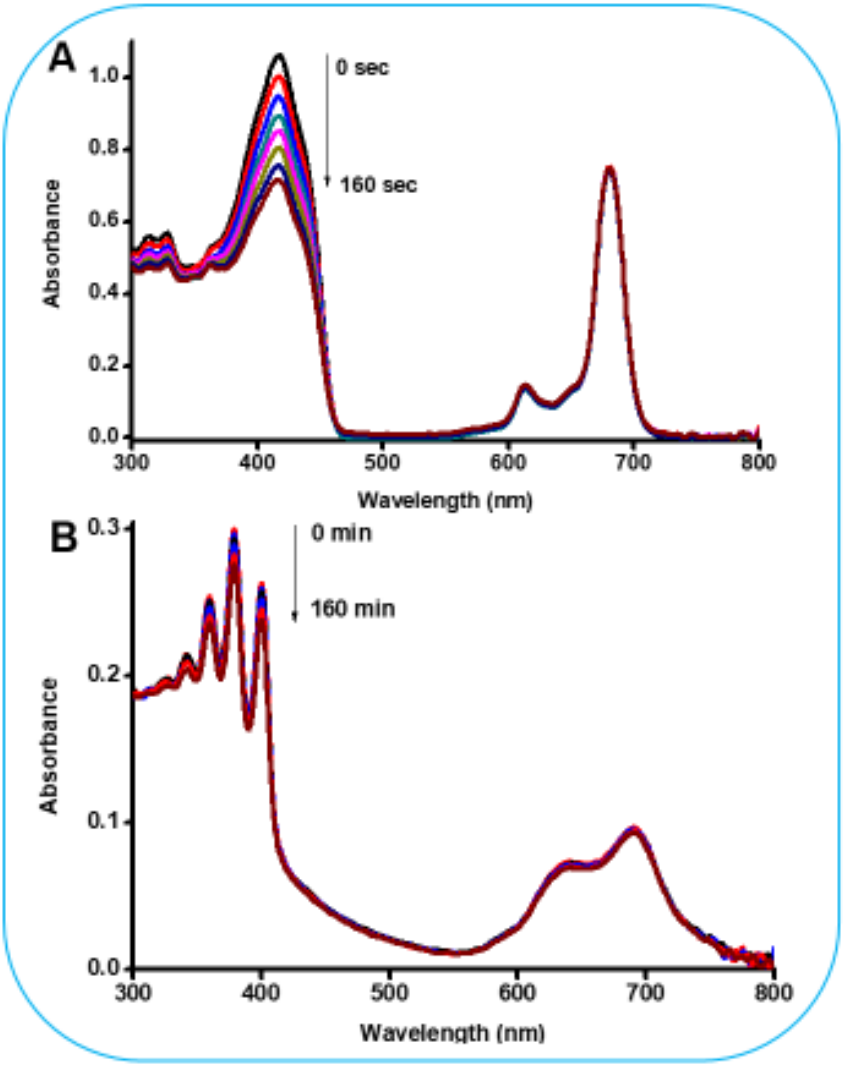

Figure 4.4: Representative spectra for singlet oxygen quantum yield determination using a photochemical method. The spectra show the degradation of (A) DPBF in DMSO and (B) ADMA in water with 1.6% DMSO in the presence of complexes **7** and **3a** respectively.

Table 4.3: The singlet oxygen quantum yield of the Pcs and respective conjugates in DMSO (and water with 1.6% DMSO in brackets).

Pc	**Φ_T (±0.01)**	**Φ_Δ (±0.01) in DMSO**	**Φ_Δ (±0.01) in water with 1.6% DMSO**
Complex 1	0.65	0.37	0.16
1-Ag_1Au_3NSs-GSH	0.79	0.27	0.11
1-Ag_3Au_1NSs-GSH	0.73	0.25	0.10
1-Ag_3Au_1SiNSs- APTES	0.55	0.49	0.15
Complex 2	0.54	0.47	0.07
2-AuNTs-GSH	0.68	0.59	0.14
2-AuNSs-GSH	0.70	0.58	0.15
2-AgNSs -GSH	0.67	0.54	0.04
2-Ag_3Au_1NSs-GSH	0.69	0.39	0.08
Complex 3a	0.59	0.50	0.07
3a-AuNTs-CTAC	0.62	0.53	0.08
3a-AuNSs-CTAB	0.68	0.56	0.10
3a-GSS	0.68	0.59	0.11
Complex 3b	0.75	0.64	0.12
3b-AuNTs-CTAC	0.81	0.69	0.13
3b-AuNSs-CTAB	0.86	0.74	0.15
3b-GSS	0.82	0.72	0.16
Complex 4a	0.47	0.33	0.07
4a-AuNTs-CTAC	0.53	0.39	0.07
4a-AuNSs-CTAB	0.61	0.46	0.08
4a-GSS	0.64	0.54	0.10
Complex 4b	0.60	0.42	0.08
4b-AuNTs-CTAC	0.64	0.52	0.09
4b-AuNSs-CTAB	0.70	0.60	0.11
4b-GSS	0.72	0.67	0.13
Complex 5	0.73	0.55	0.12
5-AuNTs-GSH	0.80	0.69	0.17
5-AuNSs-GSH	0.87	0.72	0.23
5-AgNSs-GSH	0.82	0.69	0.05
5-Ag_3Au_1NSs-GSH	0.81	0.46	0.11
Complex 6	0.73	0.69	0.15

6-AuNTs-GSH	0.83	0.75	0.20
6-AuNSs-GSH	0.90	0.79	0.22
6-AuNTs-CTAC	0.86	0.78	0.19
6-AuNSs-CTAB	0.89	0.80	0.26
6-AuCT	0.81	0.75	0.21
6-CT	0.74	0.71	0.13
Complex 7	0.76	0.69	0.14
7-AuNTs-GSH	0.85	0.77	0.19
7-AuNSs-GSH	0.89	0.79	0.21
7-AuNTs-CTAC	0.82	0.75	0.16
Complex 8	0.51	0.36	0.08
8-AuNSs-CTAB	0.62	0.55	0.16
8-AuNRs-CTAB	0.71	0.61	0.20

As shown in **Table 4.3**, the Φ_Δ followed the same trend observed in Φ_T since the Φ_Δ value is dependent on the Φ_T parameter, as previously stated except for the conjugates, **1**–Ag_3Au_1NSs–GSH, **1**–Ag_1Au_3NSs–GSH, **2**-Ag_3Au_1NSs–GSH and **5**-Ag_3Au_1NSs–GSH which displayed increased triplet quantum yields, but afforded lower singlet oxygen quantum yield than their respective complexes alone. The lower singlet oxygen quantum yield could probably be due to the screening effect caused by the capping ligand around the surface of the NPs, which could have prevented the interaction of the excited triplet state of the conjugates and the ground state molecular oxygen [232–234].

The higher singlet oxygen quantum yield for **1**–Ag_3Au_1SiNSs–APTES compared to complex **1** alone, could probably be due to the permeability of the porous silica matrix to ground state molecular oxygen [198,235]. Hence linking phthalocyanines to Ag_3Au_1NSs contained within a SiNSs matrix could be advantageous for production of singlet oxygen which is essential for application in areas such as PDT.

The aqueous media is important for biological applications, hence the Φ_Δ values were also measured in water with 1.6% DMSO since the Pc complexes and some conjugates are not soluble in water (1.6% DMSO was also used for PDT applications in **Chapter 5**). The Φ_Δ in water (with 1.6% DMSO) were lower than in DMSO (**Table 4.3**). The low Φ_Δ values in water are due to quenching [46] and low solubility of oxygen in water [236] . Even though the values of Φ_Δ in water (with 1.6% DMSO) are low, the samples can still be used for PDT since complexes such as lutetium texaphyrin with a low singlet oxygen

quantum yield value of 0.11 have been employed for clinical application in PDT [4].

4.4. Summary of chapter

The photophysical and photochemical properties of the complexes and their conjugates were studied in solution. All the studied complexes showed good photophysicochemical behaviour with relatively high triplet and singlet quantum yields. These generally increased on linkage to NPs due to the heavy–atom effect of gold and silver in NPs, except for the conjugates to complex **1**, probably due to poor interaction of the excited state of the conjugates and molecular oxygen.

AuNSs-CTAB conjugates yielded higher Φ_T and Φ_Δ values than AuNTs-CTAC due to the higher loading by AuNSs-CTAB probably caused by their small size compared to AuNTs-CTAC. However, GSS, with the largest NP size displayed the highest Φ_Δ values compared to the AuNTs-CTAC counterparts and this was attributed to high loading probably encouraged by its porous nature.

The complexes with a heavier central metal (indium) exhibited higher triplet and singlet quantum yields in comparison to its zinc counterparts (which is a relatively light metal) and this could be due to the heavy–atom effect obtained from the former. Asymmetrical complexes displayed relatively higher triplet and singlet quantum yields than symmetrical complexes, with complexes containing phenoxy benzothiazole and phenoxy propionic acid groups showing improved quantum yields than their thiophene ethoxy counterparts.

It is pertinent to note that improved Φ_T and Φ_Δ of complexes in the presence of the NPs could afford efficacious photosensitization which is pivotal for PDT in the treatment of cancer.

CHAPTER 5

5. *In-vitro* dark cytotoxicity and photodynamic therapy of cancer

This chapter discusses the *in-vitro* dark cytotoxicity and photodynamic therapy activity of phthalocyanines when alone and when conjugated to nanoparticles against epithelial breast cancer cell lines (MCF-7).

In vitro dark cytotoxicity and photodynamic therapy of the complexes and their conjugates were tested against MCF-7 cells using **3b** (Φ_Δ = 0.12), **3b**-GSS (Φ_Δ = 0.16), **6** (Φ_Δ = 0.15), **6**-AuCT (Φ_Δ = 0.21), **8** (Φ_Δ = 0.08), **8**-AuNRs-CTAB (Φ_Δ = 0.20) and **8**-AuNSs-CTAB (Φ_Δ = 0.16) as examples (and Φ_Δ values in water containing 1.6% DMSO are shown in brackets). The dark cytotoxicity studies were used to evaluate the degree to which the photosensitizer (PS) can exert cytocidal activity at varied concentration doses in the absence of illumination. Cytotoxicity studies performed in the dark are referred to as *in vitro* dark cytotoxicity. *In vitro* dark cytotoxicity is undesirable for PS aimed for use in PDT applications as it results in cytocidal activity against both healthy and tumorigenic cells. The lower the cell viability, the higher the dark cytotoxicity.

The stock concentration of all the complexes and their conjugates were prepared by dissolving each in DMSO (with an addition of 1% acetic acid for **3**-AuCT) and making the volume up with supplemented media. As a result, the vehicle control consisting of 1.6% DMSO (with additional 1% acetic acid for studies with **3**-AuCT since chitosan dissolves in water with 1% acetic acid) in culture media (being the highest concentration of DMSO used for all photosensitizers used in this study) was equally tested against MCF-7 cells to assess the effects of the solvent against the cells. The percentage cell viability of the 1.6% DMSO was relatively the same as the media control alone (**Figures 5.1** and **5.2**, 0 μg/mL). A fixed light dosimetry of 170 J.cm^2 was used for all PDT studies.

5.1. Complex 3b and 3b-GSS

Gradient PS concentration range of 10 μg/mL–160 μg/mL for *in vitro* dark cytotoxicity and PDT were used.

5.1.1. In vitro Dark Cytotoxicity

Complex **3b** and **3b**-GSS (**Figure 5.1**), exhibited ≥ 95% viable cells at concentration ≤160 μg/mL showing that the complex and its conjugate are relatively innocuous against the MCF-7 cells in the absence of light which is a good indication for an ideal PS for PDT. The absence of dark toxicity makes complex **3b** and **3b**-GSS good candidates for PDT. GSS alone (≥ 93% viable cells at 160 μg/mL) also showed no toxicity in the absence of light.

5.1.2. Photodynamic therapy activity.

The PDT activity of the samples was achieved under the same conditions as the dark cytotoxicity study but with a fixed light dosimetry of 170 J/cm^2. When MCF-7 cancer cells were treated with the highest concentration of complex **3b** (160μg/mL), 66% viable cells were obtained (**Figure 5.1A**), even though the Φ_Δ in DMSO was high (0.64). The high percentage cell viability in the presence of **3b** could be attributed to aggregation of the complex in aqueous media as shown by the low Φ_Δ (0.12) values in water with 1.6% DMSO. However, it should be noted that the phototoxicity of the PS is determined by a number of factors including cell type, cellular uptake and localization [237].

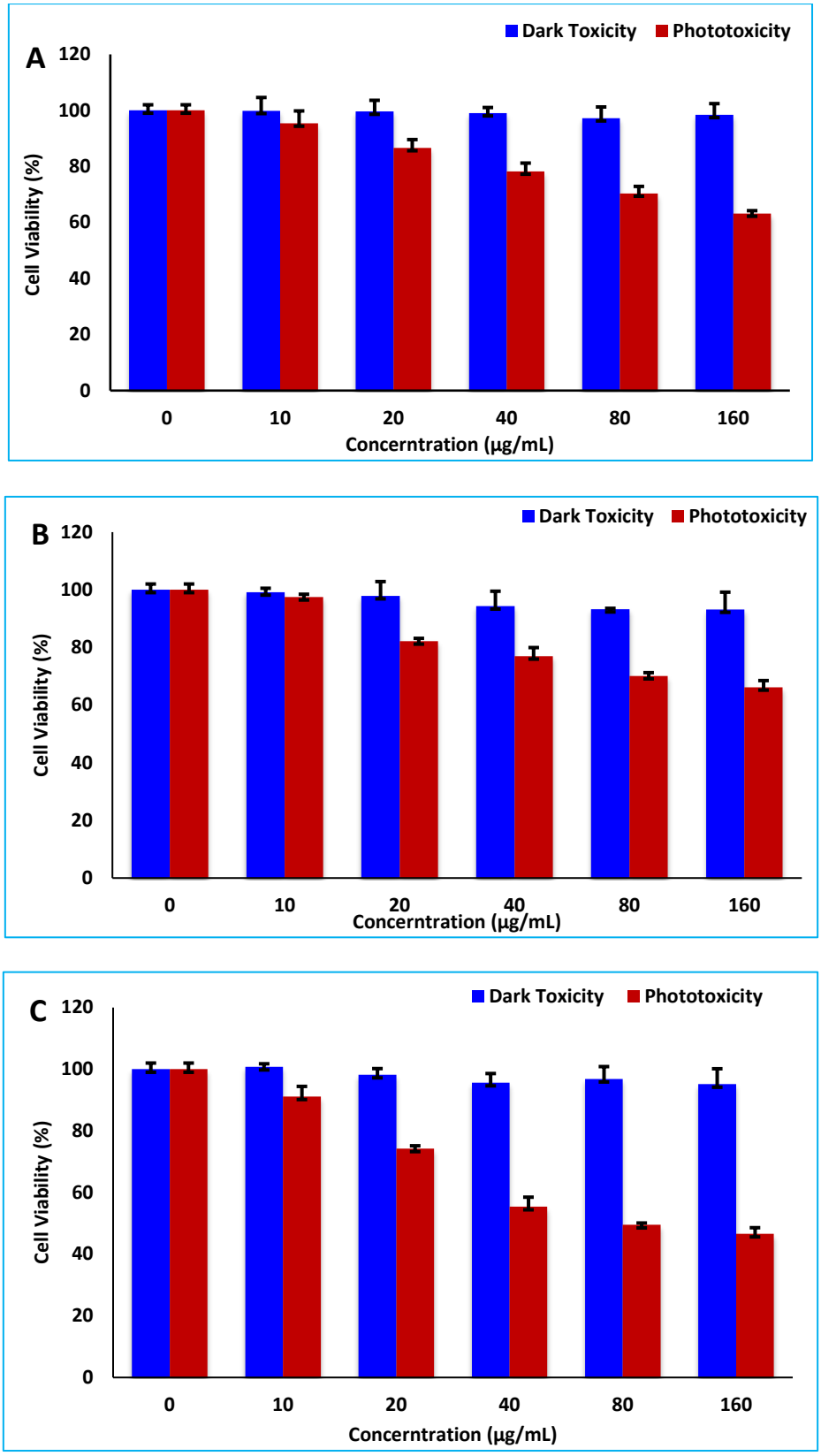

Figure 5.1: Dark toxicity and phototoxicity effects of complex **3b** (A), GSS (B) and **3b**-GSS (C) against epithelial breast cancer cells (MCF–7). Fixed irradiation dose = 170 J/cm^2. Control = 0 µg/mL (with 1.6% DMSO in media)

The poor solubility and lack of cell targeting moieties in complex **3b** could have resulted in poor uptake and localisation of the MPc hence high cell viability.

Complex **3b** was linked to GSS nanoparticles, hence the phototoxicity of GSS alone was tested against the MCF–7 cell lines. The highest concentration of GSS (160 μg/mL) showed cell viability of 63% (**Figure 5.1B**), which surprisingly is slightly higher than that of the MPc alone. Since GSS alone did not show toxicity in the dark, the phototoxicity could probably be due to the photothermal activity as reported before [153]. The conjugate, **3b**-GSS afforded improved PDT activity with cell viability of 49% at 80 μg/mL and 46% at 160 μg/mL, **Fig. 5.1C**. The enhanced PDT activity for **3b**–GSS compared to complex **3b** is attributed to enhanced singlet oxygen quantum yield due to the presence of Au, a heavy atom as explained before, in addition to the phototoxicity contributions from GSS.

5.2. Complex 6 and 6-AuCT.

Gradient photosensitizer concentrations of 3.7 μg/mL to 59.2 μg/mL for dark cytotoxicity and PDT were used.

5.2.1. In vitro dark Cytotoxicity

The in vitro dark cytotoxicity data of complex **6**, AuCT and **6**-AuCT (**Figure 5.2**), accounted for ≥ 90% viable cells at concentration ≤ 59.2 μg/mL which further shows that the complex and its conjugates are mostly inactive in the dark as expected of an ideal PS for PDT.

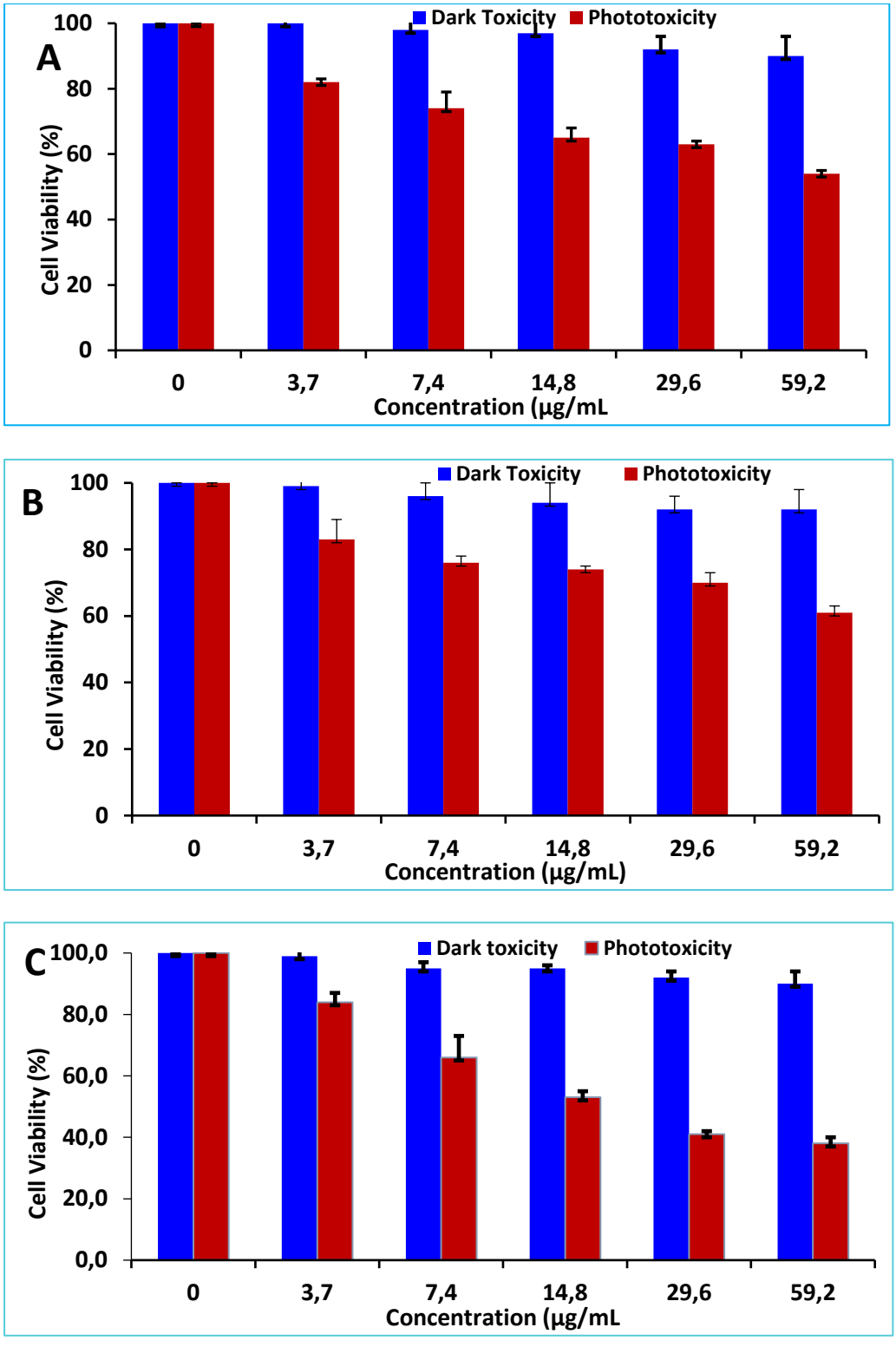

Figure 5.2: Dark toxicity and phototoxicity effects of complex **6** (A), AuCT (B) and **6**-AuCT (C) against epithelial breast cancer cells (MCF–7). Fixed irradiation dose = 170 J/cm^2. Control = 0 µg/mL (with 1.6% DMSO + 1% acetic acid in media)

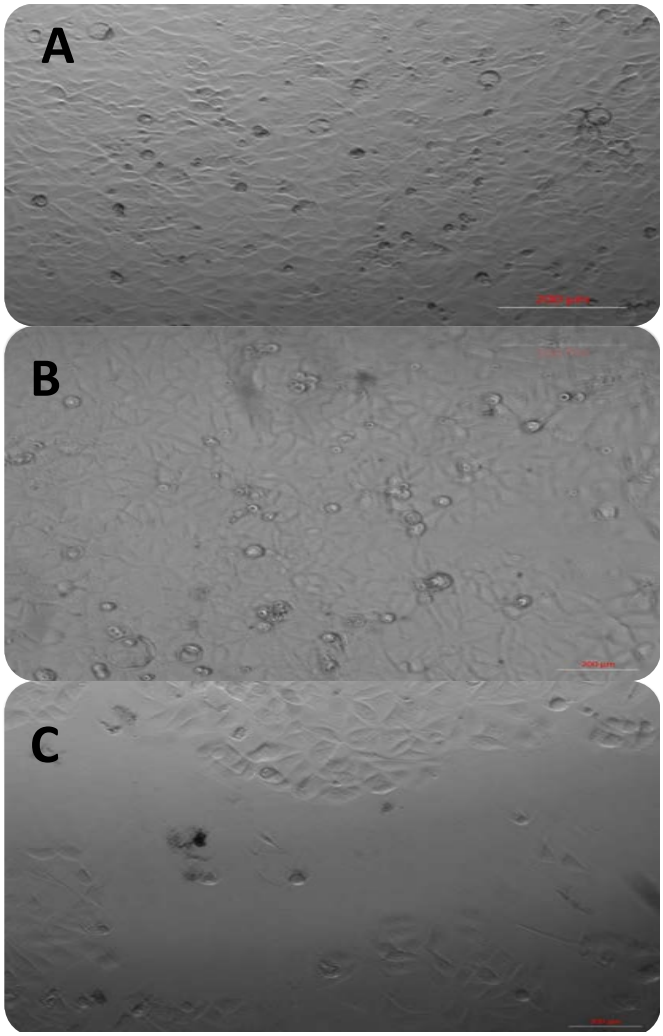

Figure 5.3: Representative MCF-7 breast cancer cells micrographs of cells only (control) (A); cells in the presence of **6**-Au-CT (29.6 µg/mL), without irradiation (B) and with irradiation (C).

The image in **Figure 5.3**, shows that there was insignificant difference between the control cells (A) and cells treated with 29.6 µg/mL **6**-AuCT (B) in the absence of irradiation. Both images (A and B) show that the cells reached confluence covering the entire surface, with some cells growing on top of one another. This shows absence of dark cytoxicity, making complex **6** and **6**-AuCT potential candidates for PDT.

5.2.2. Photodynamic therapy activity.

Complex **6** showed cell viability of ≥ 54% at a concentration ≤ 59.2 μg/mL, **Figure 5.2A**. This could be attributed to the lower Φ_Δ value (= 0.15) in water with 1.6% DMSO. Additionally, poor permeability into the cells could have contributed to the low PDT activity since complex **6** does not have the cell targeting moieties.

The conjugate, **6**-AuCT afforded improved PDT activity with a significant cytocidal activity of 59% (41% cell viability) at 29.6 μg/mL and 62% (38 % cell viabilty) at 59.2 μg/mL, **Figure 5.2C**. The enhanced PDT activity for **6**–AuCT compared to complex **6** on illumination could be due to enhanced singlet oxygen quantum yield (Φ_Δ= 0.21 in water) due to the presence of Au, a heavy atom as explained before. Additionally, the presence of chitosan, which has target moieties (sugars), in the conjugate could have enhanced permeability to the cells since it is recognised by cell surface receptors more than complex **6**.

AuCT alone (**Figure 5.2B**), displayed significant phototoxicity even though the cell viability was above 50% at a concentration ≤ 59.2μg/mL. The phototoxicity could probably be due to the photothermal activity, since gold is known to be a light absorber for cancer therapy [102]. It should be noted however that for PDT studies irradiation was done at 680 nm, and AuNPs absorb less at this wavelength (and most around 548 nm). Thus, the contribution due to photothermal activity is expected to be less than that of PDT. As shown in **Figure 5.2B**, contributions due to the presence of CT are minimal as shown by minimal (to no) dark toxicity for AuCT, even though it

is reported to induce apoptosis in cancer cells [95], while on irradiation a notable toxicity was probably due to the photothermal activity of gold.

The image in **Figure 5.3**, shows a clear difference between the cells with **3**-AuCT (29.6 μg/mL) in the absence of irradiation (B) and after irradiation (C) showing that there is less survival of cells when the conjugate is exposed to light.

5.3. Complex 8, 8-AuNRs-CTAB and 8-AuNSs-CTAB.

In vitro dark cytotoxicity and photodynamic therapy of complex **8** and its conjugates with both AuNRs-CTAB and AuNSs-CTAB were tested against MCF-7 cells. Gradient photosensitizer concentration range of 10 μg/mL to 160 μg/mL for *in vitro* dark cytotoxicity and PDT were used. **Figure 5.4,** shows the dark toxicity and phototoxicity histograms of complex **8, 8**-AuNRs-CTAB and **8**-AuNSs-CTAB. Histograms for AuNRs-CTAB and AuNSs-CTAB alone are shown in **Figure 5.5**.

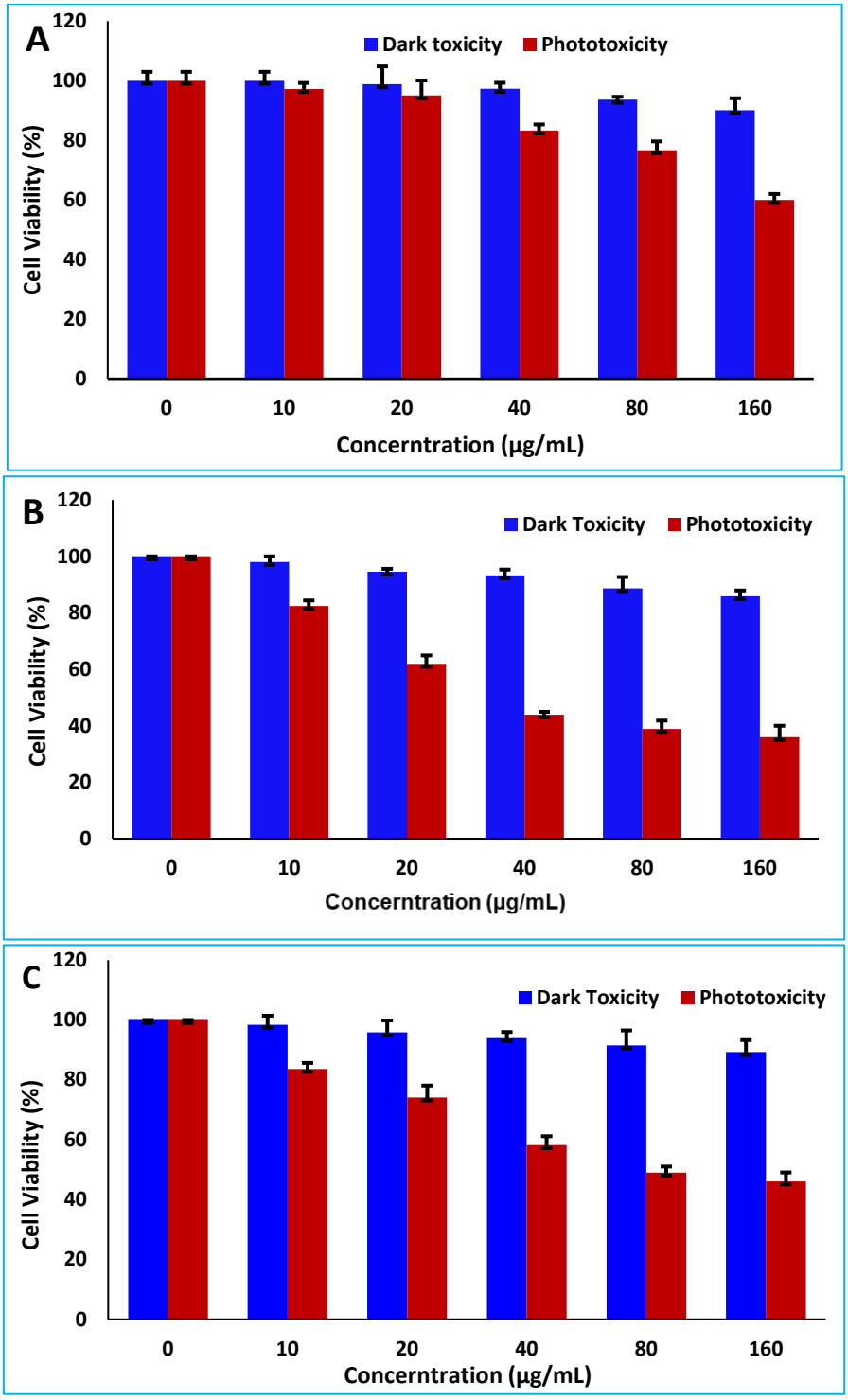

Figure 5.4: Dark toxicity and phototoxicity effects of complex **8** (A), **8**-AuNRs-CTAB (B) and **8**-AuNSs-CTAB (C) against epithelial breast cancer cells (MCF–7). Fixed irradiation dose = 170 J/cm^2. Control = 0 µg/mL (with 1.6% DMSO in media)

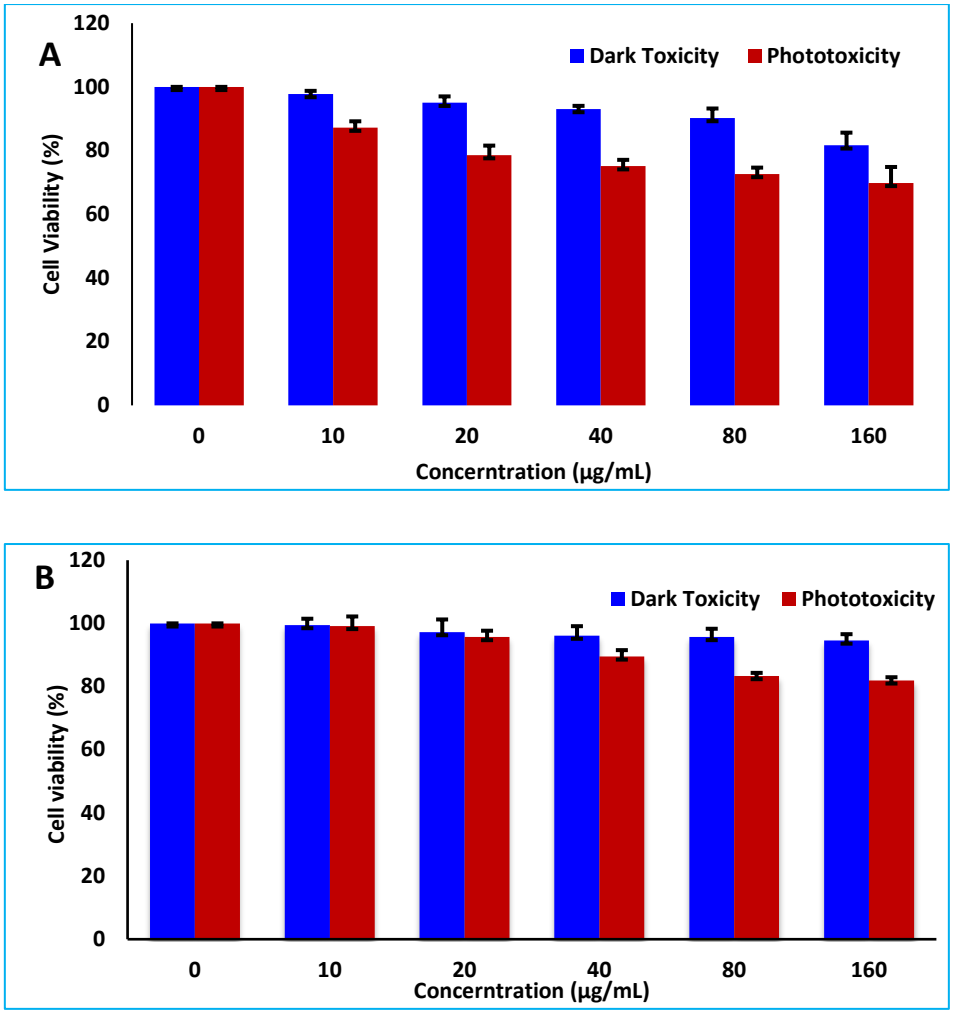

Figure 5.5: Dark toxicity and phototoxicity effects of AuNRs-CTAB (A) and AuNSs-CTAB (B) against epithelial breast cancer cells (MCF–7). Fixed irradiation dose = 170 J/cm^2.

5.3.1. In vitro Dark Cytotoxicity

As shown in **Figure 5.4A**, complex **8** and its conjugate to AuNSs-CTAB (**8**-AuNSs-CTAB) **Figure 5.4C,** accounted for ≥ 90% viable cells at concentration ≤ 160 µg/mL which further lay credence to the innocuous behaviour of phthalocyanines when in dark without light activation. **8**-AuNRs-CTAB on the other hand accounted for ≥ 85% viable cells at concentration ≤ 160 µg/mL. The AuNR alone (**Figure 5.5A**) also showed slight dark toxicity, with ≥ 81%

viable cells at concentration ≤ 160 μg/mL. The slight toxicity was attributed to the CTAB adsorbed on the surfaces of the nanorods.

The toxicity of the CTAB-capped nanorods has been reported before [238–243] and has been attributed to residual CTAB on the surfaces of the rods and not the rods themselves. It is noteworthy that the presence of Pcs in the conjugate decrease the dark cytotoxicity observed in the CTAB-capped nanorods alone, **Figure 5.4B**. This suggests that most of the CTAB on the nanorods were replaced by the Pc on conjugation

5.3.2. Photodynamic therapy activity.

As earlier stated, a fixed light dosimetry of 170 J/cm^2 and gradient photosensitizer concentration range of 10 μg/mL to 160 μg/mL were used against the MCF–7 cells. Complex **8** alone (**Figure 5.4A**) showed cell viability of > 50% at concentrations ≤ 160 μg/mL. This could be attributed to aggregation in aqueous media, which leads to lower singlet oxygen generation (Φ_Δ = 0.08). The nanoparticles alone (**Figure 5.5**) displayed phototoxicity probably due to the photothermal activity of gold, known to be a light absorber for cancer therapy [244,245]. The conjugate, **8**-AuNRs-CTAB (**Figure 5.4B**) afforded superior PDT activity with less than 50% viable cells at concentrations ≥ 40μg/mL in comparison with **8**-AuNSs-CTAB (**Figure 5.4C**) with less than 50% viable cells at a higher concentration of 80μg/mL. This is also shown in **Figure 5.6B**, when the two are compared at the same concentration. The superior PDT activity of **8**-AuNRs-CTAB (Φ_Δ= 0.20 in water with 1.6% DMSO) compared to **8**-AuNSs-CTAB (Φ_Δ= 0.16 in water with 1.6%

DMSO) is attributed to the higher singlet oxygen quantum yield in water (with 1.6% DMSO; **Table 4.3**), in addition to the phototoxicity of nanorods. It should be noted that for the PDT studies, excitation was performed at 680 nm and AuNRs-CTAB (with SPR bands at 519nm and 662 nm) absorb more light at this wavelength than AuNSs-CTAB (with SPR bands at 525 nm). The enhanced PDT activity for the conjugates compared to complex **8** alone is attributed to the phototoxicity of NPs in addition to the enhanced singlet oxygen quantum yield of the conjugates as shown in **Table 4.3**, due to the presence of Au, a heavy atom and light absorber, as explained before.

5.4. Comparison of the in vitro dark cytotoxicity and PDT activity of 3b-GSS, 8-AuNRs-CTAB, 8-AuNSs-CTAB at 160 µg/mL and 59.2 µg/mL for 6-AuCT

In vitro dark cytotoxicity and photodynamic therapy of the conjugates **3b**-GSS, **8**-AuNRs-CTAB, **8**-AuNSs-CTAB at 160 µg/mL and **6**-AuCT at 59.2 µg/mL (which is their highest concerntration used) against MCF-7 cells were compared. **Figure 5.6A,** shows the dark toxicity histograms and **Figure 5.6B** phototoxicity histograms.

5.4.1. In vitro Dark Cytotoxicity

As shown in **Figure 5.5A**, **3b**-GSS showed the highest cell viability at ≥ 95% at concentration ≤ 160 µg/mL while **6**-AuCT and **8**-AuNRs-CTAB

showed ≥ 90% at concentration ≤ 59.2 µg/mL for **6**-AuCT and ≤ 160 µg/mL for **8**-AuNRs-CTAB. **8**-AuNRs-CTAB on the other hand accounted for ≥ 85% viable cells at concentration ≤ 160 µg/mL attributed to the toxicity of CTAB as previously stated. The levels of CTAB in **8**-AuNRs-CTAB and **8**-AuNSs-CTAB are different probably due to the differences in the purification stage of the conjugates (suggesting more residual CTAB in the former than the latter).

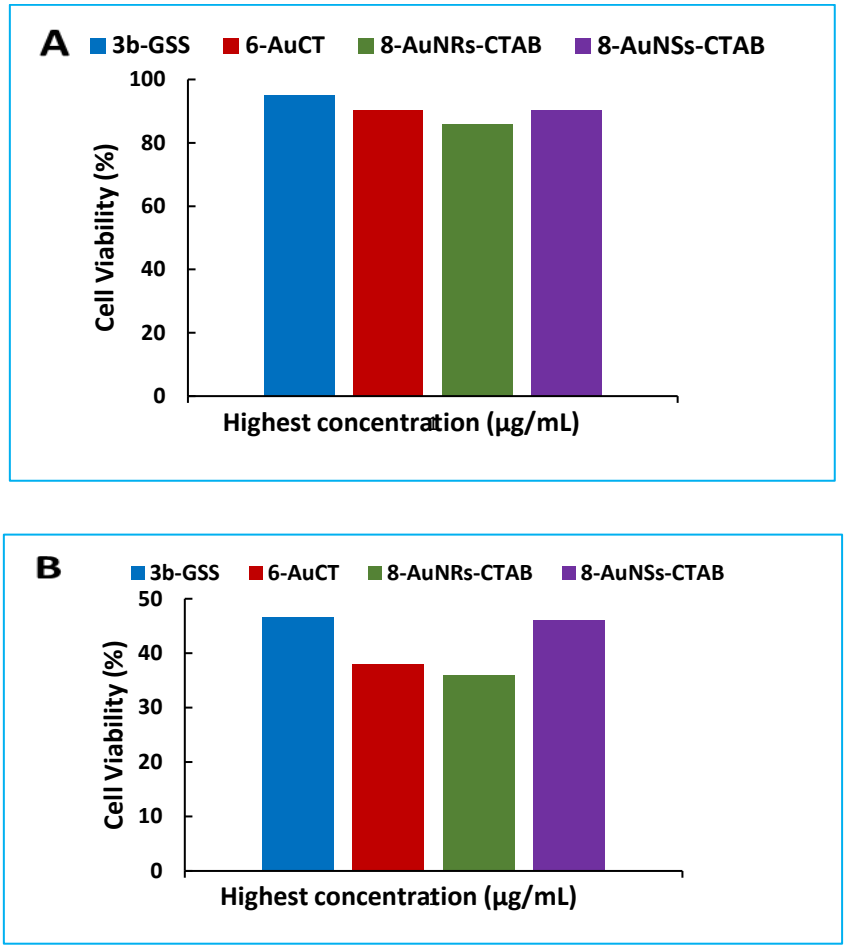

Figure 5.6: A) Dark toxicity and **B)** phototoxicity effects of **3b**-GSS, **8**-AuNRs-CTAB, **8**-AuNSs-CTAB at 160 µg/mL and **6**-AuCT at 59.2 µg/mL against epithelial breast cancer cells (MCF–7). Fixed irradiation dose = 170 J/cm^2.

5.4.2. Photodynamic therapy activity

As shown in **Figure 5.5B**, **8**-AuNRs-CTAB showed ≥ 36% cell viability at concentration 160 µg/mL, while **6**-AuCT with a lower concentration of 59.2 µg/mL showed ≥ 38% cell viability. **8**-AuNSs-CTAB and **3b**-GSS showed the lowest PDT activity of the studied conjugates with ≥ 46% viable cells at 160 µg/mL. **6**-AuCT (59.2 µg/mL) showed the best PDT activity of the studied conjugates since it showed ≥ 38 % viable cells at less than half the concentration of **8**-AuNRs-CTAB (160 µg/mL).

The conjugate **3b**-GSS, has higher cell viability on illumination due to the low Φ_Δ and probably poor cellular uptake.The conjugates to complexes **6** and **8**, have an advantage of asymmetry but **6**-AuCT has sugar moieties from chitosan which improves its solubility and cellular uptake hence the superior PDT activity than complex **8,** with protected sugars. The protecting isopropylidene groups in complex **8**, reduce solubilty in aqueous media and the cellular uptake.

5.5. Summary of chapter

In vitro dark cytotoxicity and photodynamic therapy of complexes **3b, 3b**-GSS**,** complex **6, 6**-AuCT**,** complex **8, 8**-AuNRs-CTAB and **8**-AuNSs-CTAB against MCF-7 cells were presented. The complexes were relatively not toxic in the dark, with complex **3b**, and **3b**-GSS, showing ≥ 95% viable cells at

concentration ≤160 μg/mL; complex **8** and **8**-AuNSs-CTAB having ≥ 90% viable cells at concentration ≤ 160 μg/mL. However, **8**-AuNRs-CTAB showed slight toxicity attributed to residual CTAB on the surface of nanorods. Different concentrations were used for complex **6**, AuCT and **6**-AuCT, which showed ≥ 90% viable cells at concentrations ≤ 59.2 μg/mL. The minimum dark toxicity displayed by complexes **3b**, **3b**-GSS**,** complex **6, 6**-AuCT, complex **8** and **8**-AuNSs-CTAB, make them good candidates for real life PDT applications.

All complexes when alone, displayed poor phototoxicity with > 50% cell viability at concentrations ≤ 160 μg/mL. This could be attributed to aggregation in aqueous media, which leads to lower singlet oxygen generation. However, on linkage to NPs there was reduced cell viability, with **3b**-GSS showing 46% viable cells at 160 μg/mL; **6**-AuCT 38% viable cells at 59.2 μg/mL; **8**-AuNRs-CTAB and **8**-AuNSs-CTAB showing 39% and 46% viable cells respectively at 160 μg/mL.

The conjugate **6**-AuCT showed both minimum dark toxicity and the best PDT activity of all complexes and conjugates studied, making it a potential candidate for real life PDT applications.

CHAPTER 6

6. Conclusions and recommendations

This chapter summarizes the results obtained for the studies conducted and reported in this thesis and recommendations.

6.1. Conclusion

This work presents the successful synthesis and characterization of new symmetric and asymmetric Pcs functionalized at the peripheral position. The Pcs were characterised using FTIR, UV-Vis, ^{1}HNMR, MALDI-TOF mass spectroscopies and elemental analyses. The prepared Pcs were soluble in DMSO and exhibited monomeric behaviour in solution. These were further linked to various gold containing NPs through either Au-S/Au-N self-assembly or amide bond formation from functionalised NPs. FT–IR spectroscopy was used to confirm the successful formation of the amide bond and X–ray photoelectron spectroscopy was used to confirm the Au-S/Au-N bonds.

The effect of metal centres, substituents and symmetry of Pcs together with the shape and size of the linked nanoparticles on the photochemical and photophysical behaviour of Pcs was studied. Heavy atoms as metal centres, substituents with extra phenyl rings and asymmetry of Pcs were shown to promote intersystem crossing resulting in high triplet and singlet oxygen quantum yields.

The presence of gold/silver containing nanoparticles enhanced the triplet and singlet oxygen quantum yields of Pcs and this was attributed to the heavy atom effect of the nanoparticles. However, **1**–Ag_3Au_1NSs–GSH, **1**–Ag_1Au_3NSs–GSH, **2**-Ag_3Au_1NSs–GSH and **5**-Ag_3Au_1NSs–GSH displayed increased triplet quantum yields, but afforded lower singlet oxygen quantum yield than their respective complexes alone, probably signifying poor interaction of the excited

triplet state of the conjugates and the ground state molecular oxygen, and this was attributed to the screening effect caused by the capping ligand around the surface of the NPs.

The nanoparticle shape and size were also shown to influence the photochemical and photophysical behaviour of Pcs studied. AuNSs-CTAB afforded high triplet and singlet oxygen quantum yields than AuNTs-CTAC due to the small size of the former, that loaded more Pcs due to a higher surface area than AuNTs-CTAC. However larger GSS nanoparticles also afforded higher triplet and singlet oxygen quantum yields than AuNSs-CTAB due to high loading which was attributed to the porous nature of SiNSs in GSS that increases the surface area for loading.

Furthermore, *in vitro* dark cytotoxicity and photodynamic therapy of complexes **3b, 3b**-GSS**,** complex **6, 6**-AuCT**,** complex **8**, **8**-AuNRs-CTAB and **8**-AuNSs-CTAB against MCF-7 cells was tested. All complexes and conjugates showed minimum dark toxicity making them applicable for PDT except **8**-AuNR-CTAB which showed slight dark toxicity probably due to the presence of residual CTAB on the surfaces of NPs. All complexes displayed poor phototoxicity with > 50% cell viability at concentrations ≤ 160 μg/mL, however the conjugates showed < 50% cell viability at concentrations ≤ 160 μg/mL probably to the heavy atom effect of gold in the NPs, in addition to reduced aggregation. The conjugates **3b**-GSS, **6**-AuCT and **8**-AuNSs-CTAB showed both minimum dark toxicity and better PDT activity than Pc complexes alone making them good candidates for real life PDT

applications, however **6**-AuCT was the best conjugate since displayed the best PDT activity of all complexes and conjugates studied.

6.2. Recommendations

The synthesised Pcs were not soluble in aqueous media, hence the cell viability of > 50% in PDT studies. Efforts will be made to synthesize water soluble Pcs and possible conjugation to gold containing NPs. PDT activity

of the Pcs will be tested using different cancer cells.

Water soluble asymmetric Pcs, with indium as a central metal will be synthesised for improved singlet oxygen quantum yield and better cellular uptake.

More glycosylated asymmetric Pcs will be synthesised, and efforts made to unprotect the sugars for improved water solubility and cellular uptake.

For the effect of NPs size, attempts will be made to separate the NPs especially nanotriangles into different sizes and possible evaluate the effect of different sizes of nanotriangles on the photophysical and photochemical properties of Pcs.

References

[1] G. De La Torre, C.G. Claessens, T. Torres, Chem. Commun. 20 (2007) 2000–2015.

[2] T. Fukuda, N. Kobayashi, in:, K.M. Kadish, K.M. Smith, R. Guilard (Eds.), Handb. Porphyr. Sci., 9th ed., World Scientific Press, 2010, pp. 1–644.

[3] L.M. Moreira, F.V. Dos Santos, J.P. Lyon, M. Maftoum-Costa, C. Pacheco-Soares, N. Soares Da Silva, Aust. J. Chem 61 (2008) 741–754.

[4] R. Bonnett, In Chemical Aspects of Photodynamic Therapy, Gordon and Breach Science Publishers, Amsterdam, 2000.

[5] S.B. Brown, E.A. Brown, I. Walker, Lancet Oncol. 5 (2004) 497–508.

[6] V. Mantareva, I. Angelov, V. Kussovski, D. Woehrle, S. Dimitrov, Comptes Rendus L'Academie Bulg. Des Sci. 63 (2010) 77–84.

[7] D. Mondal, S. Bera, Adv. Nat. Sci. Nanosci. Nanotechnol. 5 (2014) 033002 (12 pages).

[8] M. Wainwright, J. Antimicrob. Chemother. 42 (1998) 13–28.

[9] R. Zugle, T. Nyokong, J. Appl. Polym. Sci. 128 (2013) 1131–1142.

[10] M. Hanack, T. Schneider, M. Barthel, J.S. Shirk, S.R. Flom, R.G.S. Pong, Coord. Chem. Rev. 219 (2001) 235–258.

[11] P. Gregory, High-Technology Applications of Organic Colourants, 7th ed., Plenum Press, New York, 1991.

[12] I. Okura, Photosensitization of Porphyrins and Phthalocyanines, Gordon and Breach Science Publishers, Netherlands, 2000.

[13] D. Dini, M. Hanack, in:, K.M. Kadish, K.M. Smith, R. Guilard (Eds.), Porphyr. Handb., 17th ed., Academic Press, New York, 2003, pp. 1–31.

[14] E. Ben-Hur, W.S. Chan, in:, K.M. Kadish, K.M. Smith, R. Guilard (Eds.), Porphyr. Handb., 19th ed., Academic Press, New York, 2003, pp. 1–35.

[15] P. Gregory, J. Porphyr. Phthalocyanines 4 (2000) 432–437.

[16] T. Fukuda, K. Ono, S. Homma, N. Kobayashi, Chem. Lett. 32 (2003) 736–737.

[17] T. Nyokong, in:, J. Jiang (Ed.), Funct. Phthalocyanine Mol. Mater. Struct. Bond., 135th ed., Springer, New York, 2010, pp. 45–87.

[18] N. Kobayashi, H. Ogata, N. Nonaka, E.A. Luk'yanets, Chem. Eur. J. 9 (2003) 5123–5134.

[19] N. Kobayashi, H. Konami, in:, C.C. Leznoff, A.B.P. Lever (Eds.), Phthalocyanines Prop. Appl., 4th ed., VCH, New York, 1996, pp. 343–404.

[20] L. Edwards, M. Gouterman, J. Mol. Spectrosc. 33 (1970) 292–310.

[21] M. Gouterman, The Porphyrins, Part A. Physical Chemistry, 3rd ed., Academic Press, New York, 1978.

[22] A. Henriksson, M. Sundbom, Theor. Chim. Acta 27 (1972) 213–222.

[23] C.G. Claessens, U. Hahn, T. Torres, Chem. Rec. 8 (2008) 75–97.

[24] P. Yiru, H. Fenghua, L. Zhipeng, C. Naisheng, H. Jinling, Inorg. Chem. Commun. 7 (2004) 967–970.

[25] N.B. McKeown, Phthalocyanine Materials: Synthesis, Structure, and Function. Chemistry of Solid State Materials, Cambridge University Press, New York, 1998.

[26] F. Dumoulin, M. Durmuş, V. Ahsen, T. Nyokong, Coord. Chem. Rev. 254 (2010) 2792–2847.

[27] V.N. Nemykin, E.A. Lukyanets, Arkivoc 2010 (2010) 136–208.

[28] W. Liu, C. Lee, H. Chan, T.C.W. Mak, D.K.P. Ng, Eur. J. Inorg. Chem. (2004) 286–292.

[29] V. Novakova, J. Roh, P. Gela, J. Kuneš, P. Zimcik, Chem. Commun. 48 (2012) 4326–4328.

[30] W.M. Sharman, J.E. Van Lier, in:, K.M. Kadish, K.M. Smith, R. Guilard (Eds.), Porphyr. Handb., 15th ed., Academic Press, San Diego, 2003, pp. 1–53.

[31] V.N. Nemykin, S. V. Dudkin, F. Dumoulin, C. Hirel, A.G. Gürek, V. Ahsen, Arkivoc 2014 (2014) 142–204.

[32] C.C. Byeon, M.M. McKerns, W. Sun, T.M. Nordlund, C.M. Lawson, G.M. Gray, Appl. Phys. Lett. 84 (2014) 5174–5176.

[33] T. Fukuda, S. Homma, N. Kobayashi, Chem. Eur. J. 11 (2005) 5205–5216.

[34] S.M. RodríGuez-Morgade, G. De La Torre, T. Torres, in:, K.M. Kadish, K.M. Smith, R. Guilard (Eds.), Porphyr. Handb. Phthalocyanines Synth., 15th ed., Academic Press, San Diego, 2003, pp. 125–155.

[35] Y. Liu, Y. Xu, D. Zhu, T. Wada, H. Sasabe, L. Liu, W. Wang, Thin Solid Films 244 (1994) 943–946.

[36] Y. Liu, D. Zhu, T. Wada, A. Yamada, H. Sasabe, J. Heterocycl. Chem. 31 (1994) 1017–1020.

[37] D.O. Oluwole, T. Nyokong, J. Photochem. Photobiol. A Chem. 312 (2015) 34–44.

[38] A. Aktaş, M. Durmuş, I. Degirmencioglu, Polyhedron 48 (2012) 80–91.

[39] N. Nwaji, B. Jones, J. Mack, D.O. Oluwole, T. Nyokong, J. Photochem. Photobiol. A Chem. 346 (2017) 46–59.

[40] J. Obirai, T. Nyokong, Electrochim. Acta 50 (2005) 5427–5434.

[41] K. Hayashi, M. Nakamura, H. Miki, S. Ozaki, Adv. Funct. Mater. 24 (2014) 503–513.

[42] A. Gorman, J. Killoran, C. O'Shea, T. Kenna, W.M. Gallagher, D.F. O'Shea, J. Am. Chem. Soc. 126 (2004) 10619–10631.

[43] B.C. De Simone, G. Mazzone, N. Russo, E. Sicilia, M. Toscano, Molecules 22 (2017) 1093 (10 pages).

[44] Y. Shimzu, T. Azumi, J. Phy. Chem. 86 (1982) 22–26.

[45] T. Nyokong, Coord. Chem. Rev. 251 (2007) 1707–1722.

[46] A. Ogunsipe, J.-Y. Chen, T. Nyokong, New. J. Chem. 28 (2004) 822–827.

[47] C. Xia, Y. Wang, W. Chen, W. Yu, B. Wang, T. Li, Molecules 16 (2011) 1389–1401.

[48] M.T. Colvin, A.B. Ricks, A.M. Scott, D.T. Co, M.R. Wasielewski, J. Phys. Chem. A 116 (2012) 1923–1930.

[49] C.G. Mortimer, G. Wells, J. Crochard, E.L. Stone, T.D. Bradshaw, M.F.G. Stevens, A.D. Westwell, J. Med. Chem 49 (2006) 179–185.

[50] D. Havrylyuk, L. Mosula, B. Zimenkovsky, O. Vasylenko, A. Gzella, R. Lesyk, Eur. J. Med. Chem. 45 (2010) 5012–5021.

[51] P.C. Sharma, A. Sinhmar, A. Sharma, H. Rajak, D.P. Pathak, J. Inhib. Med. Chem. 28 (2013) 240–266.

[52] K.S. Rakesh, S. Jagadish, T.R. Swaroop, C.D. Mohan, N. Ashwini, K.B. Harsha, F. Zameer, K.S. Girish, K.S. Rangappa, Med. Chem. 11 (2015) 462–472.

[53] F. A. Dos Santos, M.C. Pereira, T.B. De Oliveira, F.J. Mendonça, M.C. Lima, M.G. Pitta, I.R. Pitta, M.J. Rêgo, M.G. Rocha, Anticancer. Drugs

29 (2018) 157–166.

[54] S. Singh, A. Aggarwal, N.V.S.D.K. Bhupathiraju, G. Arianna, K. Tiwari, C.M. Drain, Chem. Rev. 115 (2015) 10261–10306.

[55] S. Anand, B.J. Ortel, S.P. Pereira, T. Hasan, E.V. Maytin, Cancer Lett. 326 (2012) 8–16.

[56] R. Ackroyd, C. Kelty, N. Brown, M. Reed, Photochem. Photobiol. 74 (2001) 656–669.

[57] J.P. Celli, B.Q. Spring, I. Rizvi, C.L. Evans, K.S. Samkoe, S. Verma, B.W. Pogue, T. Hasan, Chem. Rev. 110 (2010) 2795–2838.

[58] Á. Juarranz, P. Jaén, F. Sanz-Rodríguez, J. Cuevas, S. González, Clin. Transl. Oncol. 10 (2008) 148–154.

[59] M. Alemany-Ribes, M. García-Díaz, P. Acedo, M. Agut, S. Nonell, M.L. Sagristá, M. Mora, M. Cañete, Á. Villanueva, J.C. Stockert, C.E.J. Semino, J. Anal. Bioanal. Tech. S1. (2013) 004 (6 pages).

[60] P.C. Lo, S.Y.S. Chow, D.K.P. Ng, in:, K.D. Pandey Ravindra, Dougherty Thomas J (Ed.), Handb. Photodyn. Ther. Recent Appl., World Scientific Press, Singapore, 2016, pp. 237–272.

[61] R.R. Allison, G.H. Downie, R. Cuenca, X.-H. Hu, C.J. Childs, C. Sibata, Photodiagnosis Photodyn. Ther. 1 (2004) 27–42.

[62] L.B. Josefsen, R.W. Boyle, Theranostics 2 (2012) 916–966.

[63] K. Plaetzer, B. Krammer, J. Berlanda, F. Berr, T. Kiesslich, Lasers Med. Sci. 24 (2009) 259–268.

[64] B.W. Henderson, T. Dougherty, Photochem. Photobiol. 55 (1992) 145–157.

[65] T.J. Dougherty, C.J. Gomer, B.W. Henderson, G. Jori, D. Kessel, M.

Korbeilk, J. Moan, Q. Peng, J. Natl. Cancer Inst. 90 (1998) 899–905.

[66] J. Taquet, C. Frochot, V. Manneville, M. Barberi-Heyob, Curr. Med. Chem. 14 (2007) 1673–1687.

[67] A.S. Derycke, P.A. de Witte, Adv. Drug Deliv. Rev. 56 (2004) 17–30.

[68] A.R. Simioni, M.M. Pelisson, M. Beltrame, A.C. Tedesco, J. Nanosci. Nanotechnol. 8 (2008) 3208–3215.

[69] K. Sugisaki, T. Usui, N. Nishiyama, W.D. Jang, Y. Yanagi, S. Yamagami, S. Amano, K. Kataoka, Invest. Ophthalmol. Vis. Sci. 49 (2008) 894–899.

[70] C.F. van Nostrum, Adv. Drug Deliv. Rev. 56 (2004) 9–16.

[71] M. Bhatti, G. Yahioglu, L.R. Milgrom, M. Garcia-Maya, K.A. Chester, M.P. Deonarain, Int. J. Cancer 122 (2008) 1155–1163.

[72] K. Ichikawa, T. Hikita, N. Maeda, S. Yonezawa, Y. Takeuchi, T. Asai, Y. Namba, N. Oku, Biochim. Biophys. Acta 1669 (2005) 69–74.

[73] I. Roy, T.Y. Ohulchanskyy, H.E. Pudavar, E.J. Bergey, A.R. Oseroff, J. Morgan, T.J. Dougherty, P.N. Prasad, J. Am. Chem. Soc. 125 (2003) 7860–7865.

[74] M.E. Wieder, D.C. Hone, M.J. Cook, M.M. Handsley, J. Gavrilovic, D.A. Russell, Photochem. Photobiol. Sci. 5 (2006) 727–734.

[75] Z. Iqbal, A. Lyubimtsev, M. Hanack, T. Ziegler, Tetrahedron Lett. 50 (2009) 5681–5685.

[76] I. Laville, S. Pigaglio, J.C. Blais, F. Doz, B. Loock, P. Maillard, D.S. Grierson, J. Blais, J. Med. Chem. 49 (2006) 2558–2567.

[77] P.C. Lo, C.M. Chan, J.Y. Liu, W.P. Fong, D.K. Ng, J. Med. Chem. 50 (2007) 2100–2107.

[78] Y. Zorlu, M.A. Ermeydan, F. Dumoulin, V. Ahsen, H. Savoie, R.W. Boyle,

Photochem. Photobiol. Sci. 8 (2009) 312–318.

[79] C.F. Choi, J.D. Huang, P.C. Lo, W.P. Fong, D.K. Ng, Org. Biomol. Chem. 6 (2008) 2173–2181.

[80] S.G. Kimani, T.A. Shmigol, S. Hammond, J.B. Phillips, J.I. Bruce, A.J. MacRobert, M.V. Malakhov, J.P. Golding, Photochem. Photobiol. 89 (2013) 139–149.

[81] D.K. Chatterjee, L.S. Fong, Y.A. Zhang, Drug Deliv. Rev. 60 (2008) 1627–1637.

[82] G. Obaid, M. Broekgaarden, A.L. Bulin, H.C. Huang, J. Kuriakose, J. Liu, T. Hasan, Nanoscale 8 (2016) 12471–12503.

[83] S. Kapse-Mistry, T. Govender, R. Srivastava, M. Yergeri, Front. Pharmacol. 5 (2014) 159 (22 pages).

[84] Y. Omidi, J. Barar, BioImpacts 4 (2014) 55–67.

[85] P. García Calavia, D.A. Russell, in:, H. Kostron, T. Hasan (Eds.), Photodyn. Med. From Bench to Clin., Published by RSC, Croydon, 2016, pp. 113–135.

[86] G. Obaid, D.A. Russell, in:, M.R. Hamblin, Y.Y. Huang (Eds.), Handb. Photomed., Taylor & Francis, Boca Raton, 2013, pp. 367–378.

[87] S.S. Lucky, K.C. Soo, Y. Zhang, Chem. Rev. 115 (2015) 1990–2042.

[88] W. Lu, Q. Huang, G. Ku, X. Wen, M. Zhou, D. Guzatov, P. Brecht, R. Su, A. Oraevsky, L. V Wang, C. Li, Biomaterials 31 (2010) 2617–2626.

[89] V. Biju, B.G. Trewyn, I.I. Slowing, S. Giri, H.-T. Chen, Chem. Soc. Rev. 43 (2014) 744–764.

[90] K.S. Abhijith, R. Sharma, R. Ranjan, M.S. Thakur, Photochem. Photobiol. Sci. 13 (2014) 986–991.

[91] S. Dengler, C. Kübel, A. Schwenke, G. Ritt, B. Eberle, J. Opt. 14 (2012) 075203 (8 pages).

[92] I. Shmarakov, I. Mukha, N. Vityuk, V. Borschovetska, N. Zhyshchynska, G. Grodzyuk, A. Eremenko, Nanoscale Res. Lett. 12 (2017) 333 (10 pages).

[93] P. Sharma, S.C. Brown, A. Singh, N. Iwakuma, G. Pyrgiotakis, V. Krishna, J.A. Knapik, K. Barr, B.M. Moudgil, S.R. Grobmyer, J. Mater. Chem. 20 (2010) 5182–5185.

[94] P. Sharma, S.C. Brown, N. Bengtsson, Q. Zhang, G.A. Walter, S.R. Grobmyer, S. Santra, H. Jiang, E.W. Scott, B.M. Moudgil, Chem. Mater. 20 (2008) 6087–6094.

[95] F. Salehi, H. Behboudi, G. Kavoosi, S.K. Ardestani, RSC Adv. 7 (2017) 43141–43150.

[96] P. Tallury, S. Kar, S. Bamrungsap, Y.-F. Huang, W. Tan, S. Santra, Chem. Commun. (2009) 2347–2349.

[97] M.A. Elgadir, M.S. Uddin, S. Ferdosh, A. Adam, A.J.K. Chowdhury, M.Z.I. Sarker, J. Food Drug Anal. 23 (2015) 619–629.

[98] Q. Xu, C. Mao, N.N. Liu, J.J. Zhu, J. Sheng, Biosens. Bioelectron. 22 (2006) 768–773.

[99] G. Di Carlo, A. Curulli, R.G. Toro, C. Bianchini, T. De Caro, G. Padeletti, D. Zane, G.M. Ingo, Langmuir 28 (2012) 5471–5479.

[100] M.R. Papasani, G. Wang, R.A. Hill, Nanomedicine Nanotechnology, Biol. Med. 8 (2012) 804–814.

[101] Z. Chen, Z. Wang, X. Chen, H. Xu, J. Liu, J. Nanoparticle Res. 15 (2013) 1930 (30 pages).

[102] G. Zhang, X. Sun, J. Jasinski, D. Patel, A.M. Gobin, J. Nanomater. 2012 (2012) 853416 (9 pages).

[103] F. Jabeen, M. Najam-ul-Haq, R. Javeed, C.W. Huck, G.K. Bonn, Molecules 19 (2014) 20580–20593.

[104] J. Lv, Y. Yi, G.Q. Wu, W. Liu, Mater. Lett. 187 (2017) 148–150.

[105] B. Ankamwar, M. Chaudhary, M. Sastry, Synth. React. Inorg. Met.-Org. Nano-Met. Chem. 35 (2005) 19–26.

[106] K. Madhumathi, P.T.S. Kumar, S. Abhilash, V. Sreeja, H. Tamura, K. Manzoor, S. V. Nair, R. Jayakumar, J. Mater. Sci. Mater. Med. 21 (2010) 807–813.

[107] T.A. Dankovich, D.G. Gray, Environ. Sci. Technol. 45 (2011) 1992–1998.

[108] J.M. Köhler, L. Abahmane, J. Wagner, J. Albert, G. Mayer, Chem. Eng. Sci. 63 (2008) 5048–5055.

[109] M.A. Al-Azawi, N. Bidin, M. Bououdina, S.M. Mohammad, Sol. Energy 126 (2016) 93–104.

[110] V.M. Blas-Ferrando, J. Ortiz, F. Fernández-Lázaro, Á. Sastre-Santos, J. Porphyr. Phthalocyanines 19 (2015) 335–343.

[111] D.C. Hone, P.I. Walker, R. Evans-Gowing, S. FitzGerald, A. Beeby, I. Chambrier, M.J. Cook, D.A. Russell, Langmuir 18 (2002) 2985–2987.

[112] O. Osifeko, T. Nyokong, Dye. Pigment. 131 (2016) 186–200.

[113] N. Nombona, E. Antunes, C. Litwinski, T. Nyokong, Dalt. Trans. 40 (2011) 11876–11884.

[114] L.F. Freitas, M.R. Hamblin, F. Anzengruber, J.R. Perussi, A.O. Ribeiro, V.C.A. Martins, A.M.G. Plepis, J. Photochem. Photobiol. B Biol. 173 (2017) 181–186.

[115] T. Mthethwa, E. Antunes, T. Nyokong, Dalt. Trans. 43 (2014) 8230–820.

[116] T. Mthethwa, T. Nyokong, Photochem. Photobiol. Sci. 14 (2015) 1346–1356.

[117] J. Wang, H.Y. Tang, W.L. Yang, J.Y. Chen, J. Porphyr. Phthalocyanines 16 (2012) 802–808.

[118] S. D'Souza, S. Moeno, E. Antunes, T. Nyokong, New J. Chem. 37 (2013) 1950–1958.

[119] P. Khoza, E. Antunes, T. Nyokong, J. Mol. Catal. A Chem. 395 (2014) 34–41.

[120] P. Khoza, T. Nyokong, J. Mol. Catal. A Chem. 399 (2015) 25–32.

[121] D.O. Oluwole, E. Prinsloo, T. Nyokong, Polyhedron 119 (2016) 434–444.

[122] O.M. Bankole, O. Osifeko, T. Nyokong, J. Photochem. Photobiol. A Chem. 329 (2016) 155–166.

[123] I. Maliszewska, W. Kałas, E. Wysokińska, W. Tylus, N. Pietrzyk, K. Popko, K. Palewska, Lasers Med. Sci. 33 (2018) 79–88.

[124] J.R. Siqueira, L.H.S. Gasparotto, F.N. Crespilho, A.J.F. Carvalho, V. Zucolotto, O.N. Oliveira, J. Phys. Chem. B 110 (2006) 22690–22694.

[125] A.B. Sorokin, F. Quignard, R. Valentin, S. Mangematin, Appl. Catal. A Gen. 309 (2006) 162–168.

[126] C. Shen, S. Song, L. Zang, X. Kang, Y. Wen, W. Liu, L. Fu, J. Hazard. Mater. 177 (2010) 560–566.

[127] A.T.B. Silva, A.G. Coelho, L.C.S. Da Lopes, M.V.A. Martins, F.N. Crespilho, A. Merkoçi, W.C. Da Silva, J. Braz. Chem. Soc. 24 (2013) 1237–1245.

[128] A. Hamdi, S. Boufi, S. Bouattour, Appl. Surf. Sci. 339 (2015) 128–136.

[129] F. Ali, S.B. Khan, T. Kamal, Y. Anwar, K.A. Alamry, A.M. Asiri, Carbohydr. Polym. 173 (2017) 676–689.

[130] A.R. Karimi, A. Khodadadi, M. Hadizadeh, RSC Adv. 6 (2016) 91445–91452.

[131] D.O. Oluwole, E. Prinsloo, T. Nyokong, Spectrochim. Acta - Part A Mol. Biomol. Spectrosc. 173 (2017) 292–300.

[132] X. Xie, J. Liao, X. Shao, Q. Li, Y. Lin, Sci Rep. 7 (2017) 3827 (9 pages).

[133] M.A. Gatoo, S. Naseem, M.Y. Arfat, A. Mahmood Dar, K. Qasim, S. Zubair, Biomed Res. Int. 2014 (2014) 498420 (8 pages).

[134] T. Nyokong, E. Antunes, Coord. Chem. Rev. 257 (2013) 2401–2418.

[135] M.C. Daniel, D. Astruc, Chem. Rev. 104 (2004) 293–346.

[136] S. Dixit, T. Novak, K. Miller, Y. Zhu, M.E. Kenney, A.M. Broome, Nanoscale 7 (2015) 1782–1790.

[137] D. Kim, Y.Y. Jeong, S. Jon, ACS Nano 4 (2010) 3689–3696.

[138] S. Dhar, W.L. Daniel, D.A. Giljohann, C.A. Mirkin, S.J. Lippard, J. Am. Chem. Soc. 131 (2009) 14652–14653.

[139] R. Toy, P.M. Peiris, K.B. Ghaghada, E. Karathanasis, Nanomedicine 9 (2014) 121–134.

[140] Expert Opin. Drug Deliv. 12 (2015) 129–142.

[141] S.M. Hussain, K.L. Hess, J.M. Gearhart, K.T. Geiss, J.J. Schlager, Toxicol. Vitr. 19 (2005) 975–983.

[142] G.A. Sotiriou, A. Meyer, J.T.N. Knijnenburg, S. Panke, S.E. Pratsinis, Langmuir 28 (2012) 15929–15936.

[143] G.A. Sotiriou, G.D. Etterlin, A. Spyrogianni, F. Krumeich, J.C. Leroux, S.E. Pratsinis, Chem. Commun. 50 (2014) 13559–13562.

[144] G.A. Sotiriou, T. Sannomiya, A. Teleki, F. Krumeich, J. Vörös, S.E. Pratsinis, Adv. Funct. Mater. 20 (2010) 4250–4257.

[145] G. Sotiriou, C. Blattmann, S. Pratsinis, in:, Mater. Res. Soc. Symp. Proc., Cambridge University Press, 2013.

[146] I.I. Slowing, J.L. Vivero-Escoto, B.G. Trewyn, V.S.Y. Lin, J. Mater. Chem. 20 (2010) 7924–7937.

[147] Y. Hoshikawa, H. Yabe, A. Nomura, T. Yamaki, A. Shimojima, T. Okubo, Chem. Mater. 22 (2010) 12–14.

[148] F.K. Alanazi, A.A. Radwan, I.A. Alsarra, Saudi Pharm. J. 18 (2010) 179–193.

[149] C. Kim, P. Ghosh, V.M. Rotello, Nanoscale 1 (2009) 61–67.

[150] P. Chen, S. Mwakwari, A. Oyelere, Nanotechnol. Sci. Appl. 1 (2008) 45–66.

[151] B. Cheng, H. He, T. Huang, S.S. Berr, J. He, D. Fan, J. Zhang, P. Xu, J. Biomed. Nanotechnol. 12 (2016) 435–449.

[152] S. Link, C. Burda, B. Nikoobakht, M.A. El-Sayed, J. Phys. Chem. B 104 (2000) 6152–6163.

[153] J. Chen, B. Wiley, Z.Y. Li, D. Campbell, F. Saeki, H. Cang, L. Au, J. Lee, X. Li, Y. Xia, Adv. Mater. 17 (2005) 2255–2261.

[154] Y. Shigemasa, S. Minami, Biotechnol. Genet. Eng. Rev. 13 (1996) 383–420.

[155] M.J. Laudenslager, J.D. Schiffman, C.L. Schauer, Biomacromolecules 9 (2008) 2682–2685.

[156] M. Fathi, S. Majidi, P.S. Zangabad, J. Barar, H. Erfan-Niya, Y. Omidi, Med. Res. Rev. 38 (2018) 2110–2136.

[157] R.C.F. Cheung, T.B. Ng, J.H. Wong, W.Y. Chan, Mar. Drugs 13 (2015) 5156–5186.

[158] D. Frackowiak, J. Photochem. Photobiol. B Biol. 2 (1988) 399–408.

[159] P.W. Atkins, Physical Chemistry, 8th ed., Oxford University Press, Oxford, 2006.

[160] M. Ethirajan, Y. Chen, P. Joshi, R.K. Pandey, Chem. Soc. Rev. 40 (2011) 340–362.

[161] A. Gilbert, J. Baggot, Essentials of Molecular Photochemistry, 1st ed., Blackwell Science Ltd., Oxford, 1991.

[162] E.T. Saka, C. Göl, M. Durmus, H. Kantekin, Z. Biyiklioglu, J. Photochem. Photobiol. A Chem. 241 (2012) 67–78.

[163] S. Fery-Forgues, D. Lavabre, J. Chem. Educ. 76 (1999) 1260–1264.

[164] D.M. Maree, T. Nyokong, K. Suhling, D. Phillips, J. Porphyr. Phthalocyanines 6 (2002) 373–376.

[165] H.C. Gerritsen, R. Sanders, A. Draaijer, Proc. SPI 2329 (1994) 260 (8 pages).

[166] A.G. Ryder, S. Power, T.J. Glynn, J.J. Morrison, Proc. SPI 4529 (2001) 102–109.

[167] T.H. Tran–Thi, C. Desforge, C. Thiec, S.J. Gaspard, Phys. Chem. 93 (1989) 1226–1233.

[168] L. Deboni, E. Piovesan, L. Gaffo, C.R. Mendonca., Phys. Chem. A. 112 (2008) 6803–6807.

[169] K.R. Weishaupt, C.J. Gomer, J. Dougherty, Cancer Res. 36 (1976) 2326–2329.

[170] N.A. Kuznetsova, N.S. Gretsova, V.M. Derkacheva, O.L. Kaliya, E.A.

Lukyanets, J. Porphyrins Phthalocyanines. 7 (2003) 147–154.

[171] A.A. Gorman, Chem Soc Rev 10 (1981) 205–231.

[172] N.A. Kuznetsova, N. Gretsova, O. Yuzhakova, V. Negrimovsky, O. Kaliya, E. Luk'yanets, Russ. J. Gen. Chem. 71 (2001) 36–41.

[173] T. Nyokong, E. Antunes, in:, K.M. Kadish, K. Smith, R. Guilard (Eds.), Handb. Porphyr. Sci., 7th ed., Academic Press, New York, 2010, pp. 247–349.

[174] T. Nyokong, Pure Appl. Chem. 83 (2011) 1763–1779.

[175] C.S. Foote, Singlet Oxygen, Academic Press, New York, San Francisco, London, 1979.

[176] J.G. Young, W. Onyebuagu, J. Org. Chem 55 (1990) 2155–2159.

[177] M. Ambroz, A. Beeby, A. McRobert, M. Simpson, R. Svensen, D. Phillips, J Photochem Photobiol B. Biol. 9 (1991) 87–95.

[178] J.R. Lakowicz, Principles of Fluorescence Spectroscopy, 2nd ed., Kluwer Academic/Plenum Publishers, New York, 1999.

[179] P. Grisoli, V. Necchi, P. Pallavicini, L. Pasotti, M. Patrini, Langmuir 28 (2012) 8140–8148.

[180] N. Masilela, T. Nyokong, J. Photochem. Photobiol. A Chem. 223 (2011) 124–131.

[181] K.A. Kozek, K.M. Kozek, W.C. Wu, S.R. Mishra, J.B. Tracy, Chem. Mater 25 (2013) 4537−4544.

[182] L. Chen, F. Ji, Y. Xu, L. He, Y. Mi, F. Bao, B. Sun, X. Zhang, Q. Zhang, Nano Lett. 14 (2014) 7201–7206.

[183] N. Zamand, A. Pour, M. Housaindokht, M. Izadyar, Solid State Sci. 33 (2014) 6–11.

[184] G. Sánchez, D. Curiel, I. Ratera, A. Tárraga, J. Veciana, P. Molina, Dalt. Trans. 42 (2013) 6318–6326.

[185] A. Gole, C.J. Murphy, Chem. Mater 16 (2004) 3633–3640.

[186] G. Zhang, X. Sun, J. Jasinski, D. Patel, A.M. Gobi, J. Nanomater 2012 (2012) 9 pages.

[187] H. Salehizadeh, E. Hekmatian, M. Sadeghi, K. Kennedy, J. Nanobiotechnology 10 (2012) 1–7.

[188] J. Mack, M.J. Stillman, in:, K.M. Kadish, K.M. Smith, R. Guilard (Eds.), Porphyr. Handb., 16th ed., Academic Press, New York, 2003, pp. 43–116.

[189] T. Furuyama, K. Satoh, T. Kushiya, N. Kobayashi, J. Am. Chem. Soc. 136 (2014) 765–776.

[190] M.J. Stillman, T. Nyokong, in:, C.C. Leznoff, A.B.. Lever (Eds.), Phthalocyanines Prop. Appl., 1st ed., VCH Publishers, New York, NY, 1989, pp. 133–289.

[191] E. Gürel, M. Pişkin, S. Altun, Z. Odabaş, M. Durmuş, Dalt. Trans. 44 (2015) 6202–6211.

[192] K. Sakamoto, E. Ohno-Okumura, T. Kato, H. Soga, J. Porphyr. Phthalocyanines 14 (2010) 47–54.

[193] S. Liu, G. Chen, P.N. Prasad, M.T. Swihart, Chem. Mater. 23 (2011) 4098–4101.

[194] H. Hiramatsu, F.E. Osterloh, Chem. Mater. 16 (2004) 2509–2511.

[195] Z. Li, Y. Yu, Z. Chen, T. Liu, Z.K. Zhou, J.B. Han, J. Li, C. Jin, X. Wang, J. Phys. Chem. C 117 (2013) 20127–20132.

[196] J.E. Millstone, S. Park, K.L. Shuford, L. Qin, G.C. Schatz, C.A. Mirkin,

J. Am. Chem. Soc. 127 (2005) 5312–5313.

[197] S. Ke, C. Kan, J. Liu, B. Cong, RSC Adv. 3 (2013) 2690–2696.

[198] M.H. Majles Ara, Z. Dehghani, R. Sahraei, A. Daneshfar, Z. Javadi, F. Divsar, J. Quant. Spectrosc. Radiat. Transf. 113 (2012) 366–372.

[199] M.A. Khan, S. Kumar, M. Ahamed, S.A. Alrokayan, M.S. Alsalhi, M. Alhoshan, A.S. Aldwayyan, Appl. Surf. Sci. 257 (2011) 10607–10612.

[200] R. Jenkins, R.L. Synder, Introduction to X-Ray Diffractometry, 138th ed., Wiley and Sons, New York, 1996.

[201] I. Papagiannouli, P. Aloukos, D. Rioux, M. Meunier, S. Couris, J. Phys. Chem. C 119 (2015) 6861–6872.

[202] B.C. Smith, Infrared Spectra Interpretation: A System Approach, 1st ed., CRC Press, New York, 1998.

[203] K.G. Thomas, P. V. Kamat, Acc. Chem. Res. 36 (2003) 888–898.

[204] R. Prabakaran, R. Kesavamoorthy, G.L.N. Reddy, F.P. Xavier, Phys. Status Solidi. 229 (2002) 1175–1186.

[205] D. Kumar, B.J. Meenan, I. Mutreja, R. D'sa, D. Dixon, Int. J. Nanosci. 11 (2012) 1250023 (7 pages).

[206] N. Soni, S. Prakash, Am. J. Nanotechnol. 2 (2011) 112–121.

[207] F.Y. Alzoubi, J.Y. Alzouby, M.K. Alqadi, H.A. Alshboul, K.M. Aljarrah, Chinese J. Phys. 53 (2015) 9 pages.

[208] J.K. Patra, K.H. Baek, J. Nanomater. 2014 (2014) 417305 (12 pages).

[209] D.M.T. Dang, T.T.T. Le, E. Fribourg-Blanc, M.C. Dang, Adv. Nat. Sci. Nanosci. Nanotechnol. 3 (2012) 035004 (4 pages).

[210] L. Li, J.F. Zhao, N. Won, H. Jin, S. Kim, J.Y. Chen, Nanoscale Res. Lett. 7 (2012) 386–393.

[211] Y. Bae, N.H. Kim, M. Kim, K.Y. Lee, S.W. Han, J. Am. Chem. Soc. 130 (2008) 5432–5433.

[212] A. Nagal, R. Singla, Indo Glob. J. Pharm. Sci. 3 (2013) 96–106.

[213] E. Hotze, T. Phenrat, G. Lowry, J Env. Qual 39 (2010) 1909–1924.

[214] A.K. Singh, Physicochemical, Electronic, and Mechanical Properties of Nanoparticles, 3rd ed., Academic Press, Oxford, 2016.

[215] M. Bouchoucha, C. René, M. Fortin, F. Kleitz, Adv. Funct. Mater. 24 (2014) 5911–5923.

[216] J.W. Owens, M.J. Robins, J. Porphyr. Phthalocyanines 5 (2001) 460–464.

[217] Z. Petrásek, D. Phillips, Photochem. Photobiol. Sci. 2 (2003) 236–244.

[218] C. Geddes, Topics in Fluorescence Spectroscopy, 10th ed., Springer, New York, 2005.

[219] C. Xue, Y. Xue, L. Dai, A. Urbas, Q. Li, Adv. Opt. Mater. 1 (2013) 581–587.

[220] J.A. Lacey, D. Philips, Photochem. Photobiol. Sci. 1 (2002) 378–383.

[221] G.D.C. Naulin, M. Costes, A. Benseddick, Laser Chem 8 (1988) 238–302.

[222] D. Phillips, Proc. R. Soc. A Math. Phys. Eng. Sci. 472 (2016) 20160102 (21 pages).

[223] G.J. Smith, Photochem. Photobiol. 41 (1985) 123–126.

[224] Z.N. Erol, P. Atienzar, Y. Arslanoılu, E. Hamuryudan, H. García, RSC Adv. 5 (2015) 55901–55908.

[225] M.G. Debacker, O. Deleplanque, B. van Vleirberge, F.X. Sauvage, B. Van Vlierberge, F.X. Sauvage, Laser Chem. 8 (1988) 1–11.

[226] J.R. Darwent, P. Douglas, A. Harriman, G. Porter, M.C. Richoux, Coord.

Chem. Rev. 44 (1982) 83–126.

[227] X. Zhang, Y. Dia, F. Zhang, J. Photochem. Photobiol. A Chem. 203 (2009) 216–221.

[228] X. Zhang, X. Li, L. Niu, L. Sun, L. Liu, J. Fluoresc. 19 (2009) 947–954.

[229] S.V. Rao, P.T. Anusha, L. Giribabu, S.P. Tewari, Pramana 75 (2010) 1017–1023.

[230] A. Fashina, E. Antunes, T. Nyokong, R. Zugle, J. Mol. Struct 1068 (2014) 245–254.

[231] A.B. Ormond, H.S. Freeman, Materials (Basel). 6 (2013) 817–840.

[232] E.I. Sagun, E.I. Zenkevich, V.N. Knyukshuto, A.M. Shulga, D.A. Starukhin, C. von Borczyskowski, Chem. Phys 275 (2002) 211–230.

[233] S.J. Chadwick, D. Salah, P.M. Livesey, M. Brust, M. Volk, J. Phys. Chem. A 120 (2016) 10647−10657.

[234] R. Yin, T. Agrawal, U. Khan, G.K. Gupta, R. V, Y.Y. Huang, M.R. Hamblin, Nanomedicine 10 (2015) 2379–2404.

[235] Y.Y. Huang, S.K. Sharma, T. Dai, H. Chung, A. Yaroslavsky, M. Garcia-Diaz, J. Chang, L. Chiang, M. Hamblin, Nanotech Rev 10 (2012) 111–146.

[236] H. Ramesh, T. Mayr, M. Hobisch, S. Borisov, I. Klimant, U. Kruhne, J. Woodley, J. Chem. Technol. Biotechnol. 91 (2016) 832–836.

[237] D. Atilla, N. Saydan, M. Durmuş, A.G. Gürek, T. Khan, A. Rück, H. Walt, T. Nyokong, V. Ahsen, J. Photochem. Photobiol. A Chem. 186 (2007) 298–307.

[238] A.M. Alkilany, P.K. Nagaria, C.R. Hexel, T.J. Shaw, C.J. Murphy, M.D. Wyatt, Small 5 (2009) 701–708.

[239] A.M. Alkilany, L.B. Thompson, S.P. Boulos, P.N. Sisco, C.J. Murphy, Adv. Drug Deliv. Rev. 64 (2012) 190–199.

[240] Y. Zhang, D. Xu, W. Li, J. Yu, Y. Chen, J. Nanomater. 2012 (2012) 7 pages.

[241] H. Parab, H. Chen, T. Lai, J. Huang, P. Chen, R. Liu, M. Hsiao, C. Chen, D. Tsai, Y. Hwu, J. Phys. Chem. C 113 (2009) 7574–7578.

[242] S. Manohar, R. Rayavarapu, W. Petersen, T.G. van Leeuwen, SPIE Proc 7177 (2009) 8 pages.

[243] A.P. Leonov, J. Zheng, J.D. Clogston, S.T. Stern, A.K. Patri, A. Wei, ACS Nano 2 (2008) 2481– 2488.

[244] M.F. Tsai, S.H. Chang, F.Y. Cheng, V. Shanmugam, Y.S. Cheng, C.H. Su, C.S. Yeh, ACS Nano 7 (2013) 5330–5342.

[245] L. Xing, B. Chen, D. Li, W. Wu, Z. Ying, Lasers Surg Med 50 (2018) 669–679.